



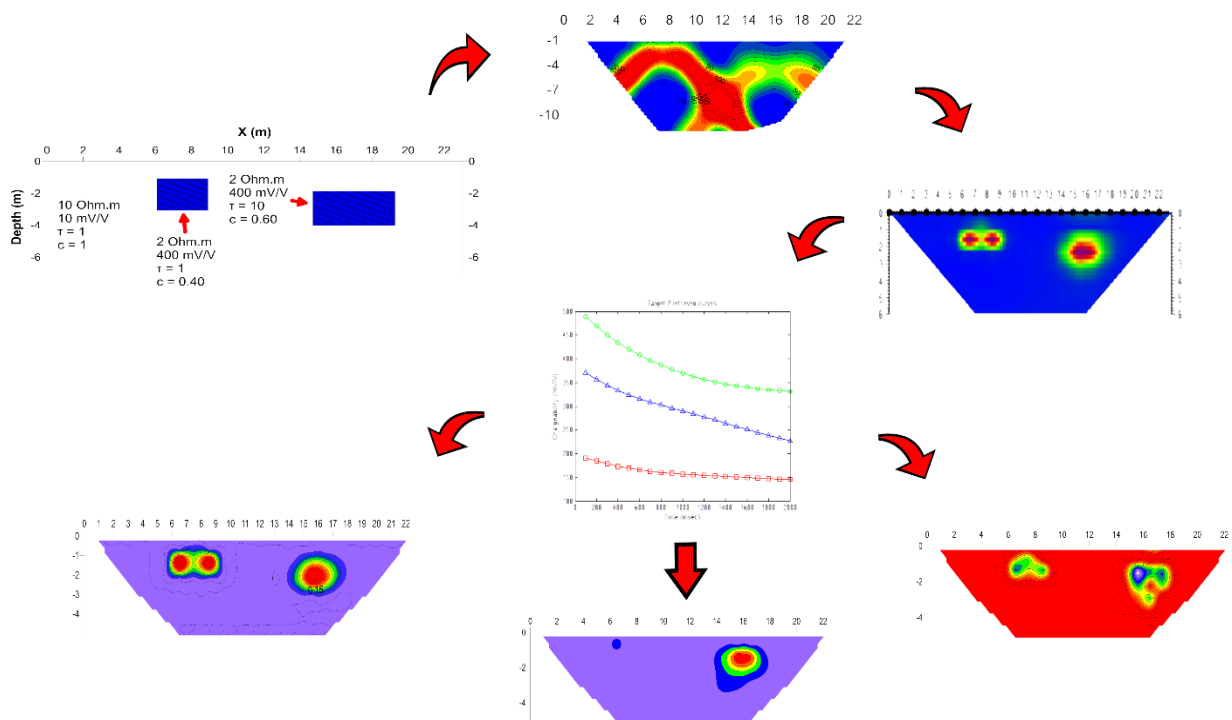
Aristotle University of Thessaloniki

School of Geology

Department of Geophysics



Processing and Modeling of Induced Polarization Data



Nivorlis Aristeides

Master Thesis

Postgraduate Program of the School of Geology in

"Applied and Environmental Geology"

Specialization: Applied Geophysics

January 2017





NIVORLIS ARISTEIDES

GEOLOGIST

Processing and Modeling of Induced Polarization Data

Submitted to the School of Geology of Aristotle University of Thessaloniki within the
postgraduate program “Applied and Environmental Geology” in specialization
“Applied Geophysics”

Date of Oral Examination: 22nd of February 2017

Advisory Committee

Professor Panagiotis Tsourlos (Supervisor)

Associate Professor George Vargemezis (Advisory Committee member)

Professor Gregory Tsokas (Advisory Committee member)

© Nivorlis Aristeides, 2017

All right reserved.

Processing and Modeling of Induced Polarization Data





*To my family,
for their constant support
over the years of my studies.*





Acknowledgements

First of all I would like to express my gratitude to my supervisor Professor Panagiotis Tsourlos for his constant support and guidance through the years of my studies. His advices helped me to deepen my knowledge and better understand topics not only relevant to this work but to general geophysical problem solving. He was a true mentor for me during my Bachelor and Master studies.

I want to thank Associate Professor George Vargemezis for his overall guidance and consulting over the past years and for the opportunities he gave me to participate in a variety of geophysical projects that helped me gather valuable experience.

I want to thank Professor Gregory Tsokas for giving me the chance to participate in many archaeological surveys that helped me further develop my geophysical fieldwork skills.

I want to thank the staff of the Department of Geophysics in the Aristotle University of Thessaloniki and especially Dr. Ilias Fikos for their help and the advices that they gave me. Furthermore, I want to thank my fellow master students Dimitris Angelis, Dimitris Oikonomou, Kostas Polidoropoulos and Nikos Chatzis, for their good partnership over the years of our master studies and their help in the collection of some of the data used in this work. I would also like to acknowledge MSc student Lais Trento for her help during the collection of the experimental data.

Last but not least, I would like to thank my family and especially my parents. Their support over the last years made it possible for me to successfully complete my work. The least I can do is to dedicate this work to them.



Abstract

This thesis studies the Induced Polarization method and focuses on developing schemes for Time Domain Induced Polarization modeling, inversion and data interpretation.

For DC-TDIP 3D modeling an existing 3D FEM based DC forward solver was modified in order to incorporate the 3D modeling of the TDIP data, producing 3D TD spectral IP data for complex geometry bodies given their resistivity, chargeability and the so-called Cole-Cole parameters for every (user defined) time window.

The Spectral IP Inversion of the data was performed using a special version of the DC2D PRO software which applies a smoothness-constrained inversion by introducing inverse model regularizations not only for the space domain but also for the channel domain by inverting up to a maximum of 20 IP windows simultaneously.

The spectral inversion model is then used for the calculation of the Cole-Cole parameters by fitting a Cole-Cole model using a Matlab code which developed within this project, based on the Particle Swarm Optimization algorithm.

The above modeling-inversion sequence was tested extensively with synthetic data and the 3D effects associated to the 2D RES-TDIP inversion were evaluated using various synthetic models.

As the proposed approach is designed to accommodate real data it is acknowledged that prior to its application it is important that the quality of the DC-TDIP data is evaluated. For this purpose, an additional tool was developed (matlab code with GUI) to perform pre-processing of the DC TDIP data.

The results of the synthetic, experimental and real data applications suggests that the presented approach is efficient and relatively robust given the complexity of the SIP data processing. Future work involves extending the present tools in a fully 3D and 4D (time lapse) mode.



Περίληψη

Στα πλαίσια της παρούσας διατριβής μελετάται η μέθοδος της Επαγόμενης Πόλωσης, επικεντρώνοντας στην ανάπτυξη τεχνικών για την μοντελοποίηση, αντιστροφή και ερμηνεία δεδομένων Χρονο-Μεταβαλλόμενης Επαγόμενης Πόλωσης (TDIP).

Για την μοντελοποίηση των TDIP δεδομένων ένα προϋπάρχον πρόγραμμα, που βασίζεται στην μέθοδο των πεπερασμένων στοιχείων τροποποιήθηκε για να ενσωματώσει την λειτουργία της μοντελοποίησης των TDIP δεδομένων, παράγοντας πραγματικά δεδομένα τριών διαστάσεων, με βάση το μοντέλο Cole-Cole, για κάθε χρονικό παράθυρο που ορίζει ο χρήστης.

Η αντιστροφή των δεδομένων έγινε με την χρήση μίας ειδικής έκδοσης του λογισμικού DC2DPRO, όπου χρησιμοποιεί την μέθοδο της εξομαλυμένης αντιστροφής εισάγοντας ομαλότητα όχι μόνο στο πεδίο του χώρου αλλά και στο πεδίο των παραθύρων, δίνοντας την δυνατότητα για ταυτόχρονη αντιστροφή έως και 20 παραθύρων.

Το μοντέλο που προκύπτει από την αντιστροφή χρησιμοποιείται για την εξαγωγή των εσωτερικών τιμών (για κάθε κελί) των παραμέτρων του μοντέλου Cole-Cole, χρησιμοποιώντας τον αλγόριθμο Particle Swarm Optimization που αναπτύχθηκε στην matlab στα πλαίσια αυτής της διατριβής.

Τα παραπάνω βήματα δοκιμάστηκαν εκτενέστερα σε συνθετικά δεδομένα και μελετήθηκε το φαινόμενο της τρισδιάστατης επιρροής στις 2D αντιστροφές TDIP δεδομένων.

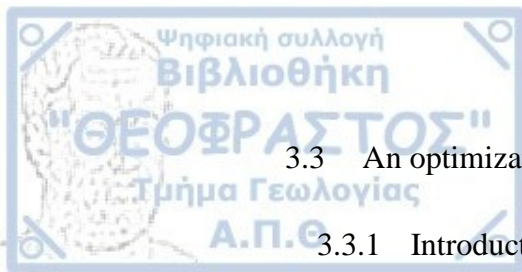
Με δεδομένο ότι η προτεινόμενη σειρά επεξεργασίας θα χρησιμοποιηθεί και σε πραγματικά δεδομένα, αναπτύχθηκε ένα λογισμικό σε γλώσσα matlab (με GUI) για την εκτίμηση της ποιότητας των δεδομένων πριν το στάδιο της αντιστροφής.

Τα αποτελέσματα από τα συνθετικά, τα πειραματικά και τα πραγματικά δεδομένα δείχνουν ότι η παρούσα αντιμετώπιση είναι αρκετά αποδοτική δεδομένης της πολυπλοκότητας των TDIP δεδομένων. Η μελλοντική δουλειά περιλαμβάνει την επέκταση των εργαλείων σε 3 και 4 (time lapse) διαστάσεις.

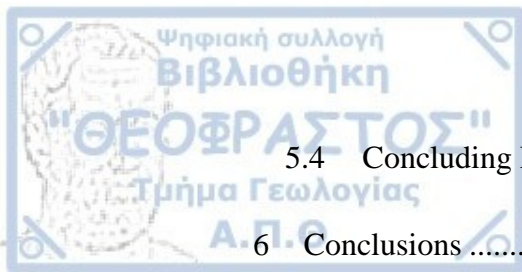


CONTENTS

1	Introduction	1
1.1	Thesis subject and aims	1
1.2	The structure of the thesis	3
2	Basic Theory	5
2.1	Resistivity Method	6
2.1.1	Apparent resistivity	8
2.1.2	Resistivity arrays	9
2.1.3	Electrical Resistivity Tomography	11
2.2	Induced Polarization	12
2.3	Forward Modeling	18
2.3.1	Finite Element Method	19
2.4	Inversion	21
3	Modeling and Inversion tools of Time Domain IP (TDIP) Data	27
3.1	Modeling of Time-Domain Induced Polarization (TDIP) Data	28
3.1.1	Algorithm Description	28
3.1.2	Induced Polarization (IP) Modeling	29
3.1.3	Time Domain Induced Polarization (TDIP) Modeling	29
3.1.4	TDIP Program	32
3.2	Inversion of TDIP data using DC2DPRO	38
3.2.1	Program Operation	40



3.3	An optimization tool for Calculating of the Cole – Cole Parameters	44
3.3.1	Introduction	44
3.3.2	Particle Swarm Optimization	45
3.3.3	Algorithmic Development.....	48
4	Application to Synthetic Time Domain IP Data.....	57
4.1	Introduction	58
4.2	Model 1	58
4.3	Model 2	65
4.4	3D effects on 2D inversion.....	72
4.5	Concluding Remarks	78
5	Application to Real Time Domain IP data	81
5.1	Pre Processing	82
5.2	Experimental Data.....	87
5.2.1	Introduction	87
5.2.2	Background Measurement.....	88
5.2.3	Experiment 1 – Metal Pipe Down lift	89
5.2.4	Experiment 2 – 3D effect	94
5.3	Real Data	98
5.3.1	Introduction	98
5.3.2	Inversion Results	99
5.3.3	Cole-Cole Model	101



5.4	Concluding Remarks	103
6	Conclusions	107
6.1	Future Work	110
7	References	113
8	Appendix I	i
Figure 2. 1.	Electrical resistivity of a cylinder	6
Figure 2. 2.	Basic resistivity array.	7
Figure 2. 3.	Commonly used electrode arrays (Tsourlos, 1995).....	10
Figure 2. 4.	Electrical Resistivity Tomography survey.	11
Figure 2. 5.	Square wave used for current injection in resistivity method (left) and IP method (right).	13
Figure 2. 6.	Voltage over time during IP current on and off times.....	14
Figure 2. 7.	Typical IP voltage curve (from Syscal Pro manual).	15
Figure 2. 8.	Decay curve for different intrinsic chargeability values.	16
Figure 2. 9.	Decay curve for different relaxation time (τ) values.....	17
Figure 2. 10.	Decay curve for different frequency dependence (c) values.	17
Figure 2. 11.	Finite Element Mesh (left), hexahedral element and nodes (right).....	20
Figure 2. 12.	Simplified overview of the Finite Element Method.	21
Figure 2. 13.	Smoothness matrix for a 9 parameter model (Tsourlos, 1995)	23
Figure 2. 14.	Smoothness constrain for two parameter (p1, p2) space (after Box and Kanemasu, 1972).	24
Figure 2. 15.	Simplified flowchart of the inversion process.....	26
Figure 3. 1.	Modified version of the algorithm used for the forward modeling.	31

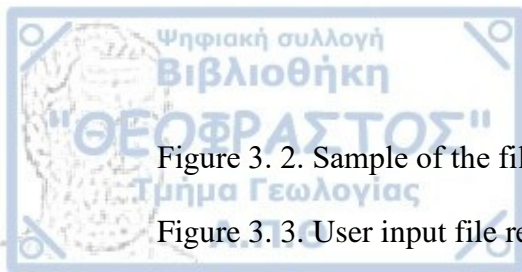


Figure 3. 2. Sample of the file that contains the array's geometry information.	32
Figure 3. 3. User input file required for the 3D TDIP solver.....	34
Figure 3. 4. Spectral IP forward solution for 20 window model.	35
Figure 3. 5. X-Z plain of the middle slice for the example model (prism 1 on the left and prism 2 on the right).....	36
Figure 3. 6. 3D View of the example model's geometry (prism 1 on the left and prism 2 on the right).....	36
Figure 3. 7. Pseudo section of (a) resistivity, (b) - (d) chargeability for channel 1, 4 and 10.....	37
Figure 3. 8. Apparent Chargeability of model measurements.	38
Figure 3. 9. DC2D Pro, model edit.	40
Figure 3. 10. DC2D Pro, data edit (left) and error analysis (right).....	41
Figure 3. 11. Spectral IP Inversion parameters used.	42
Figure 3. 12. Inverted chargeability values for Channel 1 (top) Channel 5 (middle) and Channel 10 (bottom).	43
Figure 3. 13. Extraction of intrinsic chargeability curves. Resistivity image (top and) chargeability values of model cell #70 and #78 (bottom).....	44
Figure 3. 14. Velocity vectors used in Particle Swarm.....	48
Figure 3. 15. Setup options of Particle Swarm Optimization algorithm developed in matlab.....	49
Figure 3. 16. Particle Swarm Optimization input file.....	50
Figure 3. 17. Sample of the algorithm execution.....	50
Figure 3. 18. Flowchart of the main function used for the calculation of the Cole-Cole parameters.....	51

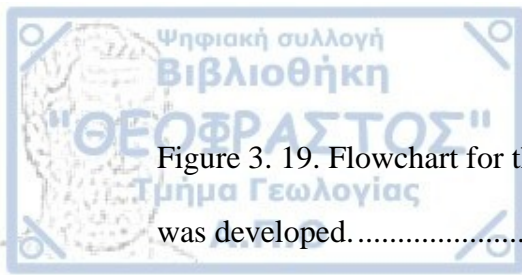


Figure 3. 19. Flowchart for the detailed Particle Swarm Optimization algorithm that was developed.....	52
Figure 3. 20. Particle Swarm Optimization results for Test Sample 1.	53
Figure 3. 21. Particle Swarm Optimization results for Test Sample 2.	54
Figure 3. 22. Model block 70 (left) and 78 (right).....	55
Figure 4. 1. X-Z plain of the middle slice for Model 1.....	59
Figure 4. 2. 3D view of Original Model Geometry for Model 1.	60
Figure 4. 3. Model 1 pseudo section of (a) apparent resistivity, (b) - (f) apparent chargeability of channel 1, 4, 7, 12, 15.....	61
Figure 4. 4. TDIP inversion results for Model 1. (a) resistivity, (b) - (f) chargeability for channel 1, 4, 7, 12, 15.	62
Figure 4. 5. Decay curves for intrinsic chargeability values for the first body (left) and the second body (right) of Model 1. The location of each model block can be seen in the top figure.....	63
Figure 4. 6. TDIP final inversion results for Model 1.	65
Figure 4. 7. X-Z plain of the middle slice for Model 2.....	66
Figure 4. 8. 3D view of the original geometry of Model 2.....	66
Figure 4. 9. Model 2 Pseudo section of (a) apparent resistivity, (b) - (f) apparent chargeability of channel 1, 4, 7, 12, 15.....	67
Figure 4. 10. TDIP inversion results for Model 2 (a) resistivity, (b) - (f) channel 1, 4, 7, 12, 15.....	68
Figure 4. 11. Decay curves for intrinsic chargeability for the upper left prism (left) and the upper right prism (right) for Model 2. The location of the model blocks can be seen in top figure.....	69
Figure 4. 12. TDIP final inversion results for Model 2.	71

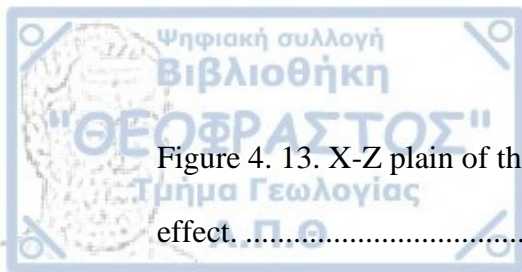


Figure 4. 13. X-Z plain of the middle slice for all the Models used in the study of 3D effect.	73
Figure 4. 14. X-Y slices at 2.5m depth for Model 12a (a) to Model 1a (d) which used in study of the 3D effect.....	73
Figure 4. 15. Pseudo section of the 1st and 3th IP channels for model 12a (a) to model 1a (d).	74
Figure 4. 16. Inverted Resistivity images for Model 12a (a) to Model 1a (d).	75
Figure 4. 17. Inversion results for the 1st IP channel for model 12a (a) to model 1a (d).	76
Figure 4. 18. Intrinsic chargeability curves all 4 models.	77
Figure 5. 1. Pre Processing tool Main window.	83
Figure 5. 2. Advanced Options.	83
Figure 5. 3. Measurement Signal to Noise plot	84
Figure 5. 4. Bad electrode filtering	85
Figure 5. 5. Decay Curve Shape Filtering.....	86
Figure 5. 6. Experimental Tank set up.	87
Figure 5. 7. Tank background experiment inversion results (nothing but water).....	89
Figure 5. 8. X-Z slice of the geometry of each experiment.	90
Figure 5. 9. Inverted resistivity image for the experiments.	91
Figure 5. 10. Inverted Chargeability of 3rd Channel (400-480 ms).	92
Figure 5. 11. Inverted Chargeability of 13th channel (1360-1440).	92
Figure 5. 12. Intrinsic chargeability curves of the central block. The Particle Swarm Optimization fit can be seen with the dashed line.	93
Figure 5. 13. Geometry of 2nd experiment. X-Z slice (top) and top view (bottom). ..	95

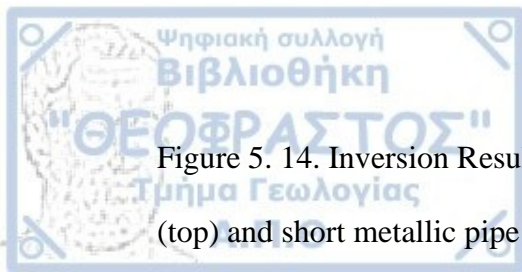


Figure 5. 14. Inversion Results for experiment 2 (3D effect) for the long metallic pipe (top) and short metallic pipe (bottom).96

Figure 5. 15. Intrinsic chargeability curves. The Particle Swarm Optimization fit can be seen with dashed line.97

Figure 5. 16. Location of the survey. Observatory building can be seen on the right edge of the map.99

Figure 5. 17. Inversion results for north line (top), middle line (middle) and south line (bottom)..... 100

Figure 5. 18. 3D inverted model of survey. 101

Figure 5. 19. Cole-Cole calculation results for north line (top), middle line (middle) and south line (bottom) 102



CHAPTER 1

Introduction

1.1 Thesis subject and aims

The Induced Polarization (IP) is a geoelectrical geophysical method which is widely used in a variety of studies and recently has gained a lot of research attention. The IP property can be measured in time domain as part of the standard geoelectrical resistivity measurement and it records an additional parameter, the so-called chargeability, which is a metric of the amount of electrical energy that was stored into the subsurface during the current injection. In this case the earth is acting as a capacitor and stores electrical energy.

In Time Domain Induced Polarization (TDIP) method, the amount of energy released is calculated over time so in this case it is possible not only to calculate the overall apparent chargeability but also to obtain the energy discharge pattern of each single measurement. It is acknowledged that through the study of this pattern useful information about the nature of the chargeable subsurface materials can be obtained.

Certain models have been proposed to describe the TDIP energy discharge but the most widely used one is the Cole-Cole model. The calculation of the Cole-Cole model's parameters can be linked to different materials and could provide extra information about the subsurface structure.

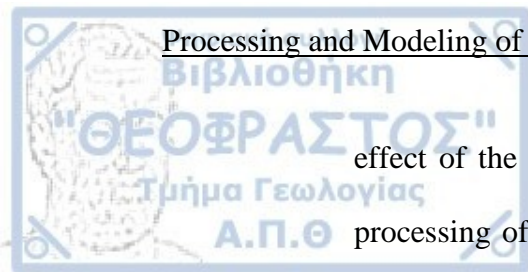
The TDIP method is widely used over the last years for mineral exploration, hydrogeological, environmental and geotechnical investigations because the chargeability signature of several minerals and pollutants is very strong compared to their surroundings. Given the applicability of the technique there is a growing research

interest in to going beyond the study of chargeability towards the studying of the TDIP patterns and the extraction of useful parameters which can be directly used for material characterization.

As this is a current research field this thesis is targeting into making a contribution regarding the modeling and processing of TDIP data. The goal is to provide a scheme for processing and interpreting Time Domain Induced Polarization under the assumption of the Cole-Cole model in order to better understand and identify complex patterns in the interpretation of the TDIP results. Additionally, this work is aimed to be used as the basis for future development of schemes and for further processing of TDIP data using 3D and 4D (time lapse) inversion tools.

The tools and methodology which are needed for such a study include:

- An algorithm to calculate the TDIP response (forward solution) of a given target geometry (ideally 3D) using the Cole-Cole model. The produced synthetic data will be used to understand the TDIP behavior and also to generate perfect data to test processing algorithms.
- IP Inversion software which is able to cope with the complex nature of the data i.e. with the IP data of all recorded time channels in order to reconstruct the decay curve of the intrinsic chargeability properties (e.g. the pattern of the released energy) for every single model cell.
- Tools to retrieve the intrinsic electrical properties (i.e. the Cole-Cole parameters) for every model cell from the inverted decay curves.
- Tests of the processing procedure with synthetic data to better understand the effect of various parameters to the final results. Out of great importance is the simulation of the effect of the burial depth, the



effect of the 3D nature of the targets into the 2D inversion, and the processing of the different values of the Cole-Cole parameters of the materials.

- Further verification of the findings is required using controlled TDIP experiments in a test tank and tests in real field conditions. As the real data may suffer from noise pre-filtering may be required.

1.2 The structure of the thesis

The structure of this thesis reflects the above described methodological approach:

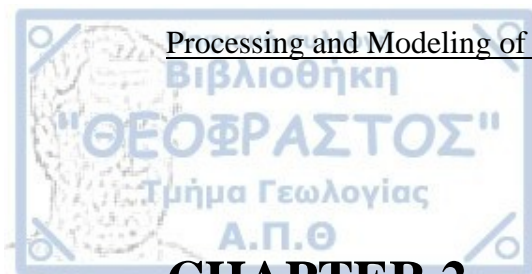
Chapter 2 introduces the basics of the electrical resistivity method. It also provides a brief introduction to the electrical resistivity tomography and Time Domain Induced Polarization method. Furthermore, it introduces the fundamental concepts needed to understand the solution of the forward problem explaining the Finite Element Method which is used in this work and the inversion process.

Chapter 3 gives a brief explanation of the algorithmic tools that were developed and used in this work. First, the forward solution algorithm is explained and then the inversion software used in this work is presented as well. Finally, the Particle Swarm Optimization algorithm developed for retrieving the Cole-Cole parameters of the TDIP responses is discussed thoroughly.

Chapter 4 illustrates the results of the application of the proposed scheme using synthetic models. The first two models consist of prisms with different electrical properties and complex geometries while in the third model involves a series of prisms with changing size across the strike (y) direction to study the 3D effect of the targets into the 2D TDIP inversion.

Chapter 5 presents the application of the proposed scheme to experimental data collected in a tank and also to real data. Further, it includes the description of a pre-processing tool that was developed to filter real TDIP data.

Chapter 6 summarizes the conclusions that were drawn from this thesis along with the proposed future work.



CHAPTER 2

Basic Theory

In this chapter the basic theory of the electrical resistivity and IP methods is discussed. This chapter is not meant to be a detailed overview of the techniques used but intends to provide the basic information required to better understand the work presented in the following chapters of this thesis. The basic principles regarding the Electrical Resistivity Tomography and the Induced Polarization Method will be provided. Lastly the description of the Cole-Cole model, its parameters and the effect they have on the shape of the intrinsic chargeability decay curve is discussed.

Moreover, in this chapter the fundamental concepts about solving the forward electrical resistivity problem are described. A brief discussion about the Finite Element Method, which was chosen to be used in this work, follows next.

Finally, the inversion process that is used to calculate the true electrical distribution on the subsurface knowing the measured apparent resistivity values is explained.

2.1 Resistivity Method

The electrical resistivity method is widely used in near-surface surveys for a variety of reasons such as the subsurface characterization for geological or engineering applications, mapping of mineral deposits, locating fault zones, hydrogeological investigations and geothermal field applications while over the past years the method was further developed and successfully applied in landslide and remediation monitoring. The resistivity method studies the electrical properties of the subsurface and namely the electrical resistivity.

The resistivity of a cylinder with length L , cross section area S and Ohmic resistance R is given by the formula:

$$\rho = R \frac{S}{l} \quad (2.1)$$

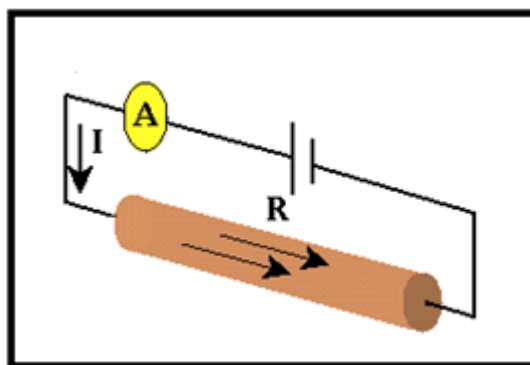


Figure 2. 1. Electrical resistivity of a cylinder.

The electrical resistivity (Ohm m) simulates the difficulty which the electrical current encounters while flowing inside the material, the earth in our case. The reciprocal of electrical resistivity is the electrical conductivity σ (Siemens/m) and is used very often in pair with the resistivity to describe a medium.

$$\sigma = \frac{1}{\rho} \quad (2.2)$$

For a single resistivity measurement four electrodes are needed, two electrodes (A and B) are used to introduce DC electrical current into the ground and two other electrodes (M and N) are used to measure the potential difference due to the application of the electrical field (Figure 2. 2), thus the method is characterized as an **active** method due to the fact that a source is needed.

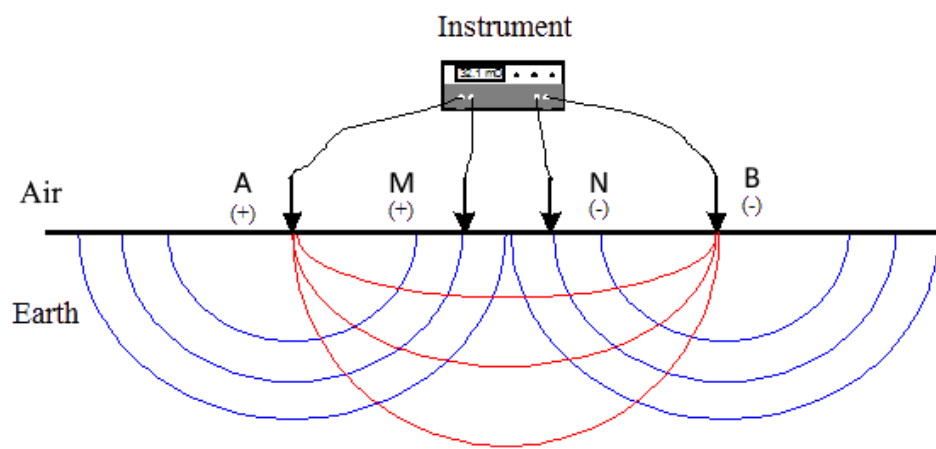


Figure 2. 2. Basic resistivity array.

The potential difference measured in the potential dipole, is used to calculate the resistivity of the ground. First the Ohmic resistance (Ohm) is calculated using the formula:

$$R = \frac{V}{I} \quad (2.3)$$

Where V is the potential difference and I is the current injected into the ground.

From eq. 2.1 and eq. 2.3 the electrical resistivity of a single measurement is:

$$\rho = \frac{\Delta V}{I} \frac{2\pi}{G} = R \frac{2\pi}{G} \quad (2.4)$$

Where R is the Ohmic resistance and G is the geometrical factor of the measurement which is given by the formula:

$$G = \frac{1}{AM} - \frac{1}{BM} - \frac{1}{AN} + \frac{1}{BN} \quad (2.5)$$

The current dipole is connected in series with an ammeter and the potential dipole in parallel with a voltmeter, hence R is calculated for each measurement. Furthermore, knowing the position of the electrodes, the geometrical factor can also be calculated. Applying the geometrical factor to the Ohmic resistance (R) yields the true electrical resistivity in case of homogeneous medium.

2.1.1 Apparent resistivity

However, the earth in most cases is heterogeneous, so the previous calculations do not yield the true electrical resistivity of the ground. In this case the resistivity calculated by the equation 2.4 is called apparent resistivity and represents a kind of weighted average of the resistivities of the different subsurface materials. This is by no means mathematically true (Telford et al, 1990) however in a broad sense this concept can be useful in the interpretation of many simple problems.

Therefore, after an electrical resistivity survey, because of the heterogeneous earth, the measurements of each potential difference are transformed into apparent resistivity, as discussed above. However, the interpretation cannot be made by the apparent resistivity measurements because they give an unrealistic image of the true electrical resistivity distribution.

Because of this, the apparent resistivity distribution measured needs to be used to retrieve the true subsurface resistivity distribution, which can then be interpreted and give valuable information about the subsurface. This is achieved by a mathematically complex process called inversion.

It should be noted that in order to calculate the earth's true resistivity distribution from the measured apparent resistivity (inverse problem) the calculation of the apparent resistivity while knowing the true electrical resistivity of the earth (called the forward problem) is also required.

2.1.2 Resistivity arrays

There are infinite ways to arrange a set of four electrodes in order to obtain a measurement, but among them some are more popular than the others (Figure 2. 3), because they have theoretical and practical benefits. The majority of these arrays offer an internal symmetry that governs the electrode separation distances, which helps both in positioning and data interpretation.

Most of them have the electrodes placed in line because they fulfill the practical criteria which make them easier to apply in an investigation. Each array is characterized by its geometrical factor, as a function of the array's internal geometry. Last but not least, the in-line arrays are commonly divided into two categories the nested and dipole ones.

The nested arrays such as Schlumberger and Wenner have the potential electrodes placed between the current electrodes dipoles while on the other hand the dipole arrays such as dipole-dipole, pole-dipole and pole-pole have the current and potential dipoles apart.

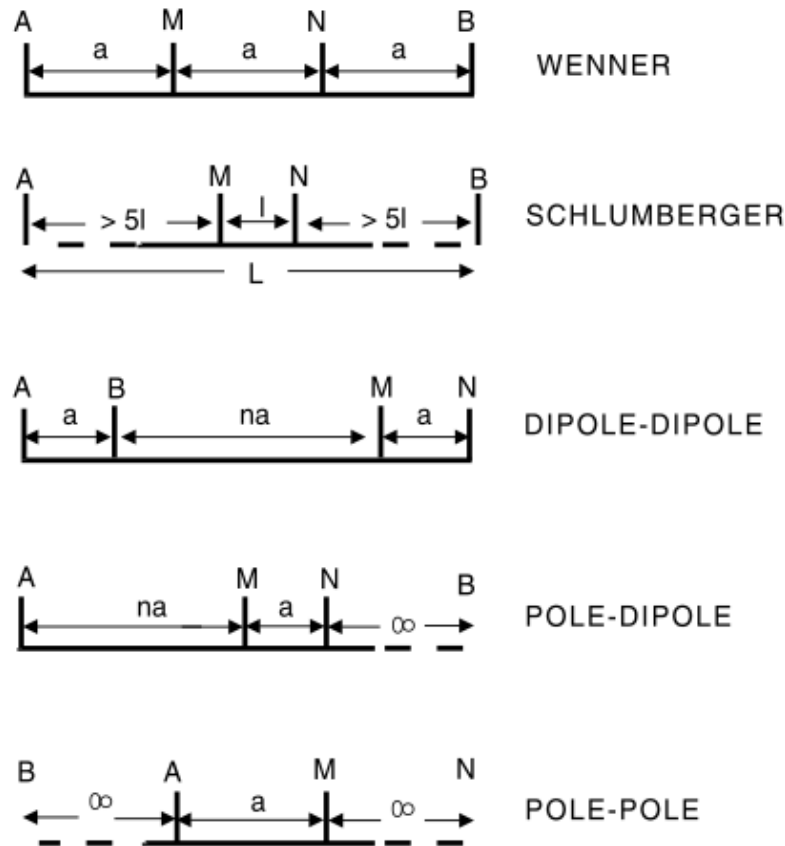
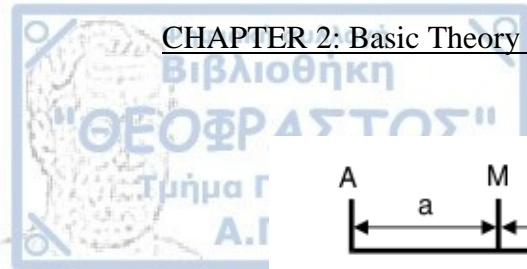


Figure 2. 3. Commonly used electrode arrays (Tsourlos, 1995).

Nested arrays like Wenner have better signal to noise ratio, offering better spatial resolution however they may suffer from limited resolving ability as they are not as sensitive as the dipole ones to lateral changes. In general, the electrode array is chosen depending on the individual investigation target, and frequently measurements from more than one arrays can be combined to further enhance the obtained information.

Evaluation of most commonly used resistivity arrays (after Ward, 1990)			
Array	s/n ratio	lateral resolution	depth resolution
Wenner	1	4	1
Schlumberger	2	3	1
Dipole-Dipole	4	1	2
Pole-Dipole	3	2	2

Code 1=best , 4=worse

2.1.3 Electrical Resistivity Tomography

There are three different measuring modes applied into the resistivity method, the vertical electrical sounding, the profiling and the electrical resistivity tomography which is the combination of the two former methods.

The electrical resistivity tomography is actually a composition of both sounding and profiling methods as far as the measurement layout is concerned. The electrical resistivity tomography can be described as a sequence of vertical electrical soundings or as a series of profiling with increasing electrode separation above an area of interest (Figure 2. 4).

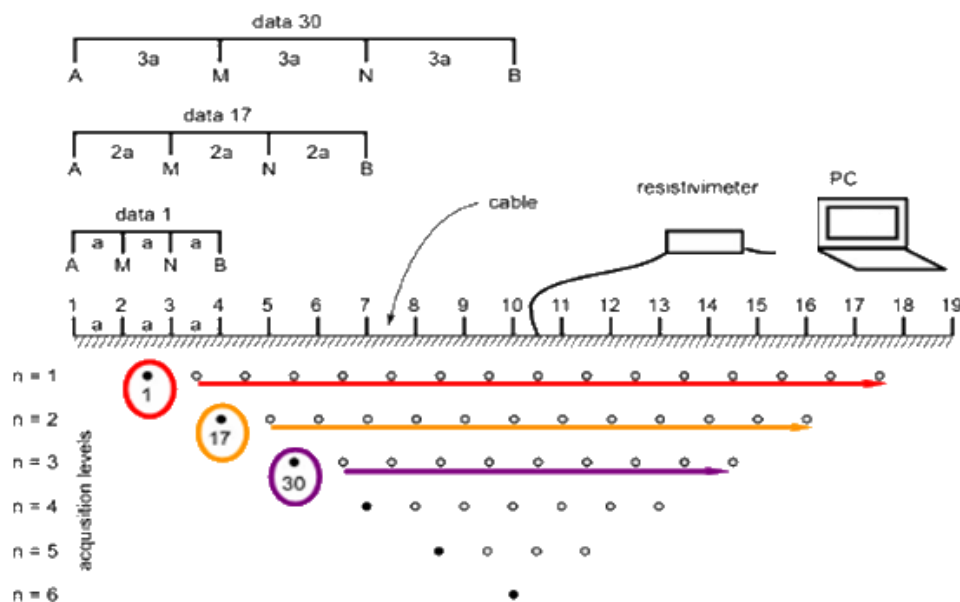


Figure 2. 4. Electrical Resistivity Tomography survey.

Over the last decades two major technological advents contributed to the development of this technique. Firstly, the improvements into the instrumentation (i.e. new resistivity meters, automated electrode switching) and secondly, the development of sophisticated interpretation algorithms in combination to the tremendous increase in

computing power which allowed the automated and efficient processing of the increased number of the collected data.

In the electrical resistivity tomography method a significant amount of data is being collected, in order to increase both the lateral and vertical resolution. Further due to the automated data collection data from boreholes and/or automatic monitoring stations can be obtained effortlessly and in a reasonable amount of time. The improvement in computational power, lead to the development of several algorithms which process these data and retrieve the resistivity distribution of the subsurface given the field measurements.

2.2 Induced Polarization

The Induced Polarization IP method can be considered as an extension of the resistivity method as commonly IP data can be measured using the same configuration and instrumentation with the electrical resistivity tomography (ERT) method.

First of all, to avoid the polarization of the current electrodes (source) due to the gathering of the free anions, the injected current changes polarity so the current injected has the form of a square wave that shifts polarity periodically (0.250 – 4 seconds) as can be seen in Figure 2. 5 (left).

In the induced polarization method, in combination with resistivity measurements, one additional parameter is calculated, called apparent chargeability and it is related to the ability of the ground to store current in form of electrical energy during the injection of the current. The ground in this situation acts very similar to a capacitor.

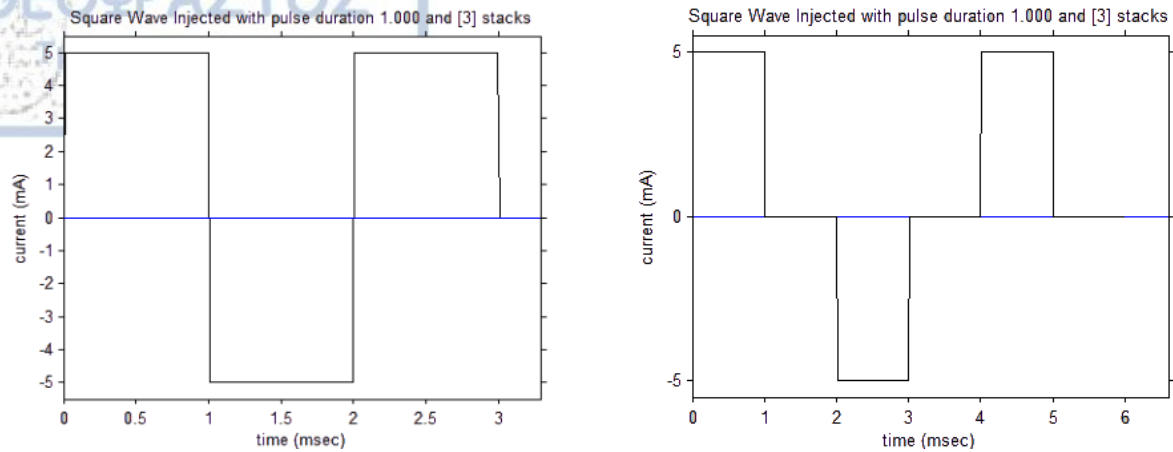


Figure 2. 5. Square wave used for current injection in resistivity method (left) and IP method (right).

In order to measure the energy stored, after each injection (on time) there is an intermediate pause step where no current is injected (off time), as can be seen in Figure 2. 5 (right). In this time (off time) the stored energy is released from the buried bodies making them act as a secondary sources themselves. The voltage of this secondary electrical field is being measured by the instrument at the potential electrodes as a secondary voltage meaning that, when the current turns off, the potential drops gradually before it zeroes due to the presence of this secondary field (Figure 2. 6).

The ratio between the secondary voltage immediately after the current turns off (V_m) and the primary voltage, while the current was on (V_s), is the so-called chargeability, η , as defined by Seigel (1959). The changes of the voltage over time while the current is on and off can be seen in Figure 2. 6.

$$\eta = \frac{V_s}{V_m} \quad (2.6)$$

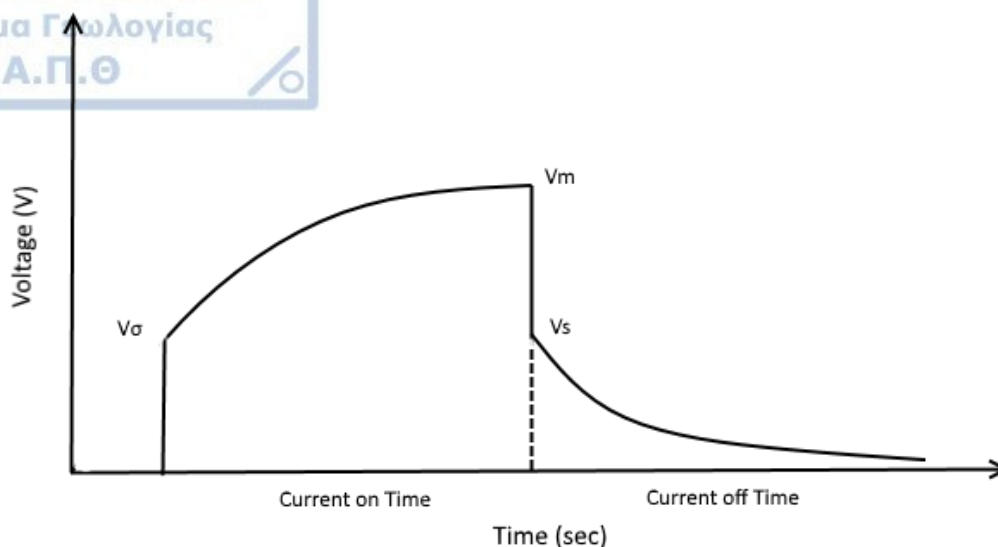


Figure 2. 6. Voltage over time during IP current on and off times.

In reality, the secondary voltage, V_s , cannot be accurately measured because when the current is turned off, because electromagnetic effects are produced and add “noise” to the measured secondary voltage.

To neutralize the effect of electromagnetic noise that is produced by the immediate cut of the current, measurements are being obtained after a delay (delay time is calculated on the pulse duration) i.e. measure IP after the electromagnetic signal attenuates.

After this delay, the voltage is measured at different times in order to record the decreasing voltage. The integral of the curve (Figure 2. 7) yields the apparent chargeability of the measurement. The instrument used in this work is the Syscal Pro which has the ability in addition to the recording of the apparent chargeability to measure up to 20 different time windows, meaning the apparent chargeability in a given time limit.

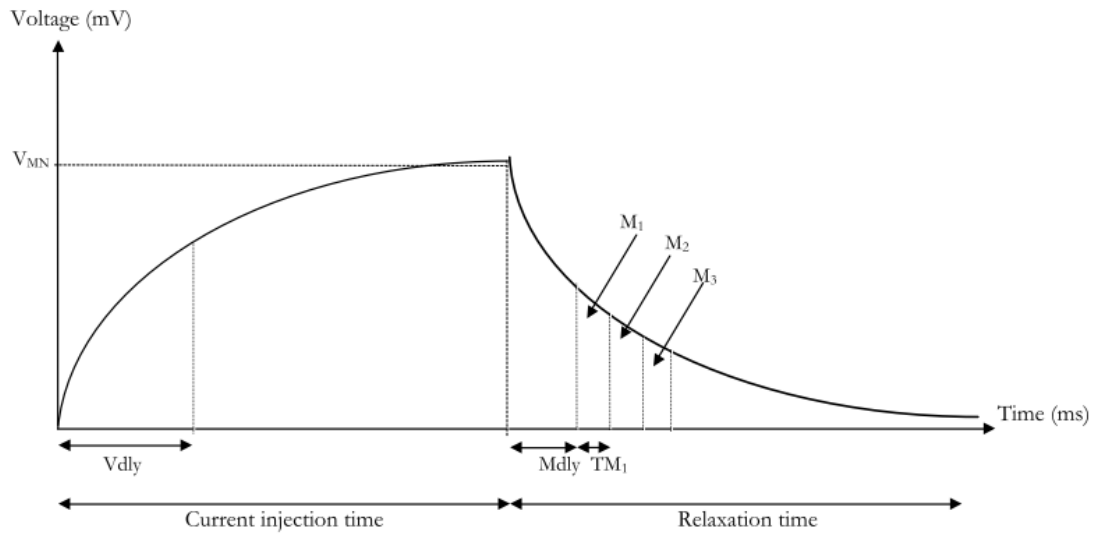


Figure 2. 7. Typical IP voltage curve (from Syscal Pro manual).

It is obvious that the chargeability as described above is a unit less parameter which can never be more than 1 V/V (Seigel, 1959), however for practical we tend to map this value to the range of 1000 mV/V. On the other hand the apparent chargeability values could range from -1 to 1 as negative apparent chargeability values can be encountered and explained in view of negative sensitivity areas (Dahlin and Loke, 2015).

Furthermore, based on the Cole-Cole electrical circuit model the shape of the decay curve is affected by three parameters the true chargeability and the so-called Cole-Cole parameters τ (relaxation time) and c (frequency dependence). The formula that calculates the time domain IP decay curve on the basis of the Cole-Cole model is given by Pelton (1978):

$$\eta(t) = \eta_0 \sum_{n=0}^{\infty} \frac{(-1)^n \left(\frac{t}{\tau}\right)^{nc}}{\Gamma(1 + nc)} \quad (2.7)$$

Where

η_0 : is the intrinsic chargeability of the earth

τ and c : are the Cole-Cole model parameters

η : is the calculated chargeability at the given time t

These three parameters (η_0 , τ and c) affect the shape of the decay curve differently. The intrinsic chargeability, η_0 , is the point in the chargeability axis for $t=0$, meaning that the bigger the value of η_0 the higher the curve that will intersect the y-axis (Figure 2. 8).

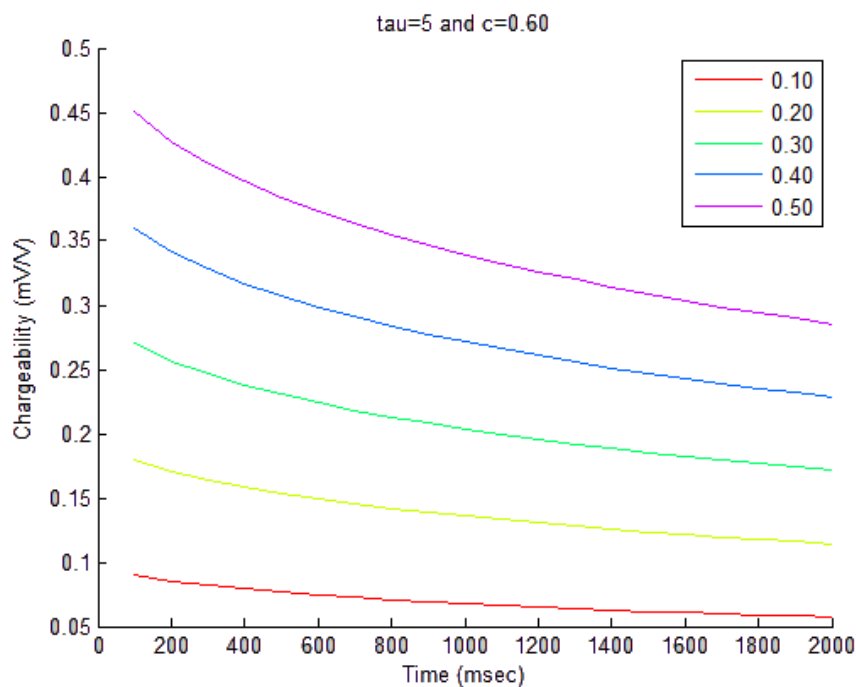


Figure 2. 8. Decay curve for different intrinsic chargeability values.

The relaxation time, affects the rate of decrease in voltage drop, meaning that the higher the τ is, the slowest the energy stored is released. Looking at the graph of Figure 2. 9 as the value of τ increases, the voltage decays slower especially at late times.

The frequency dependence value, c , affects the curvature of the decay curve. The lowest the value the highest the curvature of the decay curve (Figure 2. 10).

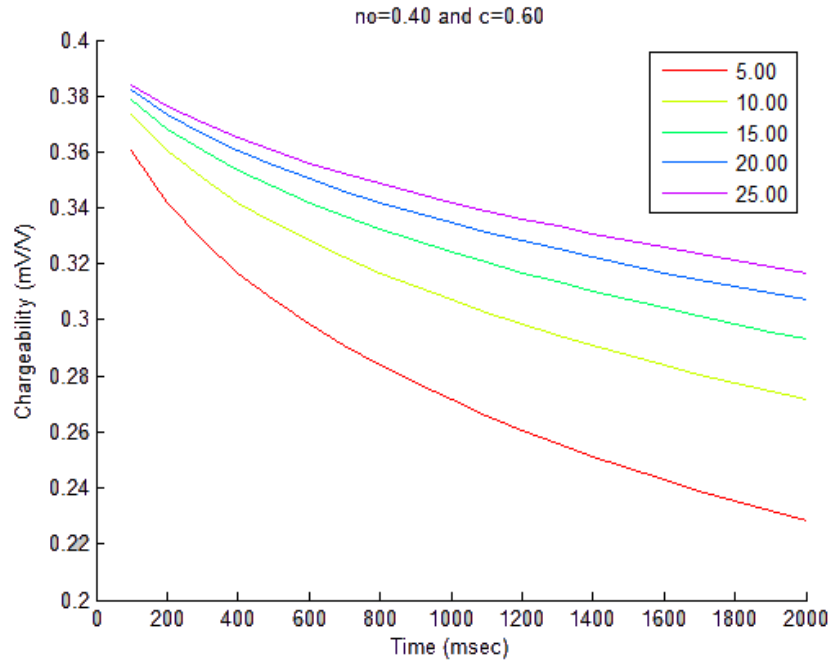


Figure 2. 9. Decay curve for different relaxation time (τ) values.

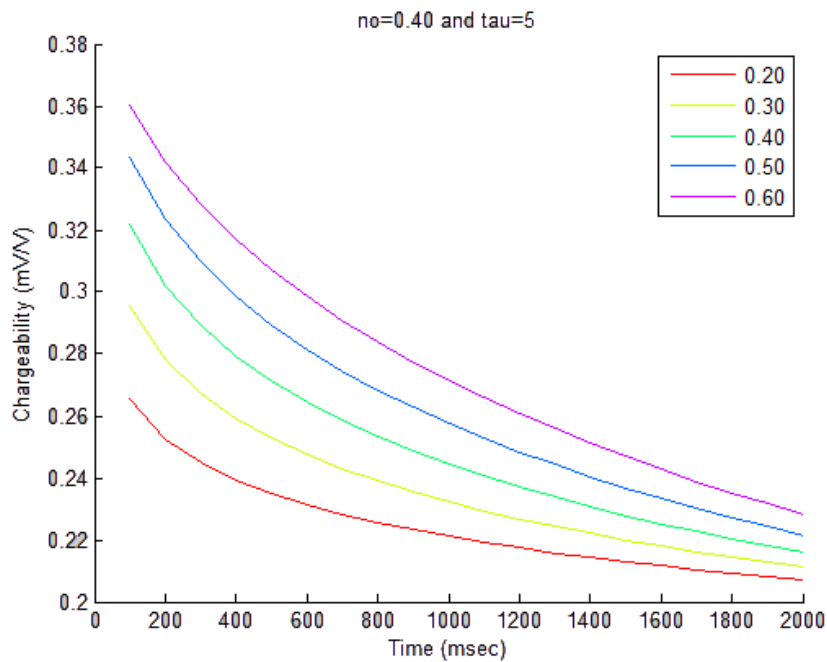


Figure 2. 10. Decay curve for different frequency dependence (c) values.

In this work the Cole-Cole model has also been used as a basis for the production of the synthetic data and the retrieval of the TDIP parameters.

2.3 Forward Modeling

The solution of the forward resistivity problem was used extensively in this work, for producing synthetic data. Furthermore, the solution to the forward problem is necessary for the transformation of the apparent electrical resistivity to electrical resistivity. Detailed description of the solution of the forward problem can be found in literature (Tsourlos, 1995; Tsourlos and Ogilvy, 1999; Karaoulis, 2009) so only a summary will be described here.

The forward modeling involves the calculation of the response of a model representing the earth's structure for which the electrical resistivity distribution is known. To solve this problem, for given source locations the current flow inside the model needs to be simulated. The equation that governs the current flow in the ground is the Poisson equation:

$$\nabla (-\sigma \nabla V) = \nabla J \quad (2.8)$$

Where V is the potential, σ represents the subsurface conductivity and J describes the current sources.

The analytical solution of eq. 2.8 can only be achieved for simple bodies such as a buried sphere (Cook and Van Nostrand, 1954) and does not exist for complex structures. So the equation is solved using a numerical approach: the differential equation which refers to the continuous space needs to be discretized and solved at selected points. Among the numerical methods used to solve the forward geoelectrical problem the most popular are the Integral Equation Method (Keller, 1966; Lee, 1974;

Furness, 1992; Dabas et al, 1994; Lesur et al, 1999), the Finite Difference (Ellis and Oldenburg, 1994; Park and Van, 1991) and the Finite Element Method (Pridmore et al, 1981; Sasaki, 1994; LaBrecque et al, 1996; Tsourlos and Ogilvy, 1999; Pain et al, 2002; Yi et al, 2001).

The algorithm used in this work is based on the Finite Element Method and for that reason this method will be further explained. The Finite Element Method has the advantage of allowing the simulation of topography very easily.

2.3.1 Finite Element Method

The Finite Element Method was developed for mechanical and civil engineering problem solving (Zienkiewicz and Taylor, 1989), but later on found application in many areas such as electromagnetics, acoustic, heat and water conduction and recent advancement in computer power allowed the method to be used widely for more general differential equations problem solving.

For the 3D geoelectrical case the ground is divided into homogeneous and isotropic hexahedral cells called elements. Simple interpolator functions (trial functions) are used to approximate the unknown potential at each vertex (called node) of every element and are combined to generate the element equations. As elements are part of a mesh and they share nodes element equations are assembled to form a large set of linear equations.

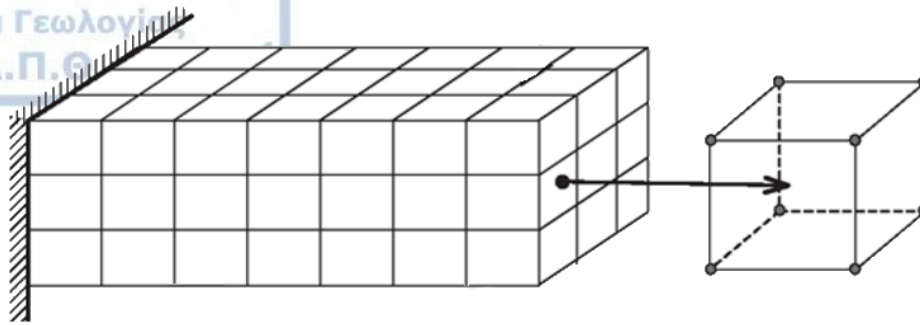
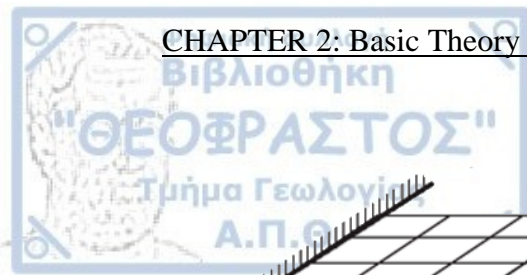


Figure 2. 11. Finite Element Mesh (left), hexahedral element and nodes (right).

The FEM global system and the equations takes the form of:

$$F = K * U \quad (2.9)$$

Where the matrix F contains the current injection sources and boundaries conditions, the matrix K (stiffness matrix) contains the nodal co-ordinates and element resistivities and the vector U contains the nodal electrical potential.

The boundary conditions applied are the Neumann BC (at the air earth interface there is no current perpendicular to the boundary) and the Dirichlet BC (the element mesh is designed in a way that value of the potential at the side and the bottom boundaries is zero). The former is enforced into the element equation and the latter is enforced in the global system equation.

The final step is to solve the system of equations (eq. 2.9) and obtain the vector U which has the potential for each node. To achieve that, the conjugate gradient method for solving large linear systems (Press et al, 1992) was used in the algorithm used in this work. As long as the potential is known at every node the potential difference (i.e. point to point differences) and thus the apparent resistivity can easily be calculated. A simplified way of illustrating the basic principle of FEM is illustrated in Figure 2. 12.

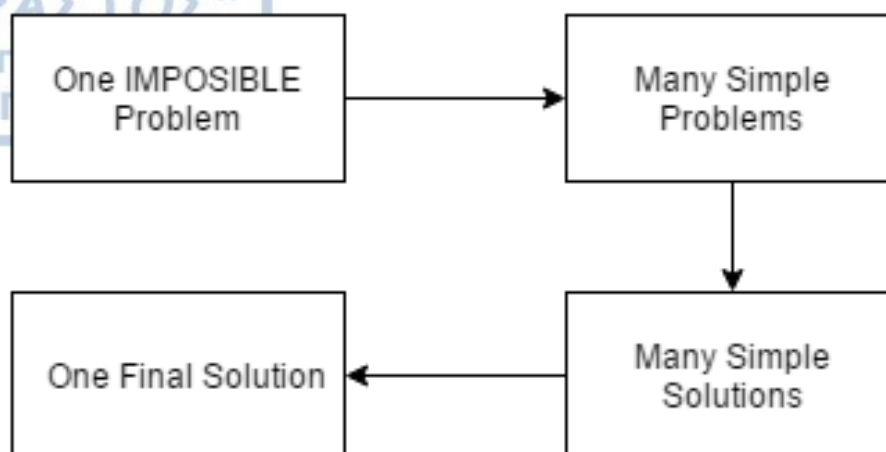


Figure 2. 12. Simplified overview of the Finite Element Method.

The forward geoelectrical problem is a 3D problem, thus a 3D finite element mesh needs to be created to solve that problem and that requires a lot of computing power especially for large sized grids. There are algorithms that can solve the problem in 2.5D, which dramatically reduces the computing power, however, in this work the models were produced using 3D scheme for two reasons: to achieve more realistic modeling scenarios with bodies having a full 3D geometry, and to develop a scheme which can later be further extended to support 3D surveys.

2.4 Inversion

As previously described, it is possible to calculate the response of an array if the earth's model is known. However, in practice the earth's model needs to be determined by the response (the obtained measurements) and the process by which this is achieved, is called inversion.

Inversion can be described as an iterative process that tries to find the earth's model which generates measurements that best fit the real data. It is obvious that this can only happen only if the forward model solution is known, hence all geoelectrical inversion schemes require a robust forward solver integrated within their flow.

There are many algorithms proposed for the solution of the inverse problem such as the least square inversion (Lines and Treitel, 1984), the eigenvalues method (Lanczos, 1960; Golub and Reinsh, 1970), the damped least-square method (Levenberg, 1944; Marquadt, 1963) and the smoothness constrained inversion (Tikhonov, 1963; Constable et al, 1987).

The geoelectrical problem is non-linear which suggests that its solution can be achieved by solving many linear problems. The general form of the iterative linear problem has the form:

$$dy = J dx \quad (2.10)$$

Where dx is vector containing the correction of the model parameters for every iteration, dy is the vector containing the differences between the real and modelled data corresponding to the current model estimate and J is the Jacobian matrix for the same model. The calculation of the Jacobian matrix (sensitivity matrix) can be achieved, with some modifications, with the same finite element scheme used to calculate the synthetic data (Tsourlos, 1995).

The Jacobian matrix connects the observed data with the resistivity of the model subsurface parameters. The size of the Jacobian matrix is $[m \times n]$ where m is the number of measurements and n is the number of parameters. Each element of the Jacobian matrix is the partial derivative of the model parameter with respect to the model measurement (eq. 2.11). In other words it is a metric of how much a particular measurement (apparent resistivity) will change for a given small change of the resistivity of a subsurface region, hence it's also called sensitivity matrix.

$$J_{ij} = \frac{\partial dy_i}{\partial dx} \quad (2.11)$$

As the direct solution of equation (2.10) is inherently unstable several ways for stabilizing the inversion technique have been proposed.

The most popular is to include a smoothness constrain into the inversion. The resistivity correction at every iteration is now given by:

$$dx = (J^T J + \mu C^T C)^{-1} * J^T * dy \quad (2.12)$$

Where the new resistivity estimate is given by:

$$x_{new} = x_{old} + d_x \quad (2.13)$$

C is the smoothness matrix and μ is the so called Lagrangian multiplier. The smoothness matrix C describes the smoothness relations of every parameter with its neighboring ones (Figure 2. 13), while the Lagrangian multiplier μ is a number which decides the overall amount of smoothness that the solution will have.

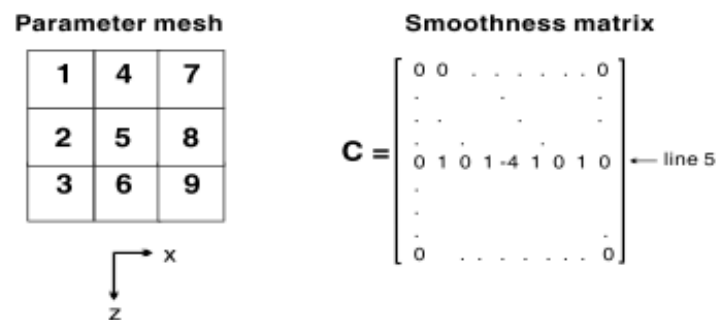


Figure 2. 13. Smoothness matrix for a 9 parameter model (Tsourlos, 1995)

This kind of smoothness is called model roughness constrain and allows the computed model parameters to be smooth in space (Figure 2. 13). Furthermore, there are other similar types of constrains that can be used depending on the problem, such as the time constrain (in time lapse inversion) and channel constrain (in spectral IP data inversion).

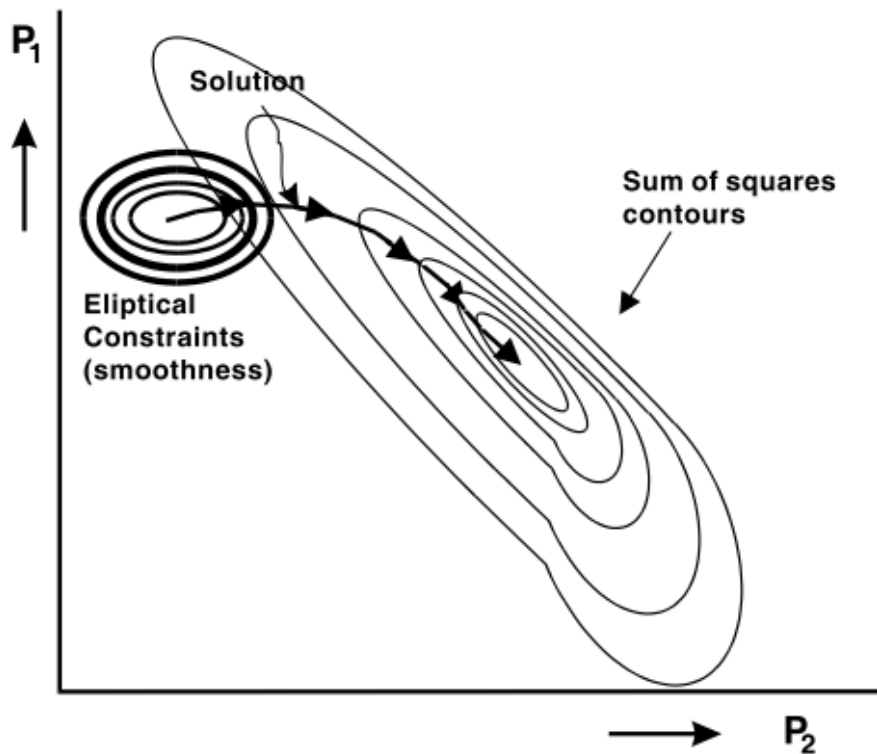


Figure 2. 14. Smoothness constrain for two parameter (p_1 , p_2) space (after Box and Kanemasu, 1972).

The inversion procedure involves subdividing the model space into cells (parameters) and the goal is to calculate for each parameter its electrical resistivity given the observed data. The inversion process is depicted in the simplified flow diagram of Figure 2. 14.

To begin with, the initial model most commonly used is the one for homogeneous earth. As long as each model parameter has a value for its electrical property (resistivity, chargeability), the model response is calculated (forward solution) and the modelled data is compared with the observed measurements and the model misfit is then computed.

The model misfit is expressed by the Root Mean Square (RMS) error between the observed and the calculated measurements.

If one of the stopping criteria is met the process terminates, otherwise the process repeats all over again: the Jacobian matrix for the new model is calculated the Lagrangian multiplier is updated a new inverted model correction is retrieved by solving equation (2.12). Finally the subsurface resistivity is updated based on eq. 2.13.

There are many stopping criteria that can be defined. The process can terminate when there is no significant improvement of the RMS error or when the RMS increases (divergence) or when the model misfit becomes less than a predefined level (i.e. on the basis of the observed data errors) or when a certain number of iterations is reached. (e.g. 7 iterations).

The flowchart representing the inversion process, as previously described, can be seen in Figure 2. 15.

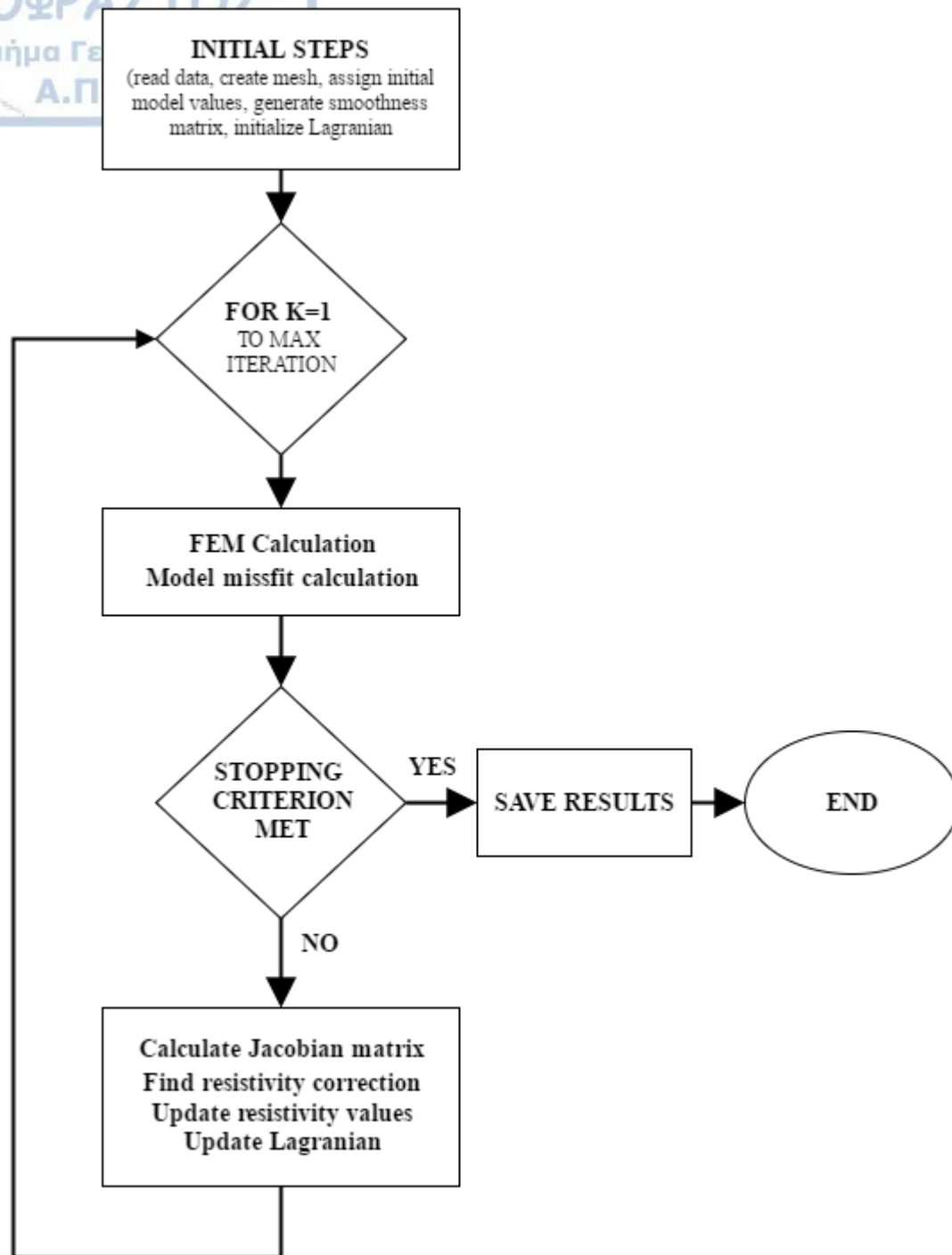
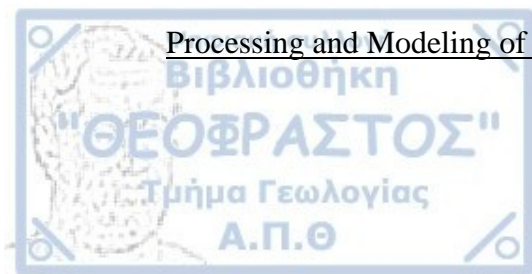


Figure 2. 15. Simplified flowchart of the inversion process.



CHAPTER 3

Modeling and Inversion tools of Time Domain IP (TDIP) Data

In this chapter the DC-TDIP modeling and inversion tools that were used in this work are presented.

For DC-TDIP 3D modeling an existing 3D FEM based DC forward solver was modified in order to incorporate the 3D modeling of the time domain IP data. The software can produce the 3D TD IP synthetic data for an arbitrary property distribution based on the Cole-Cole model.

Subsequently, the inversion of the TDIP data was performed using a special version of the DC2D PRO software, which applies a smoothness-constrained inversion by introducing inverse model regularizations not only for the space domain but also for the channel domain (similar to the introduced time lapse regularization).

The results of the smoothness TDIP inversion were then used to form the intrinsic chargeability curves for each model cell. Those curves were further processed by a matlab based tool that was developed within the framework of this work and calculates the Cole-Cole parameters for each model cell, using the Particle Swarm Optimization algorithm. The algorithmic details and only some test runs of this program are presented in this chapter as a more detailed analysis of its performance is presented in Chapter 4 and Chapter 5.

3.1 Modeling of Time-Domain Induced Polarization (TDIP) Data

3.1.1 Algorithm Description

The algorithm used in this work is an extension of an existing proven scheme developed by Tsourlos and Ogilvy (1999). The existing algorithm supported only DC/IP forward modeling in 3D so it was modified to incorporate the TDIP modeling that was required in this work. The C language program and the modifications made allows the calculation of the Induced Polarization response for each user-defined time channel based on the Cole-Cole model.

The basic structure of the existing 3D DC forward modeling algorithm is presented in detail by Tsourlos and Ogilvy (1999) so only a brief description is presented here.

The existing algorithm seeks to find a solution of the basic differential equation that describes the flow of DC current in inhomogeneous earth. As no analytical solution exists this is being achieved by using the finite element method (FEM). The subsurface is subdivided into smaller sub-regions (elements) which are considered to be geoelectrically homogeneous and for the 3D case they are hexahedrals. In each element the electrical potential is approximated by simple functions which connect the vertices of the elements which are called nodes forming a set of equation for each element. As elements have common nodes all element equations can be assembled into a single global system of equations which is then solved under certain boundary conditions. So the FEM algorithm will produce the solution of the electrical potential at every node given an electrical current source and a geoelectrical property distribution. Then, it is simple to calculate the potential differences and the respective apparent resistivities for any given array configuration.

3.1.2 Induced Polarization (IP) Modeling

The modeling of the induced polarization (IP) response is directly linked to the modeling of the resistivity data. It can be assumed that the IP effect is described by the chargeability (m), in the way defined by Seigel (1959), as a unit-less parameter confined between the values $[0,1]$. If for every model cell (i.e. element) a chargeability value is defined the calculation of the Induced Polarization response of the model can be obtained by additionally solving the same geoelectrical forward equations assuming that the electrical resistivity of the i_{th} model cell (i.e. element) is modified to a new value ρ_{im} based on the equation:

$$\rho_{im} = \rho_i * (1 - m_i) \quad (3.1)$$

Where ρ_i is the intrinsic electrical resistivity and m_i is the intrinsic chargeability of the i_{th} cell.

Finally, the apparent chargeability vector, m_a , is calculated using the formula:

$$m_a = \frac{d - d_m}{d} \quad (3.2)$$

Where d is the vector that stores the apparent resistivity of the original resistivity distribution and d_m is the vector containing the modified apparent resistivity as calculated from eq. 3.1).

3.1.3 Time Domain Induced Polarization (TDIP) Modeling

In order to include the calculation of the time domain IP response a modification of the existing algorithm was necessary. The forward calculation involves now the repetition of the IP calculation for as many folds as the time windows we need to model.

A modified intrinsic resistivity of each model block corresponding to each time window needs to be calculated and inserted into the solver. In this case, the forward solver will run once for the calculation of the apparent resistivity and it will be followed by the steps required for calculation of the TDIP response for each user-defined time window.

The electrical resistivity of the i_{th} model cell (i.e. element) for each user-defined time window t is modified to a new value ρ_{im}^t based on the equation:

$$\rho_{im}^t = \rho_i * (1 - m_i^t) \quad (3.3)$$

Where ρ_i is the intrinsic electrical resistivity and m_{ti} is the intrinsic chargeability of the i_{th} cell for time window t . The intrinsic chargeability m_{ti} for each individual time window is calculated internally prior to the forward solution by using the equation which describes the voltage's decay based on the Cole-Cole model (eq. 2.7 repeated from chapter 2):

$$\eta(t) = \eta_0 \sum_{n=0}^{\infty} \frac{(-1)^n \left(\frac{t}{\tau}\right)^{nc}}{\Gamma(1 + nc)} \quad (2.7)$$

Finally, the apparent chargeability vector, \mathbf{m}_a^t , is calculated using the equation:

$$\mathbf{m}_a^t = \frac{\mathbf{d} - \mathbf{d}_m^t}{\mathbf{d}} \quad (3.4)$$

Where \mathbf{d} is the vector that stores the apparent resistivity of the original resistivity distribution and \mathbf{d}_m^t is the vector containing the modified apparent resistivity as calculated from eq. 3.13.

The final results are then merged internally and form the time domain apparent chargeability measurement matrix.

The modified flow-chart of the algorithm which includes the calculation of the TDIP forward response is shown in Figure 3. 1. The spectral IP responses can now be calculated for complex structures, using the finite element method in the 3D domain. Even though this process is time consuming because as described the forward solution needs to be calculated for each individual channel separately, the 3D solution is chosen over the 2D forward solution to incorporate for prisms with discrete boundaries. For this reason, the data used in this work were produced by using a full 3D model.

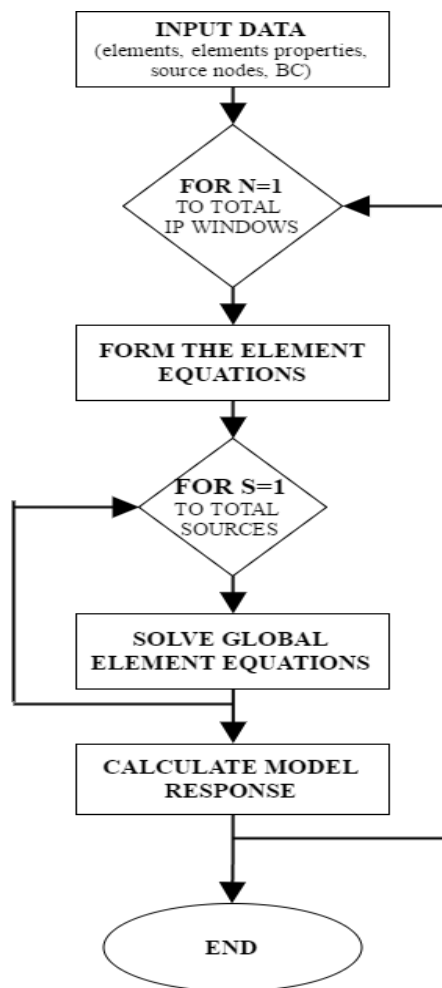


Figure 3. 1. Modified version of the algorithm used for the forward modeling.

3.1.4 TDIP Program

In this section the steps required to create the 3D model, and calculate its TDIP response are explained and demonstrated by a test model run.

Initially the measurement array configuration for which the forward solution will be calculated needs to be defined. This step requires the creation of a file which contains the locations of the electrodes. Each line represents a different measurement, and contains the location (x, y and z coordinate) of the electrodes that are needed for that specific measurement (Figure 3. 2).

Ax	Ay	Az	Bx	By	Bz	Mx	My	Mz	Nx	Ny	Nz
0.00	0.00	0.00	1.00	0.00	0.00	2.00	0.00	0.00	3.00	0.00	0.00
1.00	0.00	0.00	2.00	0.00	0.00	3.00	0.00	0.00	4.00	0.00	0.00
2.00	0.00	0.00	3.00	0.00	0.00	4.00	0.00	0.00	5.00	0.00	0.00
3.00	0.00	0.00	4.00	0.00	0.00	5.00	0.00	0.00	6.00	0.00	0.00
4.00	0.00	0.00	5.00	0.00	0.00	6.00	0.00	0.00	7.00	0.00	0.00
5.00	0.00	0.00	6.00	0.00	0.00	7.00	0.00	0.00	8.00	0.00	0.00
6.00	0.00	0.00	7.00	0.00	0.00	8.00	0.00	0.00	9.00	0.00	0.00

Figure 3. 2. Sample of the file that contains the array's geometry information.

An auxiliary program was used to generate 3D measurement protocols as merged 2D measurement lines given the model space and the general electrode geometry (i.e. electrode spacing, electrode number in X, Y direction) for commonly used array configurations. It is noted however that the program can cope with any custom made electrode array and more complex protocols files if this is required.

In the following, the user creates the input file for the forward solution software and a typical sample of it is given in Figure 3. 3. In the first section of this file the model size information is required for memory allocation purposes. After this, the type of the model solution is chosen (DC or DC/TDIP) and the array type along with the input (array configuration) and output (results) ASCII text files.

In the last section of the file the electrical properties of the background are defined along with the number of prisms that the model contains.

For the background the model requires the resistivity and chargeability as well as the Cole-Cole properties τ (relaxation time) and c (frequency dependence). The IP properties should be included into the input file only if program is asked to perform IP modeling. The format of the background model is shown in Table 3. 1 and an application example is presented in Figure 3. 3.

\$Background_resistivity and_IP

bgr_res, bgr_chrg, bgr_τ, bgr_c

bgr_res= model's background resistivity in Ohm-m.

bgr_chrg= model's background chargeability (m) which is a unit-less number between [0, 1).

bgr_τ = model's background relaxation time τ (Cole-Cole parameter)

bgr_c= model's background frequency dependence c (Cole-Cole parameter).

Table 3. 1. Information for the background.

Furthermore, for the modeling prisms their size needs to be provided in addition to their electrical and Cole-Cole properties with the format which is described in Table 3. 2. The coordinate system is defined by the electrode's coordinates.

It should be noted that in the case of overlapping modeling bodies it is the latest in sequence that overlays to the previous ones. Thus it is essential to place the modeling bodies in the correct order to achieve the correct composite model. An example of how the modeling prisms are inserted is shown in Figure 3. 3.

The final line of the input file requires from the user to specify the number and exact time in msec of the time windows for which the forward response will be calculated (See Figure 3. 3).

\$Info_Prisms

bp

$x_{1i}, x_{2i}, y_{1i}, y_{2i}, z_{1i}, z_{2i}, p_{res_i}, p_{chrg_i}, p_{\tau_i}, p_{c_i}$

.

bp = The number of prisms to be modelled.

$x_{1i}, x_{2i}, y_{1i}, y_{2i}, z_{1i}, z_{2i}$ = The limits of the i_{th} prism along the X, Y, Z axes

p_{res_i} = i_{th} prism background resistivity in Ohm-m.

p_{chrg_i} = i_{th} prism chargeability (m)

p_{τ_i} = i_{th} prism relaxation time τ

p_{c_i} = i_{th} prism frequency dependence c

Table 3. 2. Information for each prism.

```

$3D_MODELLING_INPUT_FILE
$-----
$MAX_PROBES_X
25
$MAX_PROBES_Y
25
$MAX_BR_PROBES
20
$MAX_MEASUREMENTS
2500
$-----
$MODEL_TYPE_ (RES=1, RES+IP=2)
2
$ARRAY_TYPE_ (Wen=1, Dip-Dip=2, Pole-Dip=3, Pole-Pole=4)
2
$DATA_INPUT_FILENAME → array input
dd_24x5_1m
$INFO_OUTPUT_FILENAME
dd_24x5_1m.d
$-----
$BACKGROUND_RESISTIVITY_AND_IP →  $\rho, m, \tau, c$ 
10, 0.01, 1, 0.10
$NUMBER_AND_INFO_FOR_PARALEL
2
7, 10, 0, 5, 2, 4, 2, 0.40, 1, 0.25 →  $x_1, x_2, y_1, y_2, z_1, z_2, \rho, m, \tau, c$ 
14, 18, 0, 5, 2, 4, 2, 0.40, 10, 0.60
$NUMBER_AND_INFO_OF_TIME_WINDOW →  $t_1, t_2, \dots, t_n$ 
10
0.100, 0.200, 0.300, 0.400, 0.500, 0.600, 0.700, 0.800, 0.900, 1.000
$END
    
```

Figure 3. 3. User input file required for the 3D TDIP solver.

After the input file is set, the program is executed running the forward solver for every time window as can be seen at the screen capture of Figure 3. 4.

```

PROBES=> 120
PROBE SPACING X=> 1.000
PROBE SPACING Y=> 1.000
INIT. RESIST.=> 10.000 Ohm-m
=====
*      3-D MODELLING BODIES      *
=====
Number of bodies: 2
Background Res.= 10.000 Background IP.= 0.010
***** x1 x2 y1 y2 z1 z2 res ip
BD1= 7.00,10.00,0.00,5.00,2.00,4.00,2.00,0.40
***** x1 x2 y1 y2 z1 z2 res ip
BD2= 14.00,18.00,0.00,5.00,2.00,4.00,2.00,0.40
***** FEM CALCULATION STARTS *****

NORMALIZING PROCEDURE:
=====
Solving for 120 electrodes:.. 1.. 2.. 3.. 4.. 5.. 6.. 7.. 8.. 9.. 10..
..
..111..112..113..114..115..116..117..118..119..120..

CALCULATING MODEL RESISTIVITY RESPONSE:
=====
Solving for 120 electrodes:.. 1.. 2.. 3.. 4.. 5.. 6.. 7.. 8.. 9.. 10..
..
..111..112..113..114..115..116..117..118..119..120..

CALCULATING MODEL IP RESPONSE:
=====
SIP Inversion Window[1]
Solving for 120 electrodes:.. 1.. 2.. 3.. 4.. 5.. 6.. 7.. 8.. 9.. 10..
..
..111..112..113..114..115..116..117..118..119..120..

SIP Inversion Window[2]

.....
.....
.....
.....

SIP Inversion Window[20]
Solving for 120 electrodes:.. 1.. 2.. 3.. 4.. 5.. 6.. 7.. 8.. 9.. 10..
..
..111..112..113..114..115..116..117..118..119..120..

SIP Inversion Total Chargeability
Solving for 120 electrodes:.. 1.. 2.. 3.. 4.. 5.. 6.. 7.. 8.. 9.. 10..
..
..111..112..113..114..115..116..117..118..119..120..

***** PROGRAM END !!! *****

```

Figure 3. 4. Spectral IP forward solution for 20 window model.

The program finally will save an output file with each line containing the information of every measurement. The file has as many lines as the measurements and each line contains the x, y and z location for the current and potential electrodes, the apparent resistivity and the TDIP response as the calculated apparent chargeability for each time window.

Finally the software also exports synthetic data in a format compatible with existing inversion software (i.e. DC2DPRO, DC3DPRO, RES2DINV) for further processing.

To demonstrate the application of the TDIP modeling software we present an example for the case of the 2 prisms that were inserted using the model input file of

Figure 3. 3. The measuring protocol is dipole-dipole with 24 electrodes at 6 lines spaced 1m apart along X and Y axes.

The X-Z slice of the middle slice of the model can be viewed in Figure 3. 5 and the 3D view of the model can be seen in Figure 3. 6 to fully understand the model's geometry.

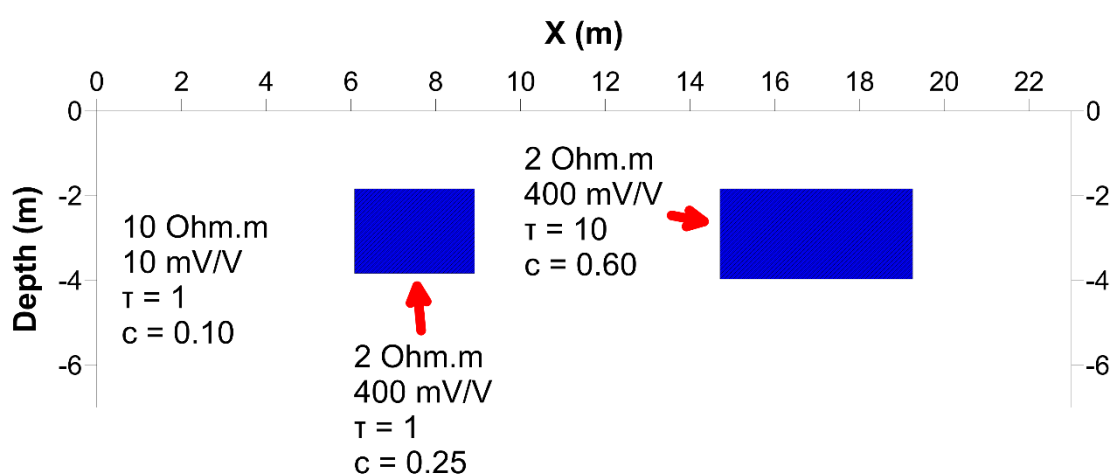


Figure 3. 5. X-Z plain of the middle slice for the example model (prism 1 on the left and prism 2 on the right).

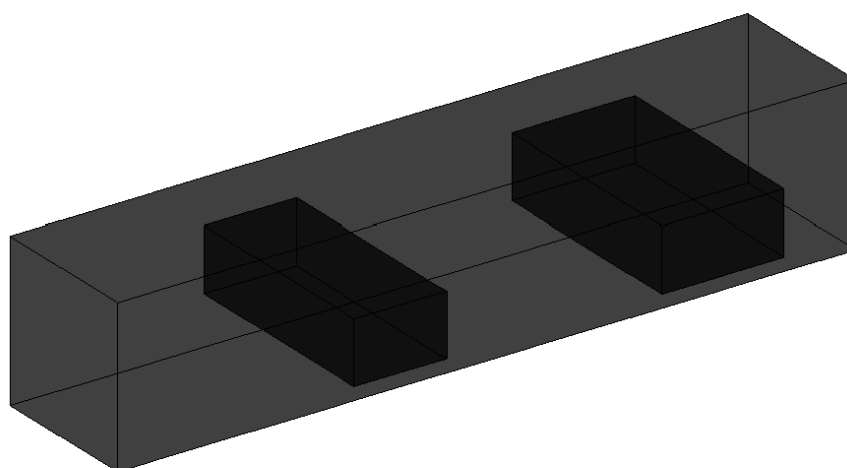


Figure 3. 6. 3D View of the example model's geometry (prism 1 on the left and prism 2 on the right).

The middle 2D dipole-dipole line of the full 3D data set, is exported to be used by the 2D inversion software for further processing. The pseudo section of the apparent

resistivity and apparent chargeability for the 2D middle line are represented in Figure

3. 7.

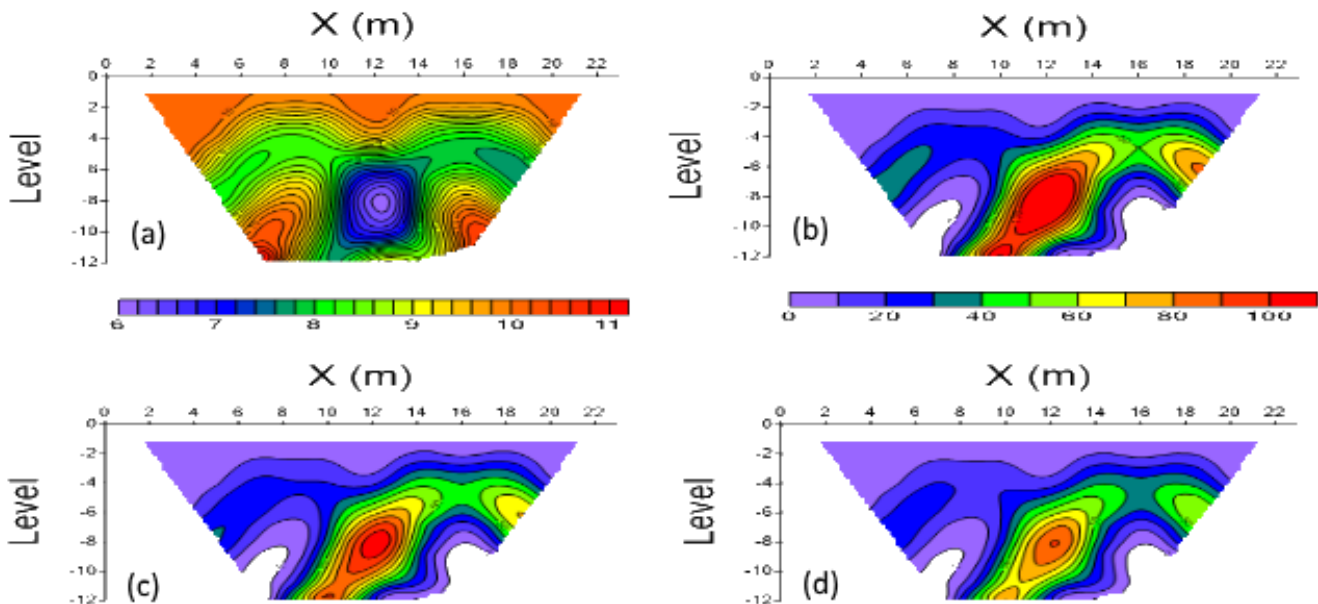


Figure 3. 7. Pseudo section of (a) resistivity, (b) - (d) chargeability for channel 1, 4 and 10.

Furthermore, some typical TDIP curves for selected individual dipole-dipole measurements have been extracted and are shown in Figure 3. 8 representing the decay of the apparent chargeability over time (Figure 3. 8).

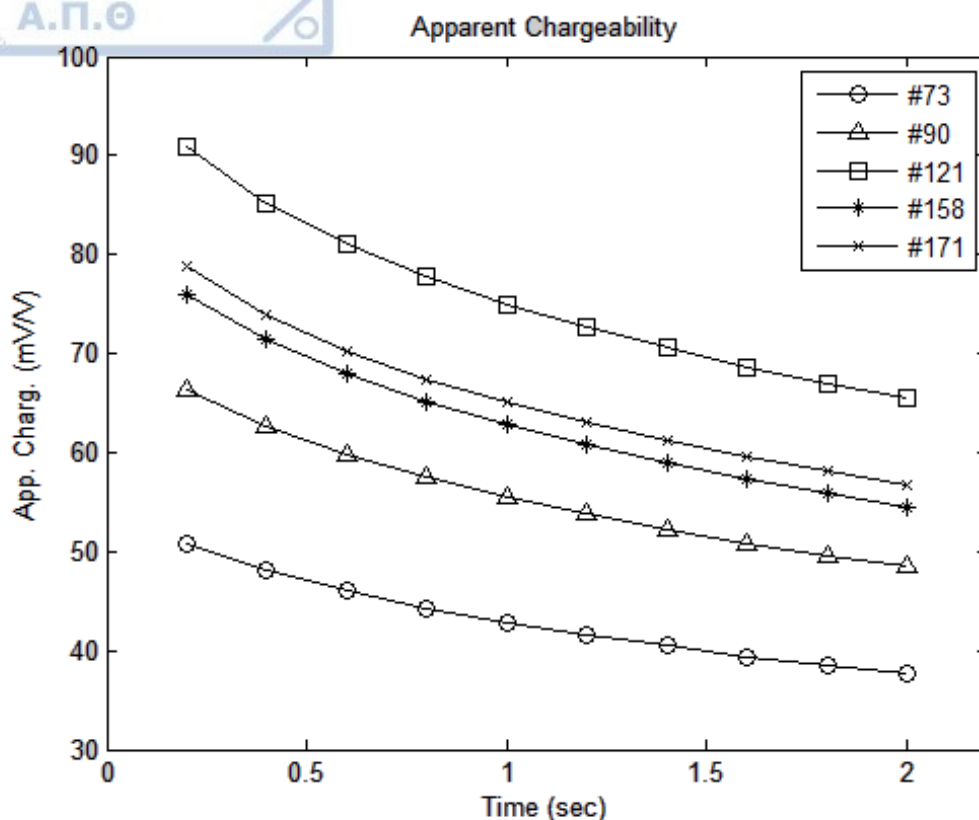
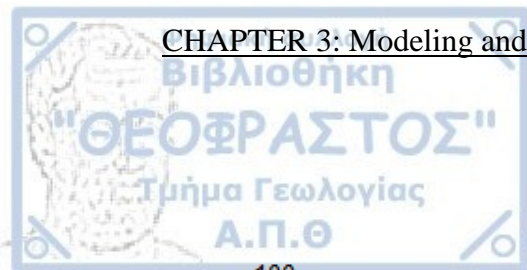


Figure 3. 8. Apparent Chargeability of model measurements.

3.2 Inversion of TDIP data using DC2DPRO

As the TDIP dataset contains the information of the apparent chargeability decay over time for different time windows a special algorithm for inverting the TDIP data had to be used. The inversion software that was used in this work is the DC 2D Pro (Kim 2012), which uses a smoothness constrained inversion method not only for the model but also for the TD channels. The software offers a user-friendly environment that gives numerous options for the user to define.

The inversion of the data for the calculation of the electrical properties distribution and the calculation of the Cole-Cole parameters was made in two dimensions (2D) because currently the combined smoothness constrained inversion for TDIP is supported only for 2D inversion. So although the synthetic responses were

calculated in a full 3D mode (to produce more realistic results for complex geometries) the inversion tests were performed in 2D using 2D data lines extracted from the 3D data.

Over the last 20 years several algorithms were proposed to process the TDIP data (Yuval and Oldenburg, 1997; Johnson et al, 2010) however most of them process the data in an independent mode: the IP data of each time channel is separately inverted. Therefore the inverted chargeability curves may suffer from irregular shapes as they are not constrained to meet the basic forms of the chargeability curves, introducing potential interpretation errors.

To deal with this problem Kim et al., (2012) proposed an algorithm for the simultaneous inversion of the different available TDIP channels which is expected to produce improved results regarding the reconstructed chargeability curves. This was achieved by introducing a smoothness constrain in channel domain in addition to the typical smoothness in space domain.

In this way the inversion of all the IP windows is run simultaneously and this implies that N data sets are simultaneously inverted to seek N different subsurface models of chargeability distribution. The advantage of this approach is that the individual channel inversion results do take into account the results of the neighboring channels. On the other hand, this suggests that the algorithm is extensively demanding in memory and computing resources as it will result into extremely large matrices that need to be inverted: the size of the Jacobian matrix is at least N^2 times larger than the one used in the single step inversion (i.e. resistivity inversion).

3.2.1 Program Operation

The inversion program reads the TDIP data from a formatted file and generates automatically a dense finite element grid, which is used to approximate the solution of the forward problem. It is necessary to have a dense finite element grid in order to achieve greater accuracy in the calculation of the forward model. The same dense grid can theoretically be used to calculate the inverted properties however it is not recommended as this could lead to an extremely underdetermined system. So at the same time a sparser mesh which contains the inversion parameters is also generated.

Both the finite element mesh and the inversion parameter mesh can be directly changed by the user, in the model edit section of the software (Figure 3. 9) prior to the inversion process.

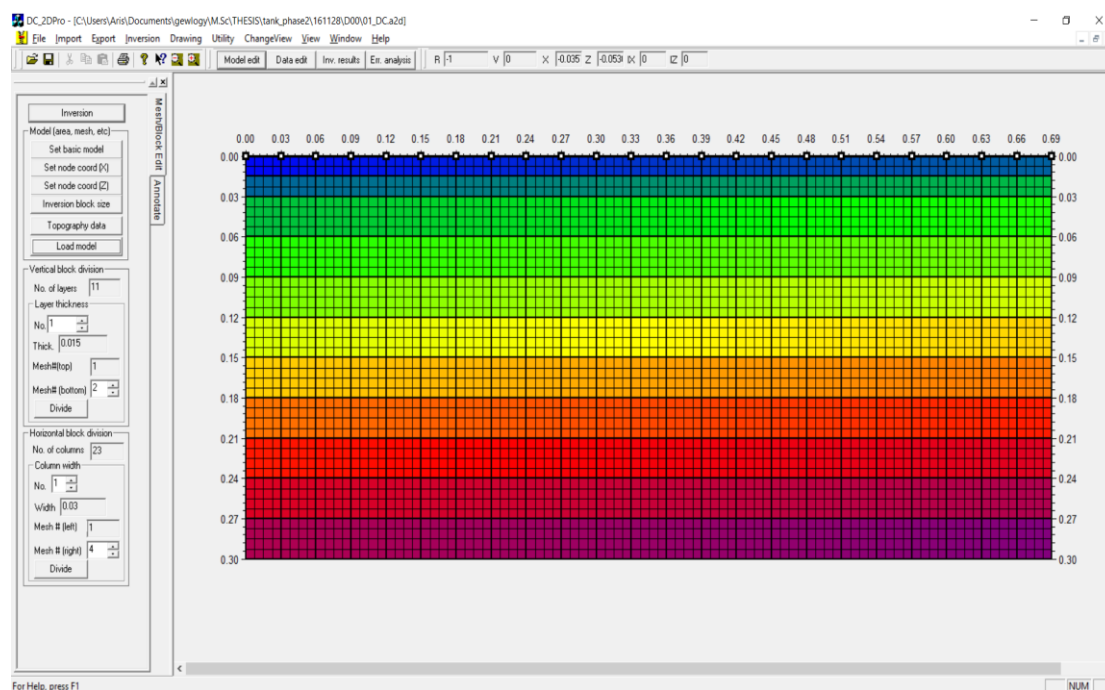


Figure 3. 9. DC2D Pro, model edit.

Furthermore, the software offers the ability to process the data of each model. This can be used to manually remove outliers from a particular dataset and further improve the data quality. This can be done in the model edit section of the software.

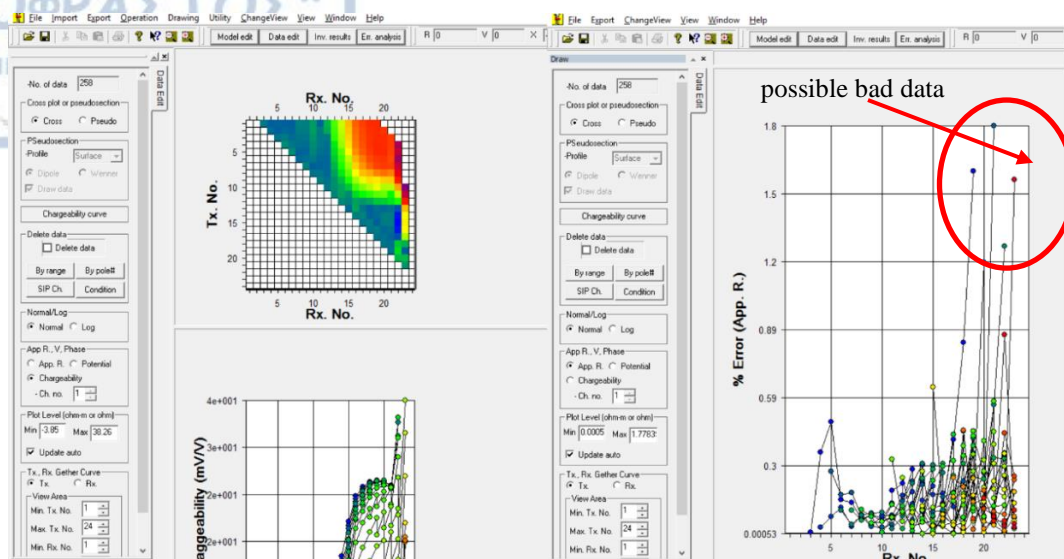


Figure 3. 10. DC2D Pro, data edit (left) and error analysis (right).

Another way to exterminate bad data points, is by using the data misfit. This is basically the root mean square error of each measurement which is computed after the inversion process by comparing the measured apparent resistivity from a single measurement with the matched one from the forward solution of the final earth model that was calculated. This does not necessarily mean that the measurement is bad, however it means that the model cannot reproduce that measurement hence it should not be trusted.

After setting the mesh and checking for possible outliers, the last step is to determine the inversion parameters such as: the maximum number of iterations, the error minimization norm, the model smoothness in channel and in space domain and the values of the Lagrangian multipliers.

Inversion Parameters

- No. of iterations: 6

Regularizations

Error minimization: ☐ L2 norm ☒ L1 norm

Model smoothness (space): ☒ L2 norm ☐ L1 norm

Lagrangian multiplier: ☒ Automatic update (Weight: 0.05) ☐ Constant (0.1) ☒ From ACB (Max: 1, Min: 0.01)

Differential smoothing: ☒ Differential weighting (X, Z) (Horizontal smoothing factor: 1)

Model smoothness (4-D): ☐ L2 norm ☒ L1 norm

Roughness minimization: ☐ L2 norm ☒ L1 norm

Lagrangian multiplier: ☒ Automatic update (Weight: 0.5) ☐ Constant (0.1) ☒ From ACB (Max: 1, Min: 0.01)

Space-Time dependency: ☒ Constant ☐ Time dependent ☐ Space-Time dependent

☐ Incorporate resolving power

Inverted Data

Max. absolute value: 21.1973

Min. absolute value: 3.06607

☒ Exclude negative app. r.

Set resistance weighting

OK Cancel

Run DC/SIP inversion Run DC/4D inversion

Figure 3. 11. Spectral IP Inversion parameters used.

The inversion parameters that were used for the Spectral IP inversion can be seen in (Figure 3. 11). After the spectral IP inversion process is over the chargeability distribution has been calculated N times for every model cell, where N is the number of windows that were available in the TDIP data. In Figure 3. 12 the inversion models of the chargeability for different time channels are shown for the case of the 2 prisms model (Figure 3. 5).

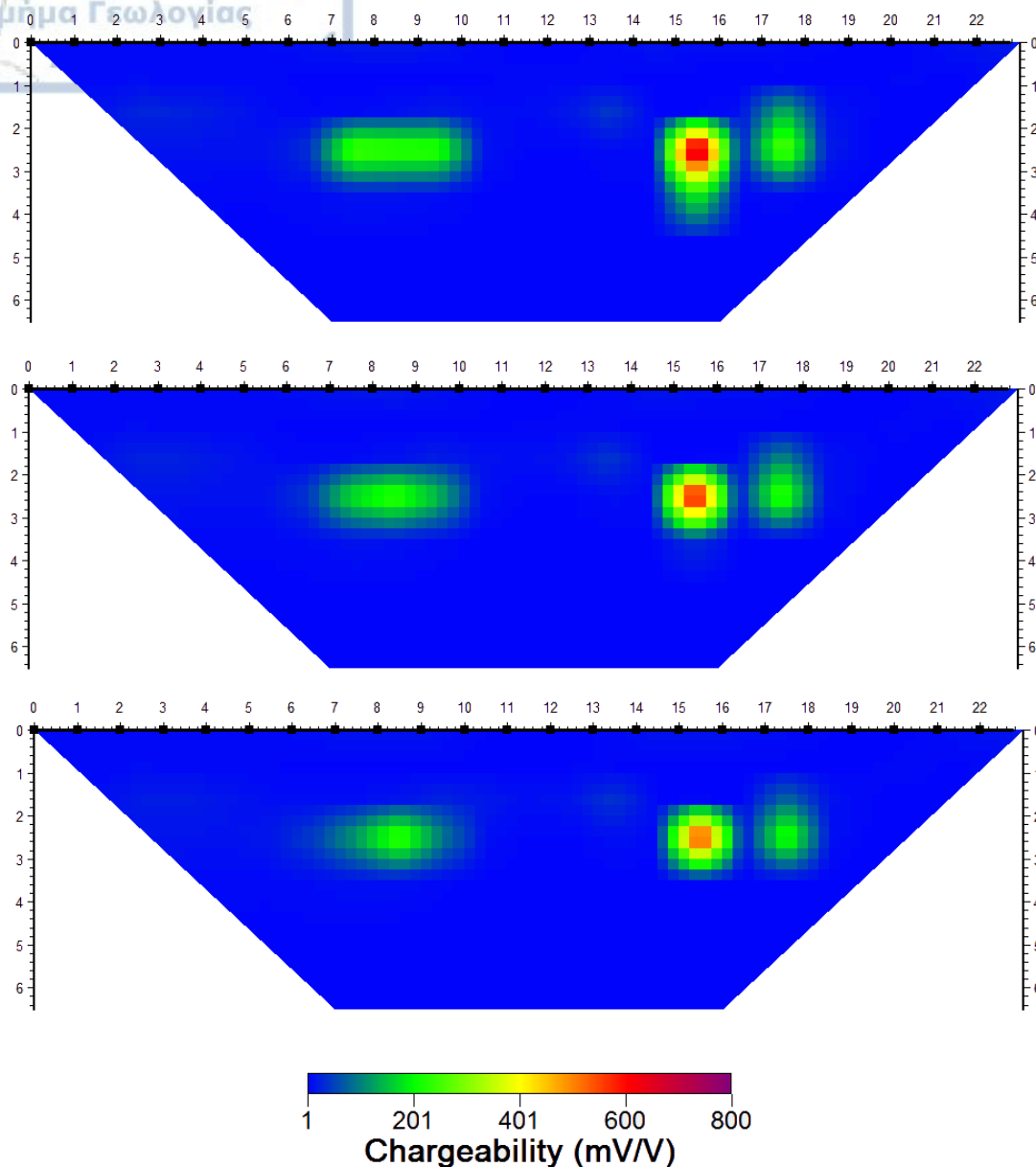


Figure 3. 12. Inverted chargeability values for Channel 1 (top) Channel 5 (middle) and Channel 10 (bottom).

That means that for each cell, N different chargeability values have been calculated, with each value correspond to a different time window. Those values can be used to form the intrinsic chargeability curves for each model cell (Figure 3. 13). The software offer the option to export the spectral information, the calculated value for each cell for every time window, in an ASCII format file. This file can be used to visualize and further process the result.

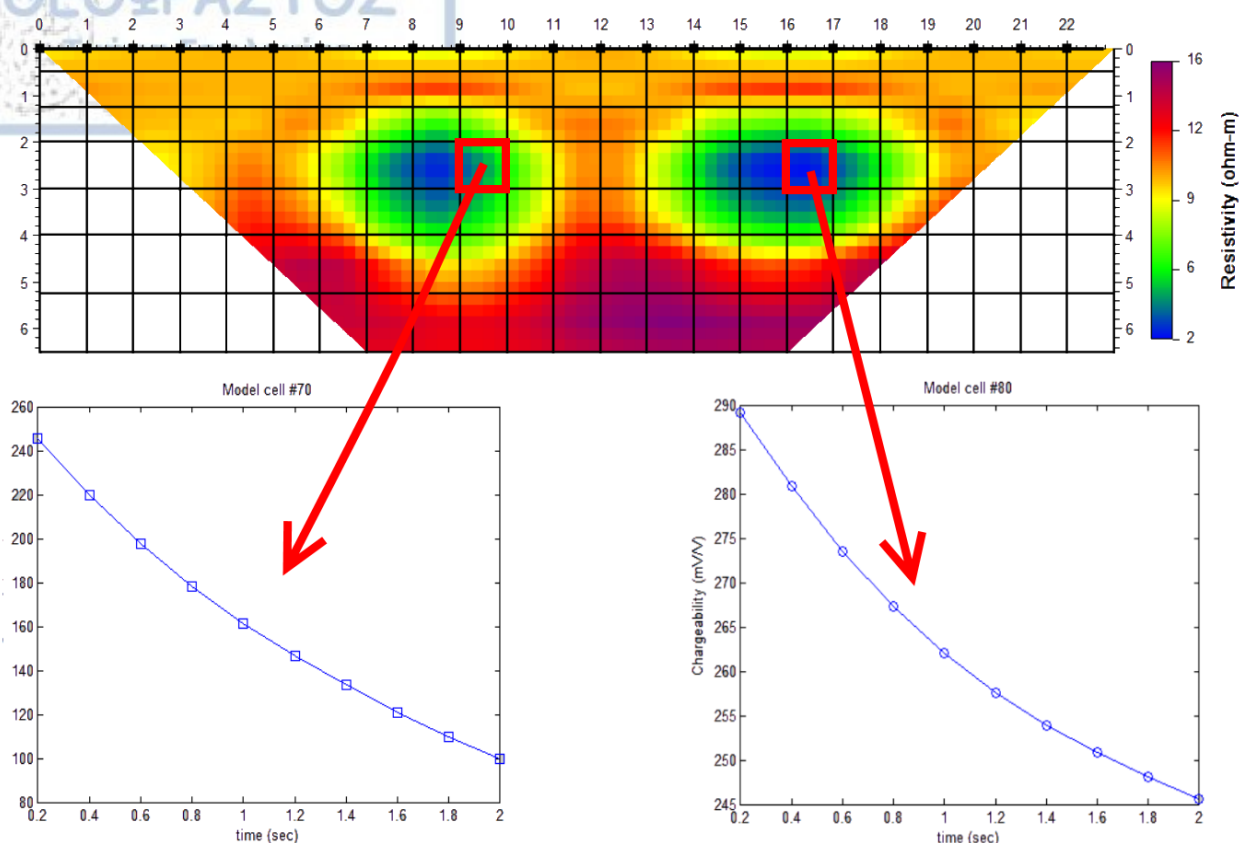


Figure 3. 13. Extraction of intrinsic chargeability curves. Resistivity image (top and) chargeability values of model cell #70 and #78 (bottom).

3.3 An optimization tool for Calculating of the Cole – Cole Parameters

3.3.1 Introduction

Following the calculation of the intrinsic TD chargeability of the model, using the software described above, the calculation of the Cole-Cole parameters can now be considered. Within the framework of this work an optimization tool for calculating the Cole-Cole parameters the basic of the inverted TDIP data was developed.

For that purpose a scheme (in Matlab) which solves the particular optimization problem using the Particle Swarm Optimization Algorithm was developed. The tool aims into finding the Cole-Cole model values (n_0 , τ , c) that best describe the curve's intrinsic chargeability decay over time. Considering the fact that the Cole-Cole model has 3 different unknown parameters at least 3 different time windows should be used

in the Spectral IP inversion in order to be able to uniquely determine the parameters, however a number of more channels (i.e. at least 6) is recommended for more reliable results, especially in situations where there is a significant amount of noise in the data.

Similar work has been presented previously (Yuval and Oldenburg, 1997) but the IP data of each IP window were inverted independently, however in this work the use of the simultaneous inversion of TDIP data is believed that will improve the quality of the results and the accuracy of the retrieved Cole-Cole parameters, especially in situations where the data quality is limited.

Although the Particle Swarm Optimization, as a global optimization technique, can be rather slow compared to direct optimization algorithms, it is chosen in this work because it is proven to be very robust, as it is not easily trapped into local minima and generally produces solution which are relatively insensitive to the initial model choice (Kennedy and Eberhart, 1995)

Initial tests (not shown here) that we conducted with the direct optimization methods, namely the Gauss-Newton algorithm, using the perturbation technique to approximate Jacobian (ignoring Hessian matrix) proved fast but rather unstable in situations where the initial guess was not very close to the final solution. Therefore, the extra time required using the global optimization techniques such as Particle Swarm Optimization method proved worthwhile.

3.3.2 Particle Swarm Optimization

The idea behind the Particle Swarm Optimization method is rather simple and has its roots into the social behavior science. It was used by scientists (Reynolds, 1987; Heppner and Grenander, 1990) to present simulation of bird flocking by trying to

understand the rules that apply to their synchronously movement which involves with frequently direction changes, scattering and regrouping.

The same rules apply to other large animal communities, regarding their movement in the search for food like fish of schools (Wilson, 1975). According to his research, in large communities the individual members of a community such as birds and fish, can benefit from the discoveries and previous experiences of all the other members of the community during their search for food. If the food supply considered unpredictable distributed the advantages overcome the disadvantage of competition.

This pattern of social behavior established the core of the Particle Swarm Optimization algorithm. The above idea could be described in a more mathematical way of thinking as a search in the 3D space of a point where the best solution is located. The swarms could be described as points that could take any value inside the boundaries of that space and they have the ability to “fly” around in the space searching for the best solution.

To begin with, a random initial solution is set for each particle and a random velocity vector is set for each particle as well. To avoid situations where the velocity of the particles is enormously increased an upper and lower limit is set in the velocity of each component. It is important not to set the same limit for every component because the space dimension could vary in each direction and the convergence would be very slow in this case.

The starting, inertia velocity, of each particle is used to shake the particles during the first steps, however after several steps, it will affect the behavior of the particles less. For this reason a damping factor is introduced to reduce the inertia velocity on each step i.e. as the swarm approaches into the solution.

Each particle stores its personal best position found. The best solution is the one which minimizes the objective function, which for that particular problem is the one that produces Cole-Cole model curves that best fits our inverted TDIP curves of a particular model cell.

At every iteration each particle moves a certain amount according to a velocity vector. Apart from the inertia velocity, each particle has its own personal velocity, pulling the particle towards their personal best and a swarm's velocity pulling the particle towards the group's best solution found so far as described in equation 3.3.

$$V = v_I + c_1 * v_p + c_2 * v_s \quad (3.3)$$

Where V is the velocity of the particle, v_i is the inertia velocity of the particle, v_p is the personal velocity of the particle and v_s is the swarm velocity. Coefficients c_1 and c_2 are set to 2 and are multiplied by a random value between the boundaries of the space domain in every run to differentiate velocity and allow bigger or smaller steps in space domain.

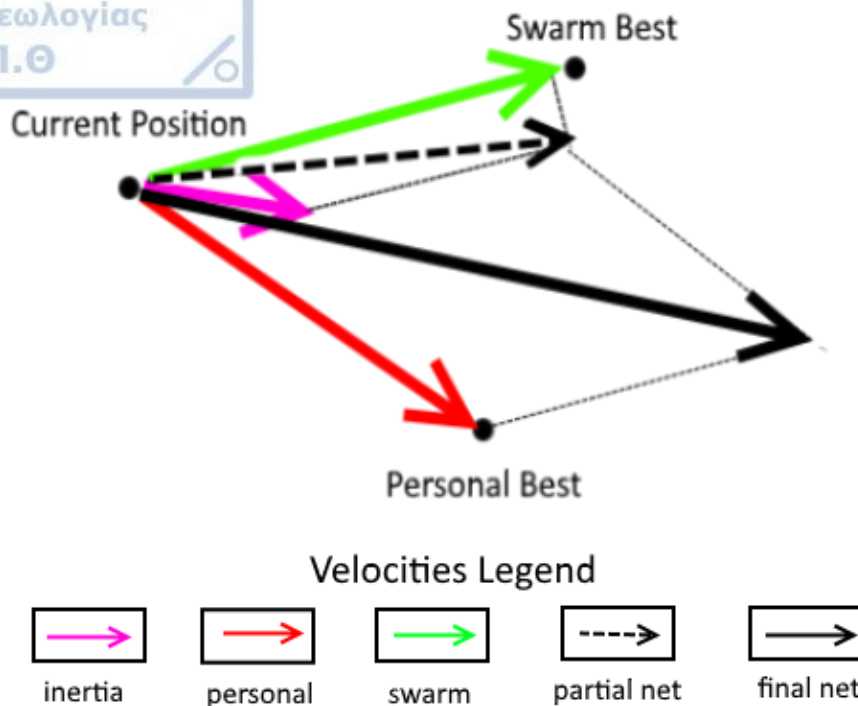
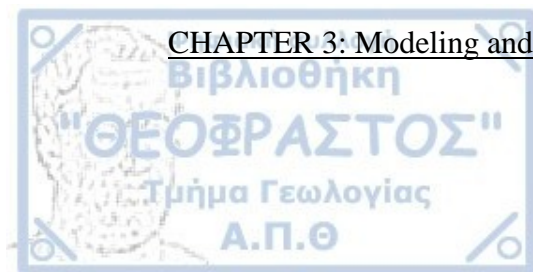


Figure 3. 14. Velocity vectors used in Particle Swarm.

3.3.3 Algorithmic Development

The general algorithm that was described in the previous section was applied within the framework of the particular problem. Among the different Particle Swarm Optimization schemes that exist in literature we have chosen the most commonly used approach of the initial, personal and best speed adopted.

The 3D space in our problem is not the x, y and z coordinate system but the chargeability, τ and c space (Table 3. 3). However, it should be noted that the same algorithm can be applied for any dimension space with minor modifications. Furthermore, the size of population and the maximum number of times that the population will move iterative is defined by the user along with the minimum and maximum allowed solution for the parameters. A starting population of 200 particles was chosen, and the number of iterations was set to 40 (each particles “fly” around 40 times).

Boundaries of the 3D space used

	Minimum	Maximum
Chargeability	0	1
Relaxation Time	0	100
Frequency Dependence	0	1

Table 3. 3. Boundaries of the 3D space used in Particle Swarm Optimization in this work.

Rather than using the existing Matlab tool, the code was developed analytically in order to allow full control of all algorithmic parameters (Figure 3. 15). The code was not developed from scratch but it was based on the work of Dr. Mostapha Kalami Heris. The Matlab code is presented in Appendix I.

```

measuredData = data;
costFunction = @(x,time) PeltonCurvesForward(x,time); % Cost Function

nVar = 3; % Number of Unknown (Decision) Variables
nData = length(measuredData); % Number of Data Points
varSize = [1 nVar]; % Matrix Size of Decision Variables

varMin = [0 0 0]; % Lower Bound
varMax = [1 100 1]; % Upper Bound

% Parameters of PSO

MaxIt = 20; % Maximum Number of Iterations [20] opt

nPop = 100; % Population Size (Swarm Size) [100] opt

w = 1; % Inertia Coefficient
wdamp = 0.5; % Damping Ratio of Inertia Coefficient
c1 = 2; % Personal Acceleration Coefficient
c2 = 2; % Social Acceleration Coefficient

```

Figure 3. 15. Setup options of Particle Swarm Optimization algorithm developed in matlab.

The algorithm reads the file which contains the inversion results as produced by DC2DPRO. In particular, the file contains the x, z coordinates of the center of each model cell, the resistivity and the inverted time domain chargeability values for every

time window. This file is the only input necessary in order to calculate the Cole-Cole parameters of the model. An example of such a file is shown in Figure 3. 16

xCenter	yCenter	Resistivity	log(Resistivity)	Ch1	Ch2	Ch3	Ch4	Ch5	Ch6	Ch7	Ch8	Ch9	Ch10
0.500	1.750	9.668622e+000	9.853646e-001	4.2	4.0	3.8	3.6	3.5	3.3	3.2	3.0	2.9	2.8
1.500	1.750	9.851025e+000	9.934814e-001	4.4	4.3	4.3	4.2	4.2	4.1	4.0	4.0	3.9	3.9
2.500	1.750	9.941248e+000	9.974409e-001	4.3	4.3	4.4	4.4	4.4	4.4	4.4	4.4	4.4	4.4
3.500	1.750	9.976332e+000	9.989709e-001	4.9	4.9	5.0	5.0	5.0	5.0	5.0	5.0	5.1	5.1
4.500	1.750	9.999924e+000	9.999967e-001	4.8	4.8	4.8	4.8	4.9	4.9	4.9	4.9	4.9	4.9
5.500	1.750	9.949028e+000	9.977807e-001	5.1	5.0	5.0	4.9	4.9	4.8	4.8	4.7	4.7	4.6
6.500	1.750	9.707170e+000	9.870927e-001	7.3	7.1	7.0	6.8	6.7	6.5	6.4	6.2	6.1	5.9
7.500	1.750	9.366302e+000	9.715681e-001	11.3	10.9	10.6	10.3	10.0	9.8	9.6	9.3	9.1	8.9
8.500	1.750	9.209256e+000	9.642246e-001	12.9	12.5	12.1	11.7	11.4	11.1	10.9	10.6	10.4	10.1
9.500	1.750	9.391025e+000	9.727130e-001	9.2	8.9	8.6	8.3	8.0	7.7	7.4	7.2	6.9	6.7

Figure 3. 16. Particle Swarm Optimization input file.

The program reads the spectral information and forms the chargeability decay curve for each model cell. The algorithm will perform the particle swarm optimization routine sequentially for every model cell and will produce the Cole-Cole parameters (n_o , τ , c) for every intrinsic decay curve until every block is processed (Figure 3. 17).

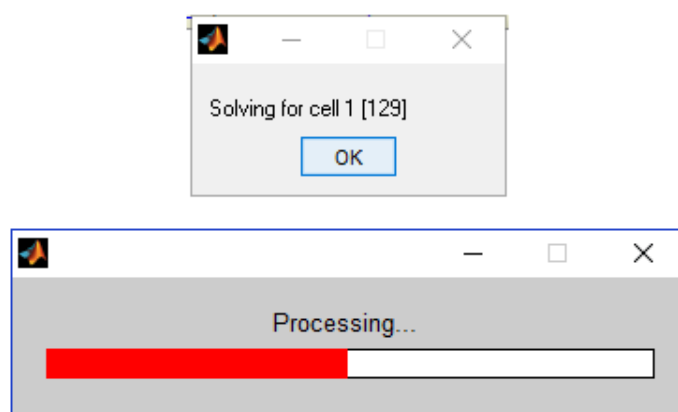


Figure 3. 17. Sample of the algorithm execution.

When processing is completed the algorithm saves the resulting Cole-Cole parameters data in a txt file.

As in many cases the intrinsic chargeability decay curve can be practically zero as the particular block is not chargeable a chargeability signal threshold option was

introduced to save unnecessary processing time: the optimization is taking place only for model blocks which have an average chargeability value larger than the threshold set.

The algorithmic process is described in the two flow charts presented below. The process of the main function is described in the Figure 3. 18 while in Figure 3. 19 the flow chart for the Particle Swarm Optimization used for the Cole-Cole parameters retrieval is presented.

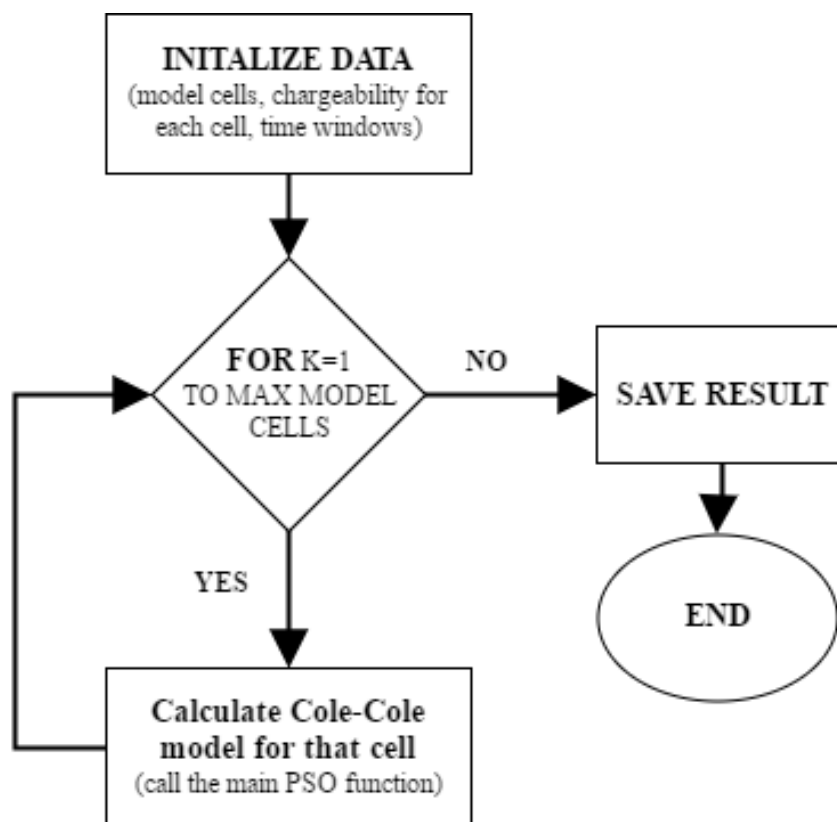


Figure 3. 18. Flowchart of the main function used for the calculation of the Cole-Cole parameters.

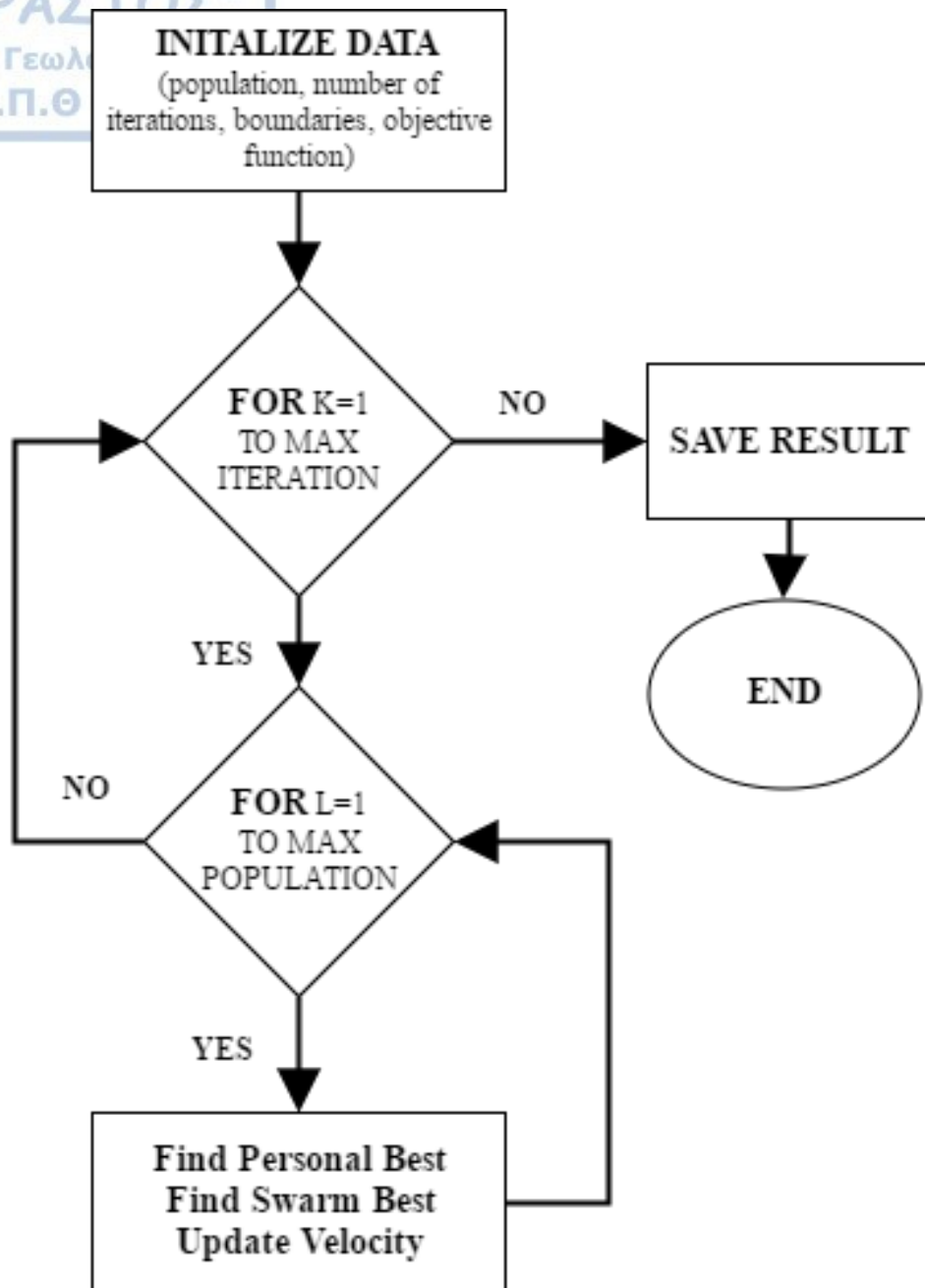


Figure 3. 19. Flowchart for the detailed Particle Swarm Optimization algorithm that was developed.

To illustrate the application of the algorithm a simple example is presented. Synthetic data for 20 time windows (100ms to 2 sec) were produced using the Cole-Cole TDIP response described in eq. 2.7 and then they were contaminated with 10% random noise.

The Particle Swarm Optimization algorithm was applied and the results can be seen below. The initial values and retrieved Cole-Cole parameters can be summarized

in the Table 3. 4. The initial, noise contaminated and retrieved decay curves are shown in the Figure 3. 20 and the Figure 3. 21. There is a good agreement of the final models with the initial ones despite the noise level.

Test Sample 1

	no	τ	c
Model Values	0.40	2	0.20
Retrieved Values	0.39	2.4	0.19

Test Sample 2

	no	τ	c
Model Values	0.60	10	0.20
Retrieved Values	0.63	8.4	0.14

Table 3. 4. Model and Retrieved values for test sample 1 and 2.

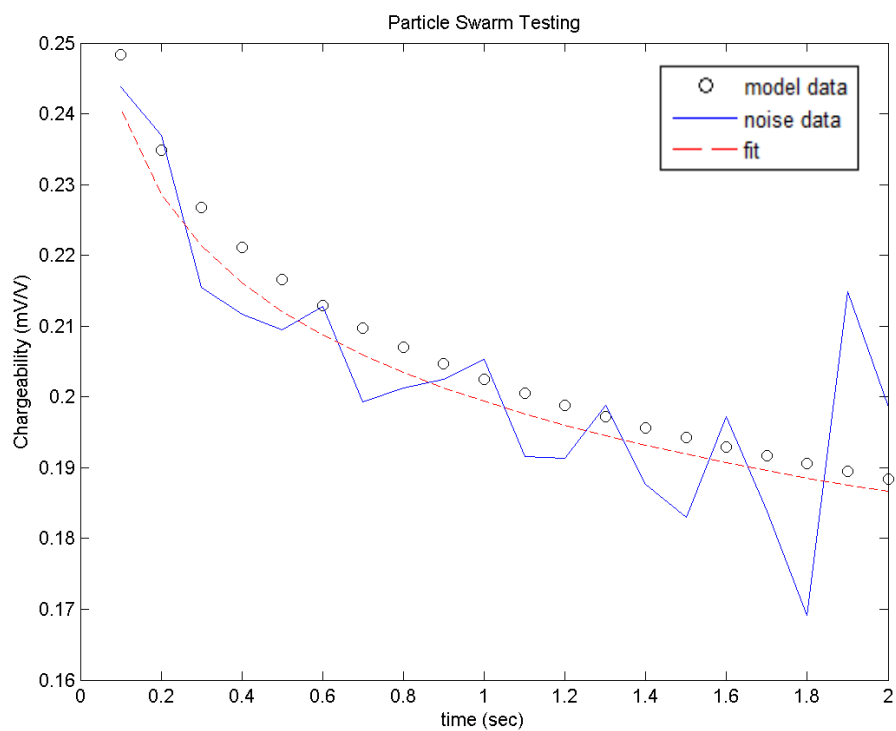


Figure 3. 20. Particle Swarm Optimization results for Test Sample 1.

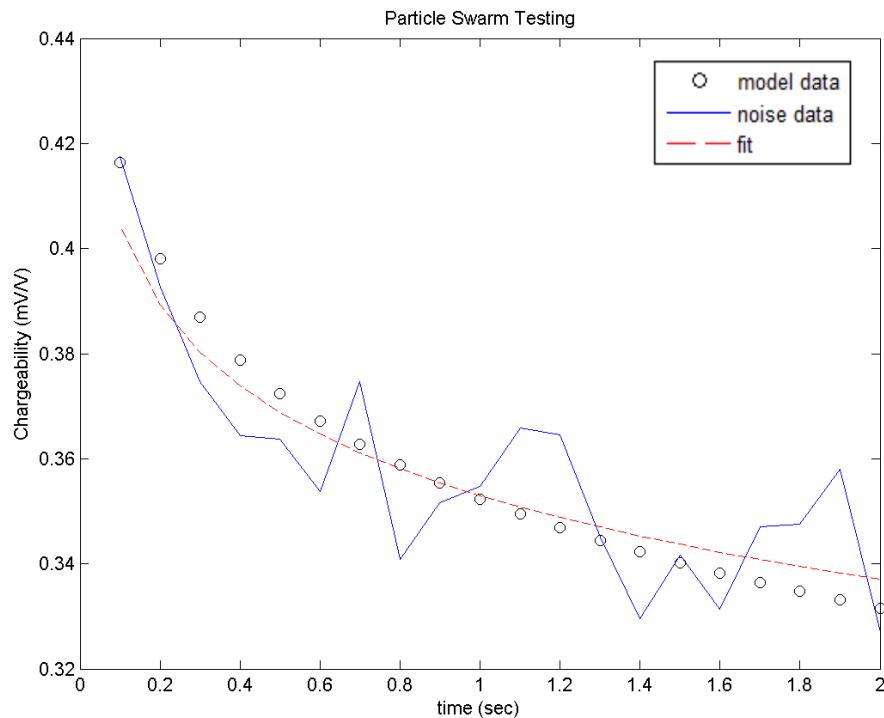


Figure 3. 21. Particle Swarm Optimization results for Test Sample 2.

Further, in Figure 3. 13 we illustrate the performance of the algorithm for the case of two blocks of the synthetic model presented in Figure 3. 13. As the decay curves are very smooth the algorithm achieves a good curve fitting.

A more detailed evaluation of the algorithm with synthetic and real data is presented in the following chapters.

Particle Swarm Optimization Results from Model Blocks

	no	τ	c
block #70	0.276	1.9	0.95
block #78	0.316	35.8	0.49

Table 3. 5. Particle Swarm Optimization results for the synthetic model presented in this chapter.

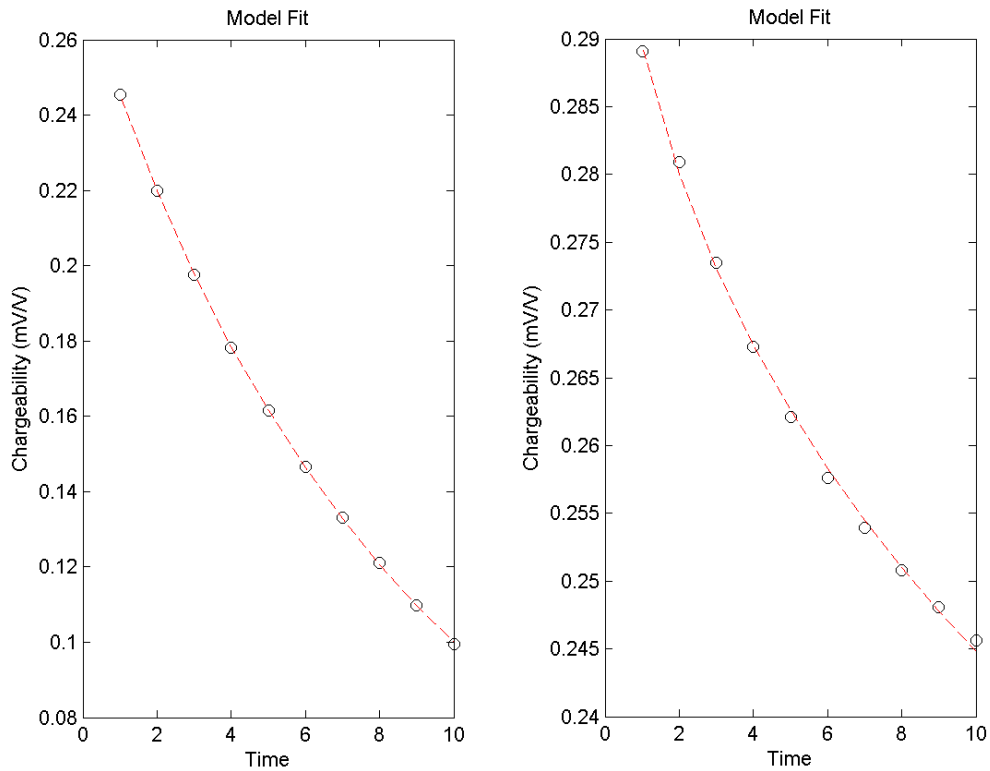
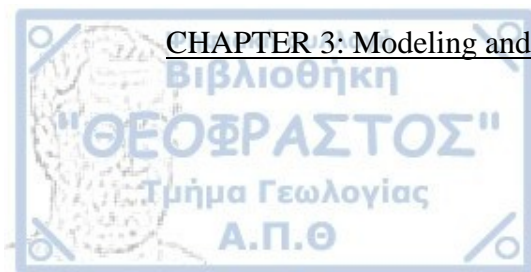
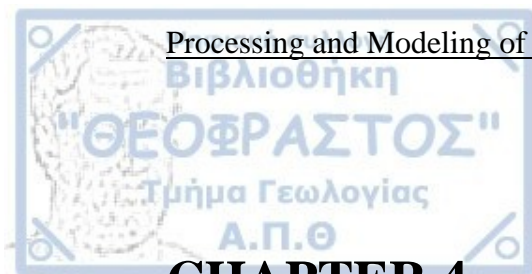


Figure 3. 22. Model block 70 (left) and 78 (right).





CHAPTER 4

Application to Synthetic Time Domain IP Data

In this chapter the results of the synthetic TDIP modeling that was produced and processed as previously described will be discussed.

For the presentation of the results for each model, a pattern similar to the one described previously will be followed. First, the information about model geometry and then the information about the electrical properties of the prisms that was used will be described. At this point the pseudo sections produced by the forward solver will be given, and following that the results of the inversion will be thoroughly discussed. Finally, the inversion results are used to calculate the Cole-Cole parameters of the model.

The first two models consist of prisms with contrast in the electrical properties with the background. The third model was created to study the 3D effect on the 2D TDIP inversion in the case of a single prism. The prism strike (Y axis) boundaries were sequentially reduced in order to study the effect of the changing 3rd dimension.

4.1 Introduction

In this chapter the inversion results and the calculated Cole-Cole parameters are presented for synthetic 3D models in order to evaluate the procedure presented in the previous chapter. As explained, the inversion program used in this work operates only in two dimensions (2D) so the produced full 3D synthetic data-sets cannot be used directly for the inversion. Instead, a 2D data-set is extracted from 3D data-set in order to be further processed by the inversion software. Regardless the fact that the inversion is done in 2D, since the forward modeling is solved in a 3D geometry it provides the opportunity to process true 3D data. So a special synthetic model was designed to study the 3D effect in the 2D TDIP inversion procedure

In the following the results of three synthetic models are presented. The first 2 are 3D prisms models while the third synthetic model is used to study the 3D effects on 2D TDIP inversion. All data presented in this section are extracted 2D lines measured with the dipole-dipole array.

4.2 Model 1

The first model involves the simulation of the TDIP response of two 3D chargeable prisms. The size of the modeling domain is 24 X 5 meters and it includes 2 conductive polarizable prisms which can be seen in the cross-section at the x-z plain of Figure 4. 1 together with the resistivity and Cole-Cole properties of all modeling bodies. The full 3D visualization of the model is presented in Figure 4. 2. The exact properties of the modeling bodies are given in Table 4. 1.

<i>Modeling body</i>	<i>Resistivity Ohm-m</i>	<i>Chargeability mV/V</i>	<i>τ</i>	<i>c</i>
Background	10	10	1	1.00
Prism 1 (left)	2	400	1	0.40
Prism 2 (right)	2	400	10	0.60

Table 4. 1. Values of the electrical properties used in the original Model 1.

It should be noted that there is no variation contrast in the τ value (relaxation time) of the first prism compared to the background and it was selected to test how this will affect its retrieval into the TDIP inversion.

The full 3D model response was calculated for 20 different time channels at 100msec intervals starting from 100msec up to 2sec. The dipole-dipole array data was simulated having an electrode separation $a=1\text{m}$ with the maximum dipole separation set to be $8a$ while for larger separations the dipole length was doubled (i.e. $2a$) until it reached again the $8(2a)$. As explained only the central 2D measured line was extracted from the full 3D data set to be inverted.

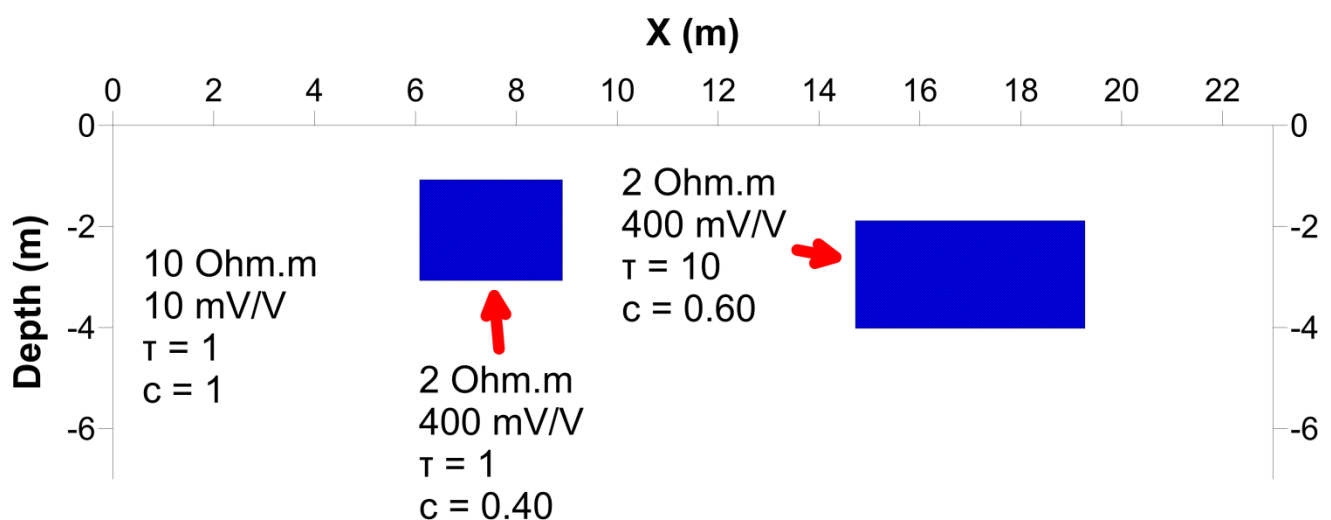


Figure 4. 1. X-Z plain of the middle slice for Model 1.

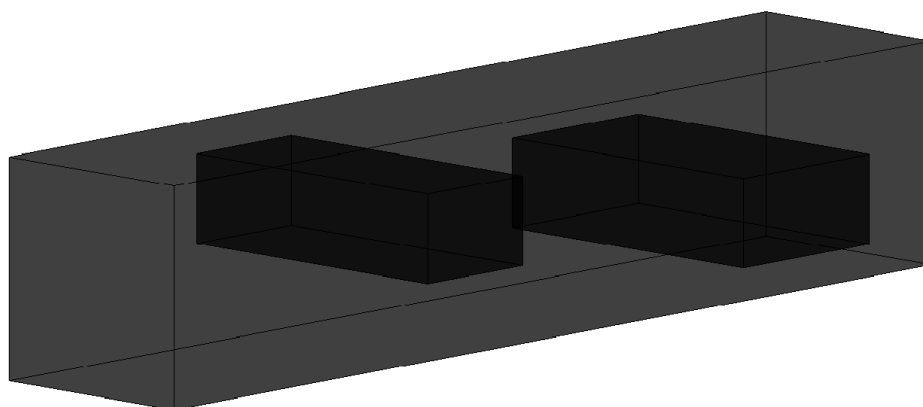


Figure 4. 2. 3D view of Original Model Geometry for Model 1.

The forward modeling dipole-dipole data in the form of pseudo sections are presented in Figure 4. 3. The anomalous bodies generate reverse V-shape anomalies typical for the dipole-dipole configuration. The apparent resistivity of the 1st prism is lower than the apparent resistivity of the 2nd one, even though they have the same electrical resistivity value. This is because the 1st prism is closer to the surface.

This can also be seen in the apparent chargeability pseudo sections. Even though the prisms have similar intrinsic chargeability values, because of the different depth that they are located, the apparent chargeability of the shallower prism is higher than the second one.

The TDIP data, produced by the forward solver were inverted in order to calculate the distribution of the actual electrical resistivity and chargeability.

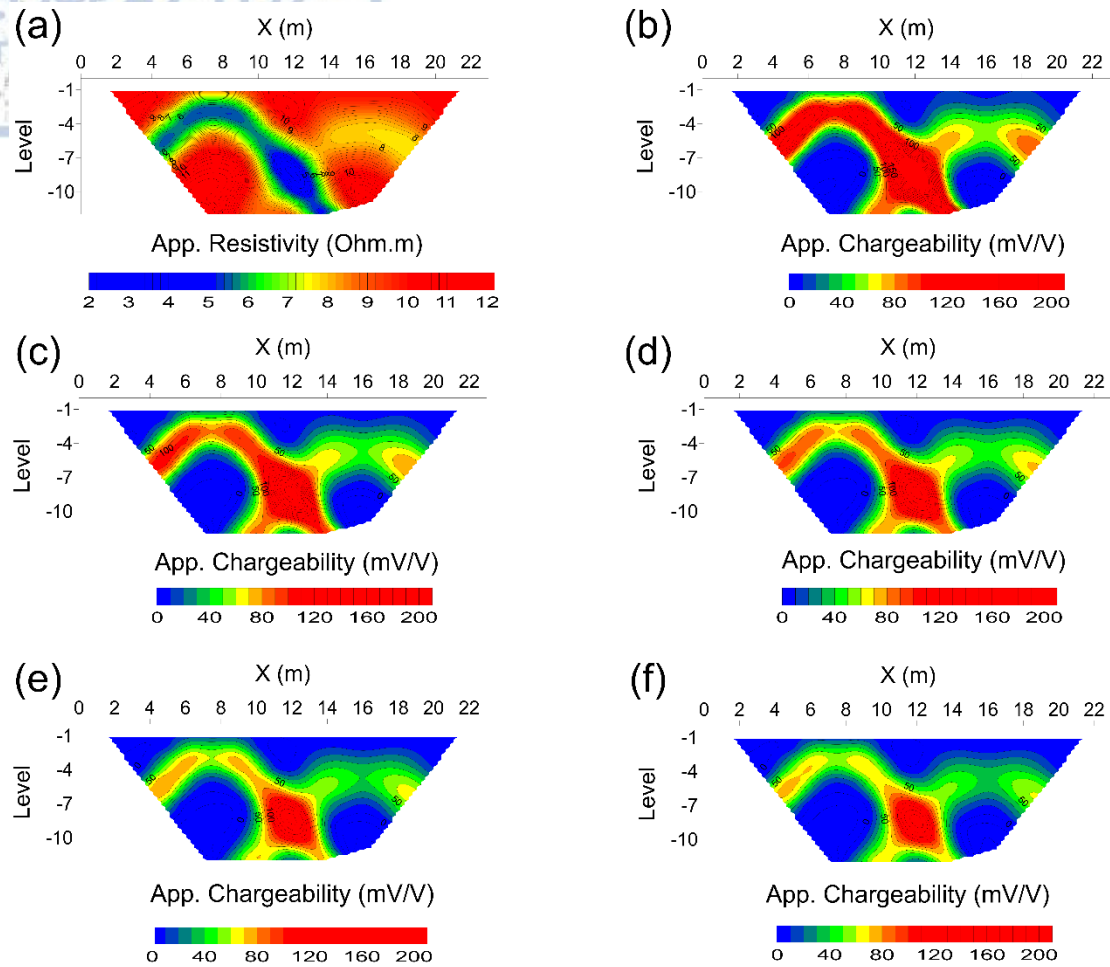


Figure 4. 3. Model 1 pseudo section of (a) apparent resistivity, (b) - (f) apparent chargeability of channel 1, 4, 7, 12, 15.

The inversion results for the resistivity can be seen in Figure 4. 4a while the chargeability inversion results for different time models can be seen in Figure 4. 4b-f.

The resistivity image very clearly shows the boundaries of the two modeling prisms. The inverted chargeability images also show the location of the prisms but the chargeability distribution is mostly concentrated at the upper half part of the modeling bodies. Overall, the lateral boundaries (across the X axis) and top boundary of the bodies are clearly seen but the lower boundary of the bodies is not clearly delineated.

Furthermore, as the second body is deeper than the first the resolution is reduced with the depth so its reconstructed image is of lower quality in relation to the shallower prism.

Another observation has to do with the fact that the chargeability images misplace slightly the target which seems concentrated mostly on its top boundary especially when the signal is low (e.g. 2nd prism), while the resistivity image can better resolve the boundaries of the modeling bodies.

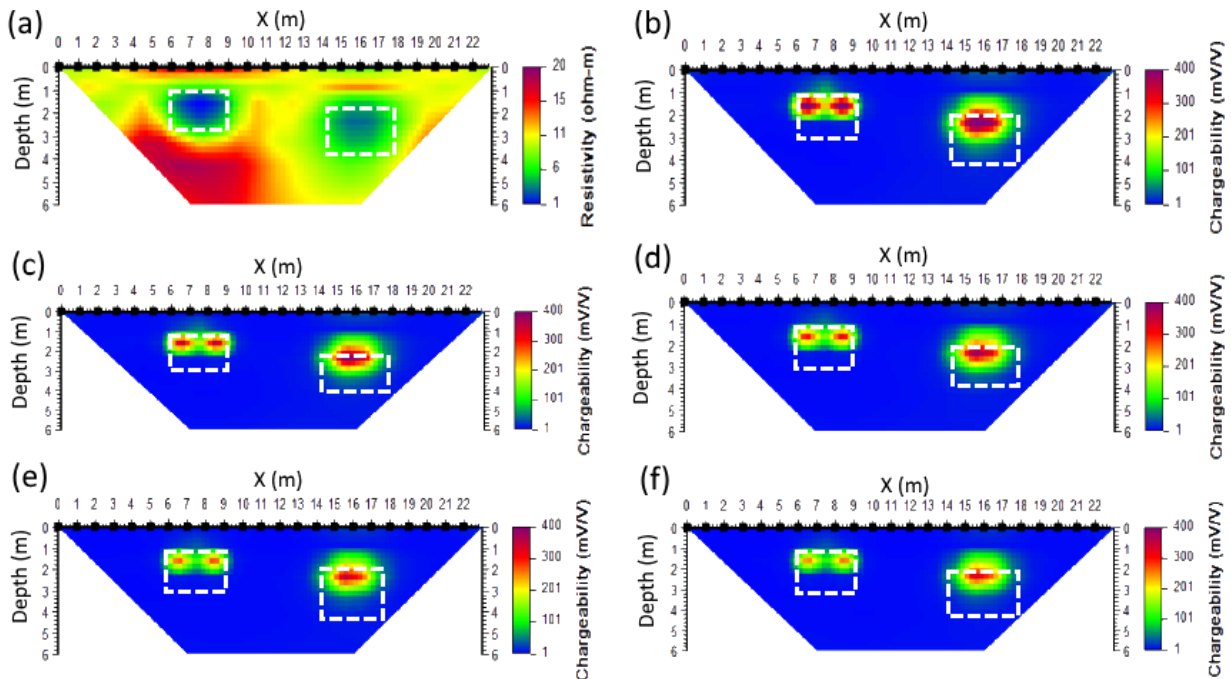


Figure 4. 4. TDIP inversion results for Model 1. (a) resistivity, (b) - (f) chargeability for channel 1, 4, 7, 12, 15.

A closer inspection of the different windows of the TDIP inversion results (Figure 4. 4) can also provide a qualitative hint about the behavior of the Cole-Cole parameters and especially τ . It is very clear that although the chargeability level of the two prisms are similar for the first window, the chargeability of the first body decays faster compared to the second body. This indicates that the value of τ for the first body is smaller than the value of τ for the second body which is of course in line with the original model parameters.

This can be further verified by looking at the inverted decay curves for particular a model block i.e. for the model blocks which correspond to the prisms

(Figure 4. 5): The chargeability of the model cells of the first body decays much faster that in the case of the second body.

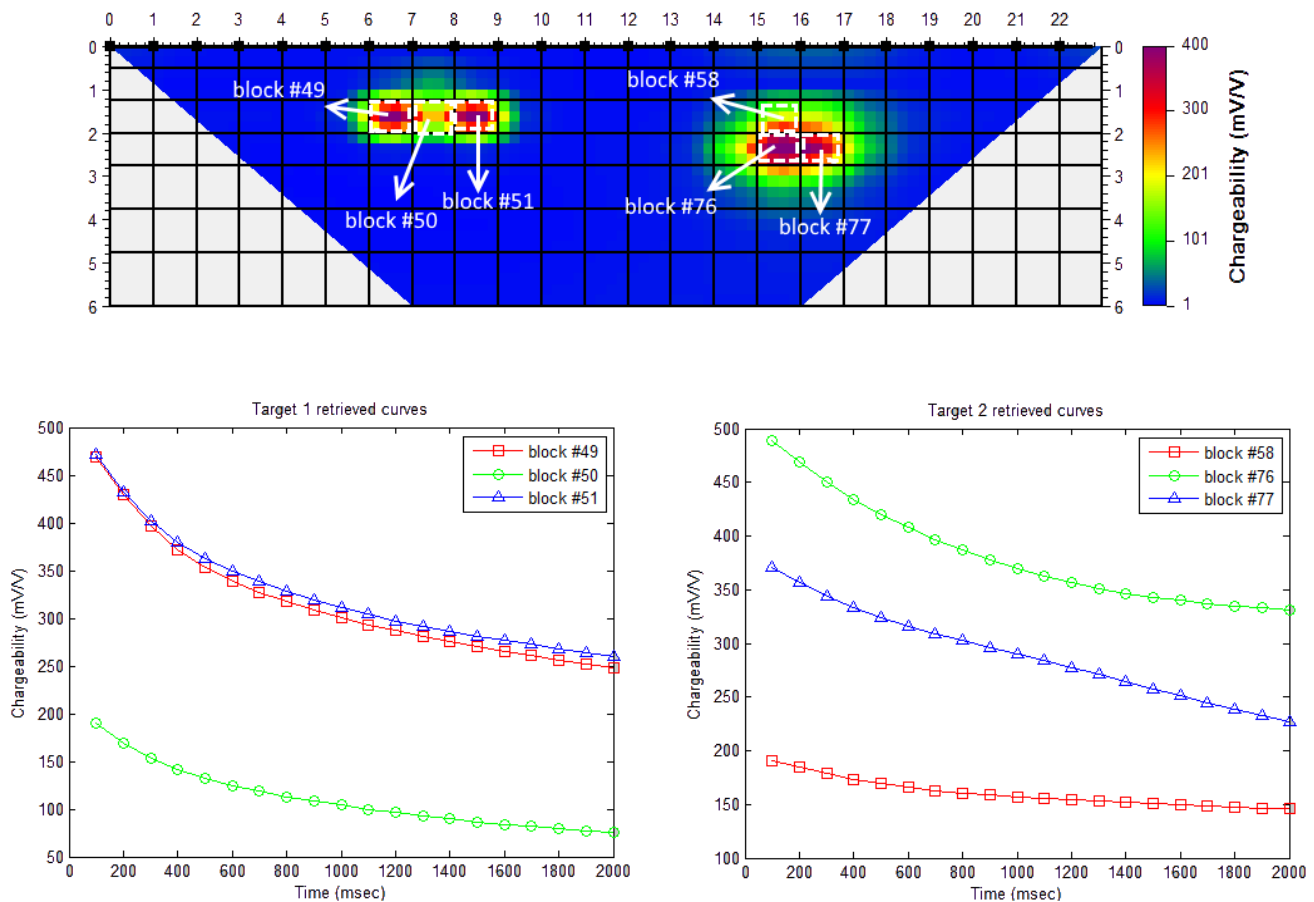


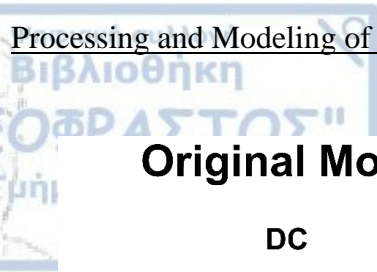
Figure 4. 5. Decay curves for intrinsic chargeability values for the first body (left) and the second body (right) of Model 1. The location of each model block can be seen in the top figure.

Finally, the Particle Swarm Optimization algorithm was used to calculate the Cole–Cole parameters (intrinsic chargeability, τ , c) for every model cell on the basis of the decay curves produced by the TDIP inversion. As in some model regions the chargeability signal is very low applying the Particle Swarm Optimization in these areas is time consuming and can result into unstable results. Therefore the algorithm was applied only to the cells where the inverted chargeability of the first channel is at least higher than 5 mV/V.

The retrieved results for the Cole-Cole parameters together with the inverted resistivity image are presented at the right column of Figure 4. 6 while at the left column of the same figure the original model used to produce the synthetic data is presented in order to evaluate the inversion results.

First of all, it is clear that any inversion artefact present at the inversion of the resistivity, such as the resistive region beneath the left prism, does not propagate at the Cole-Cole inversion results.

Even though the targets were at different depths, any inverted results that contain strong signal can be used in order to successfully calculate the Cole-Cole parameters. Generally the intrinsic chargeability, τ and c parameters are reconstructed in a satisfactory way although the inverted property seems to be concentrated at the top part of the modeling bodies. On the other hand, possible errors in the retrieval of the chargeability distribution are unavoidably reflected into the retrieval of the Cole-Cole parameters. Among the retrieved Cole-Cole parameters the c (frequency dependence) seems to be less satisfactorily retrieved which possibly suggests that its inversion is less stable.



Original Model

Inversion Results

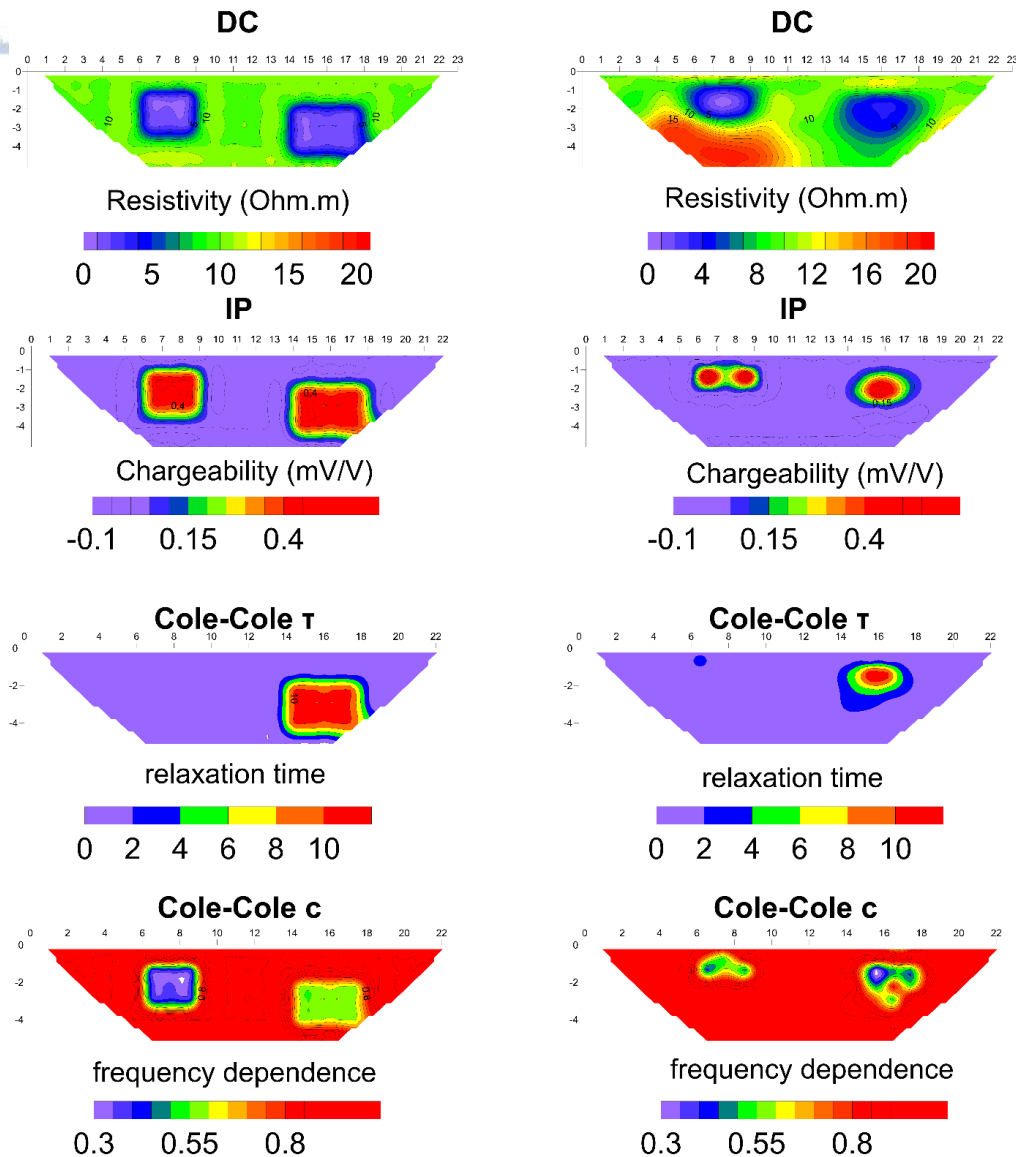


Figure 4. 6. TDIP final inversion results for Model 1.

4.3 Model 2

The second model used in this work involves the simulation of the IP response of seven 3D chargeable prisms which were overlaid to form a complex 3D body resembling two fractured zoned filled with conductive and chargeable materials. The same general domain geometry as in the previously model was used: 24X5m. The conductive polarizable modeling body can be seen in the cross-section at the X-Z plain

of Figure 4. 7 and its full 3D structure is presented in Figure 4. 8. The exact properties of the modeling bodies are given in Table 4. 2.

<i>Modeling body</i>	<i>Resistivity Ohm-m</i>	<i>Chargeability mV/V</i>	τ	c
Background	10	10	1	1.00
Model	2	400	10	0.80

Table 4. 2. Values of the electrical properties used in the original Model 2.

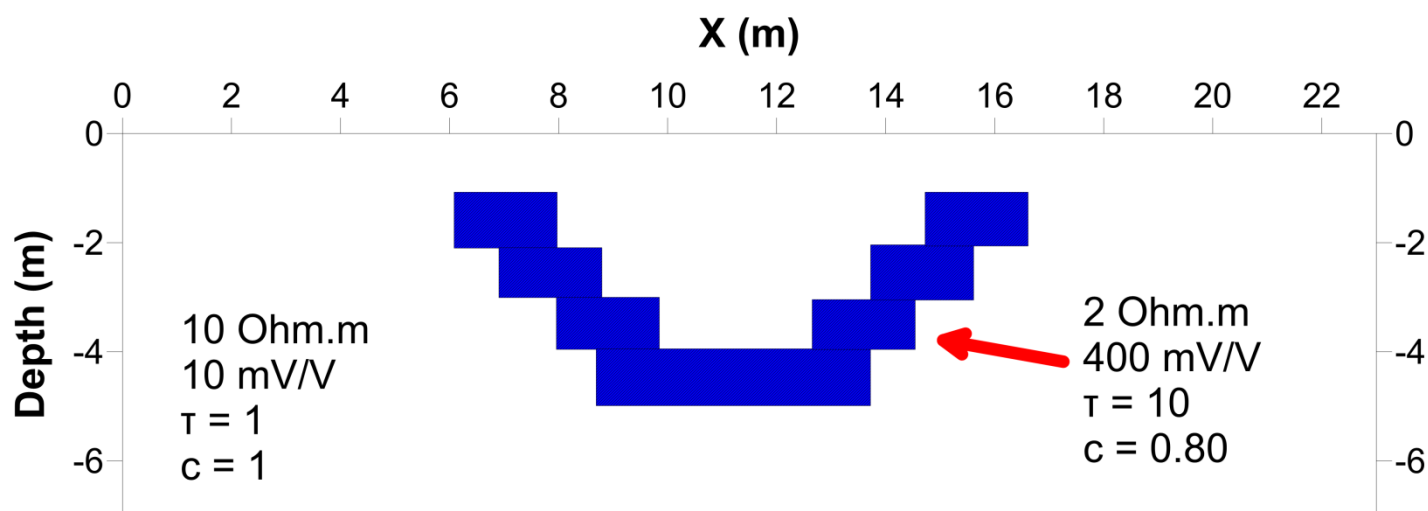


Figure 4. 7. X-Z plain of the middle slice for Model 2.

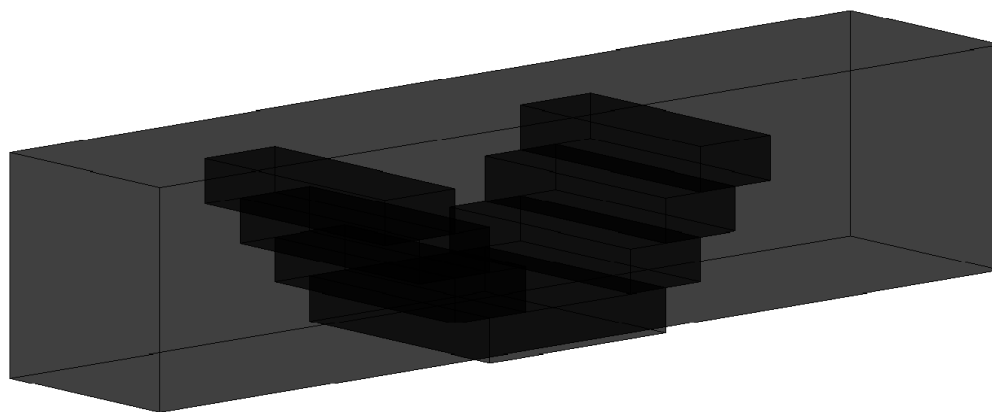


Figure 4. 8. 3D view of the original geometry of Model 2.

The array configuration used is the dipole-dipole array with 1m electrode separation. To calculate the model response 20 different channels were used starting from 100ms up to 2sec, with an interval of 100ms. For further data processing the

middle slice of the model was extracted from the 3D forward solution response in order to be inverted using the 2D algorithm described in the previous section.

The forward model pseudo sections are presented in Figure 4. 9. The reverse V-shape anomaly is present once again in the apparent resistivity pseudo sections, however this time the shape is symmetric due to the symmetry of the model's geometry. The apparent chargeability pseudo section has very similar behavior, with clear symmetric reverse V shape pattern.

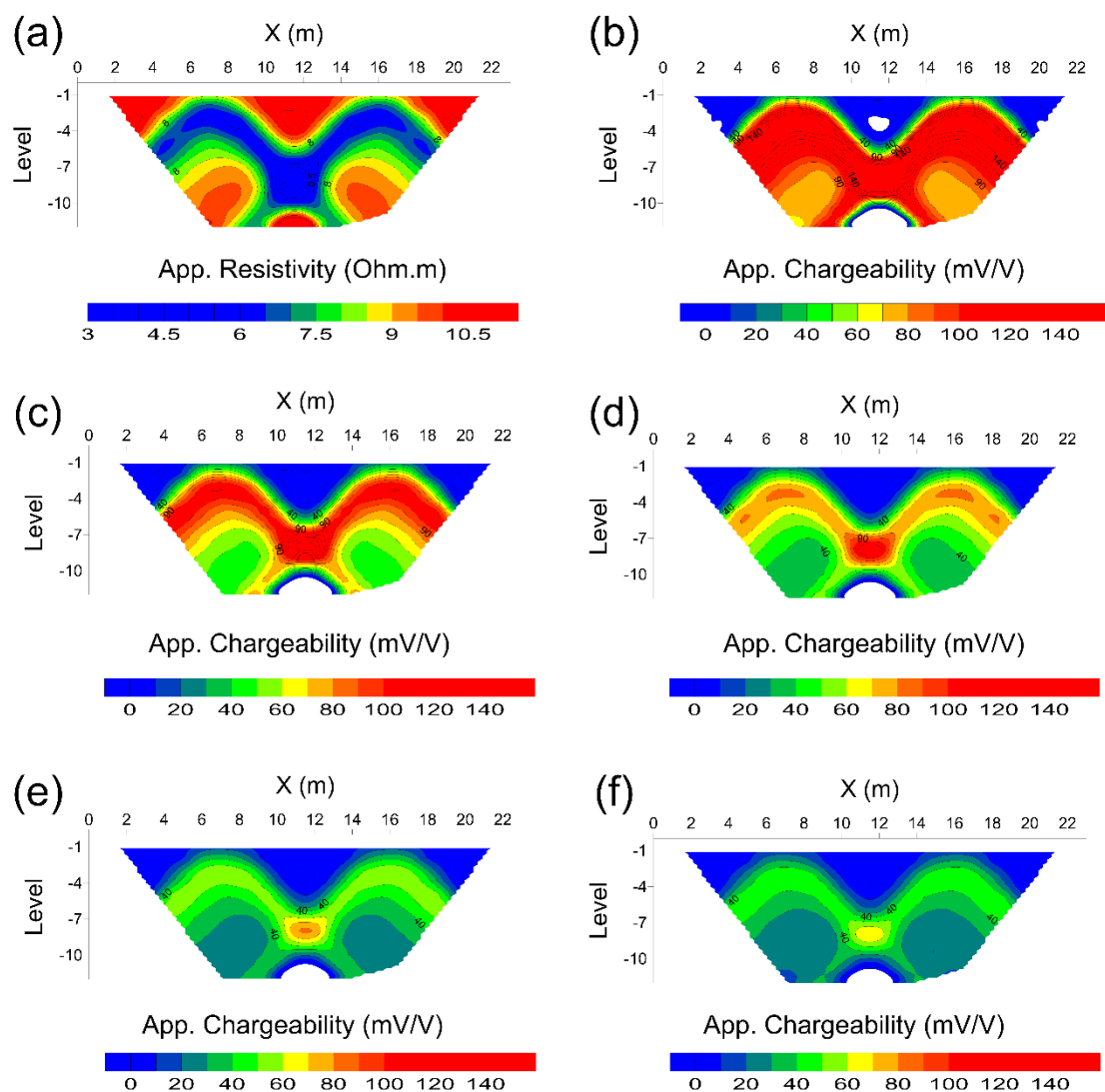


Figure 4. 9. Model 2 Pseudo section of (a) apparent resistivity, (b) - (f) apparent chargeability of channel 1, 4, 7, 12, 15.

The TDIP inversion results of the apparent resistivity and apparent chargeability data can be seen in Figure 4. 10. The resistivity image very clearly shows the boundaries of the modeling structure. The inverted chargeability images also show the location and the general outline of the body although this appears to be quite inhomogeneous suggesting that it has separate materials. This is probably caused by the inversion algorithm, and shows similarity with the case of model 1 where the chargeability distribution tends to move very close to the upper limit of the bodies.

Additionally, and in contrast to the resistivity image, the inverted chargeability images introduce a misplacement of the modeling body compared to its original position especially at larger depths. The relatively different resistivity and chargeability images in relation to the depth extend of the body could lead in to a dilemma regarding the final interpretation and is a reason for consideration.

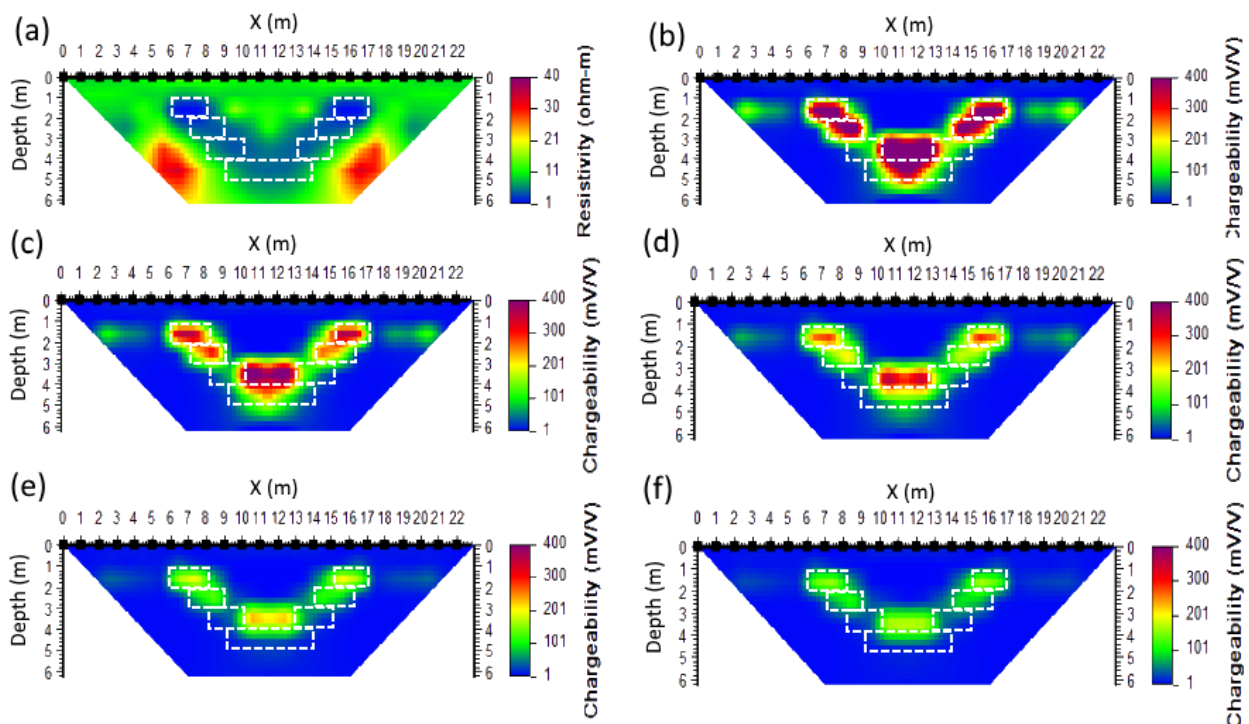


Figure 4. 10. TDIP inversion results for Model 2 (a) resistivity, (b) - (f) channel 1, 4, 7, 12, 15.

In the inverted chargeability images it can be seen that the chargeability signal drops rapidly over time and with very similar rate over the chargeable bodies which suggests that the material is uniform. This can be also seen by inspecting different intrinsic chargeability decay curves for specific model blocks shown in Figure 4. 11. Given the similar shape of the curves the frequency dependence should be similar as well.

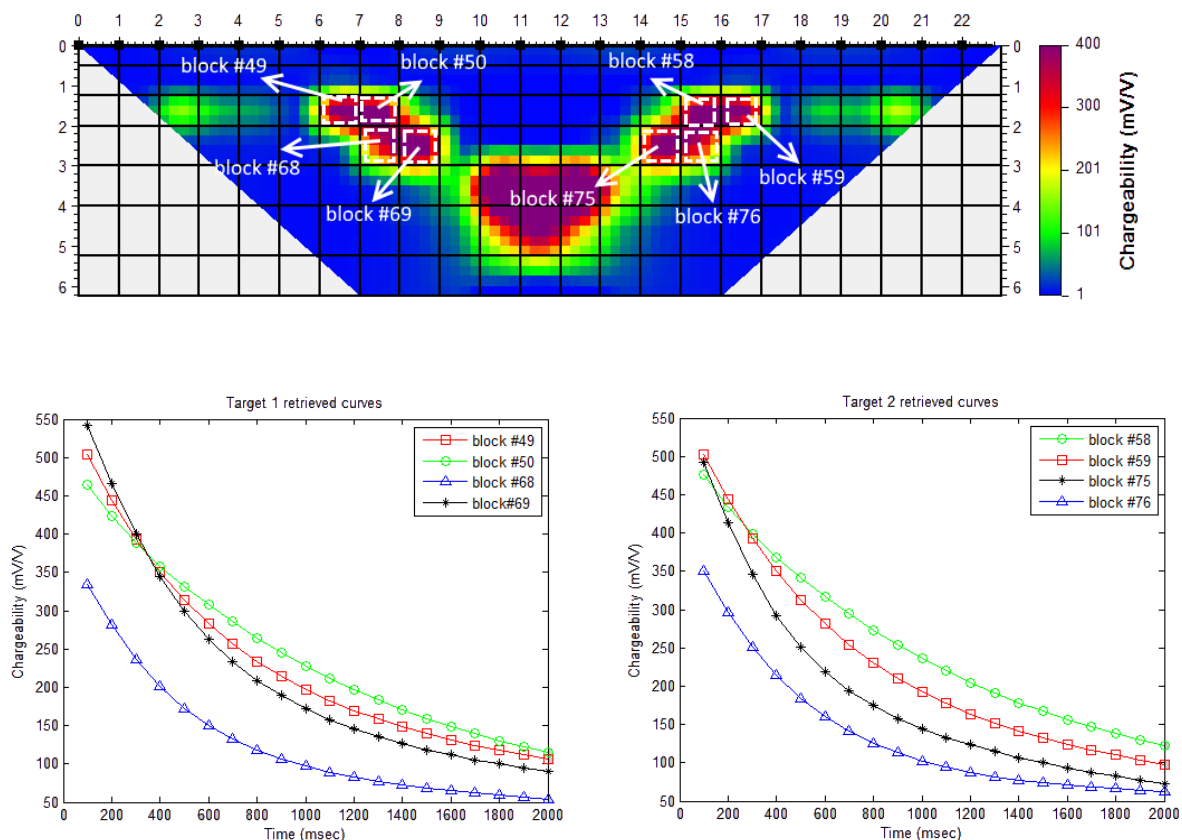


Figure 4. 11. Decay curves for intrinsic chargeability for the upper left prism (left) and the upper right prism (right) for Model 2. The location of the model blocks can be seen in top figure.

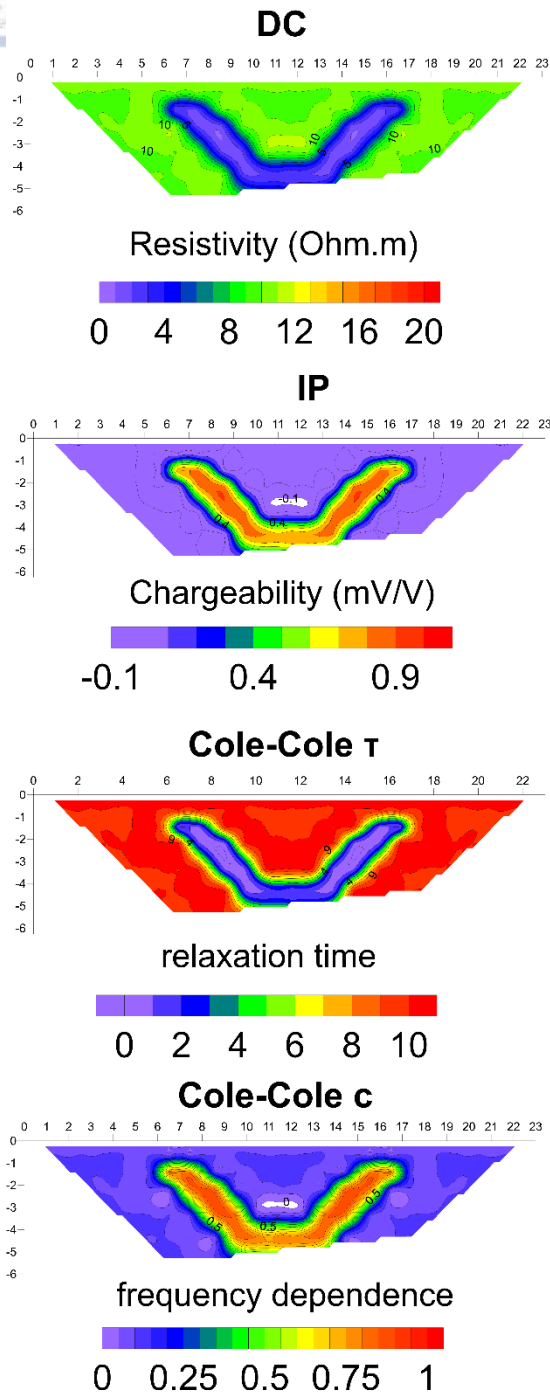
Consequently, the Particle Swarm Optimization algorithm was used to calculate the Cole–Cole parameters (intrinsic chargeability, τ , c) for every model cell on the basis of the decay curves produced by the TDIP inversion. The inverted resistivity image and the reconstructed Cole–Cole parameters are presented at the right column of Figure 4. 12 together with the original model at the left column of the figure.

Again the resistive anomaly beneath the conductive prism can be seen into the resistivity inversion image but this artefact does not appear into the Cole-Cole inversion results. We can assume therefore that the calculation of chargeability and Cole-Cole parameters can be safely made.

Once again in regions where the chargeability signal is too low the calculation of the Cole-Cole parameters using the Particle Swarm Optimization algorithm cannot yield reliable results as it proved unstable particularly for the c Cole-Cole parameter. For this reason the focused version of Particle Swarm Optimization was used in this case as it ignores such areas and calculates the parameters only for model blocks with sufficient signal.

The properties of the material calculated through the inversion and Particle Swarm Optimization are very close to the original models. The Cole-Cole parameters can yield a reliable result regarding different chargeable materials as it can be an indicator of the level of similarity between the materials of the targets.

Original Model



Inversion Results

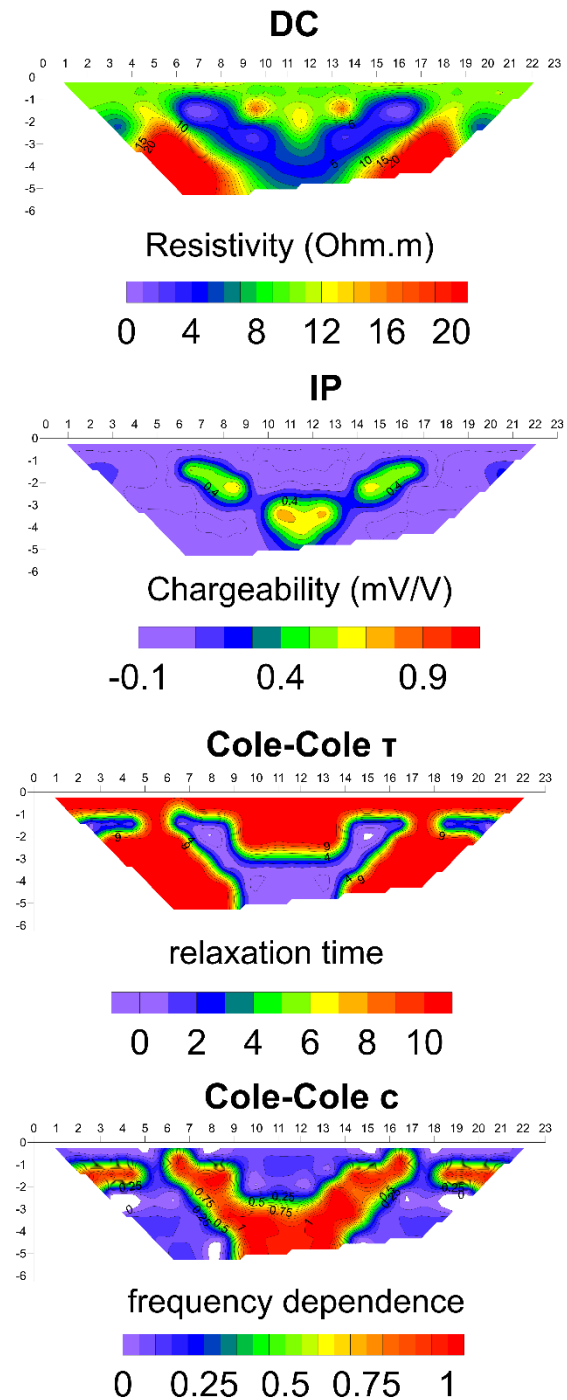


Figure 4. 12. TDIP final inversion results for Model 2.

4.4 3D effects on 2D inversion

In order to study the 3D effect in 2D TDIP inversion a prism model with changing dimensions along the strike (Y axis) was used. The overall model geometry involved a 24x24x7m domain. A chargeable conductive prism located at the central part of the domain having fixed boundaries along x-axis (electrode array) and z-axis (depth) was considered, however the boundaries across the Y-axis were differentiated.

For the first model the prism had a maximum length of 24m across the Y axis i.e. 12 electrode units to each side of the array (it is named Model 12a) which suggests that the model fits the assumptions of the “infinite” length at the strike direction required by the theoretical formulation of the 2D inversion algorithm. The strike length of the prism was gradually reduced to 16, 8 and 2m generating the Models 8a, 4a and 1a respectively simulating bodies which depart more and more from the 2D inversion assumptions.

The location and properties of the prism across the X-Z plain is shown in Figure 4. 13 and in Figure 4. 14 the X-Y profiles models used at depth of 2.5 meter are shown. The electrical properties of the prism remain the same in every model, and can be seen in Table 4. 3, so any differences into the inversion results should be due the different Y-axis length of the prisms.

<i>Modeling body</i>	<i>Resistivity Ohm-m</i>	<i>Chargeability mV/V</i>	<i>τ</i>	<i>c</i>
Background	10	10	1	1.00
Model	2	400	10	0.70

Table 4. 3. Values of the electrical properties of the original models used in the study of the 3D effect.

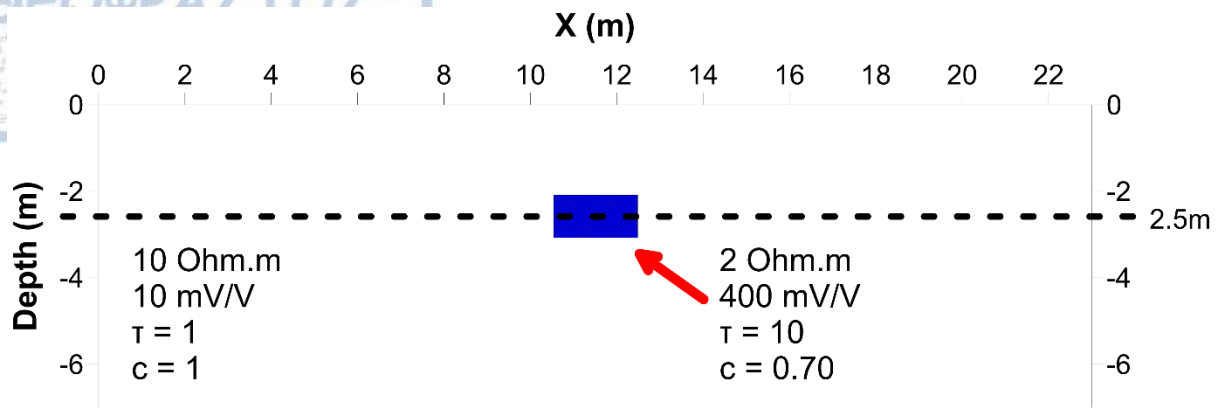


Figure 4.13. X-Z plain of the middle slice for all the Models used in the study of 3D effect.

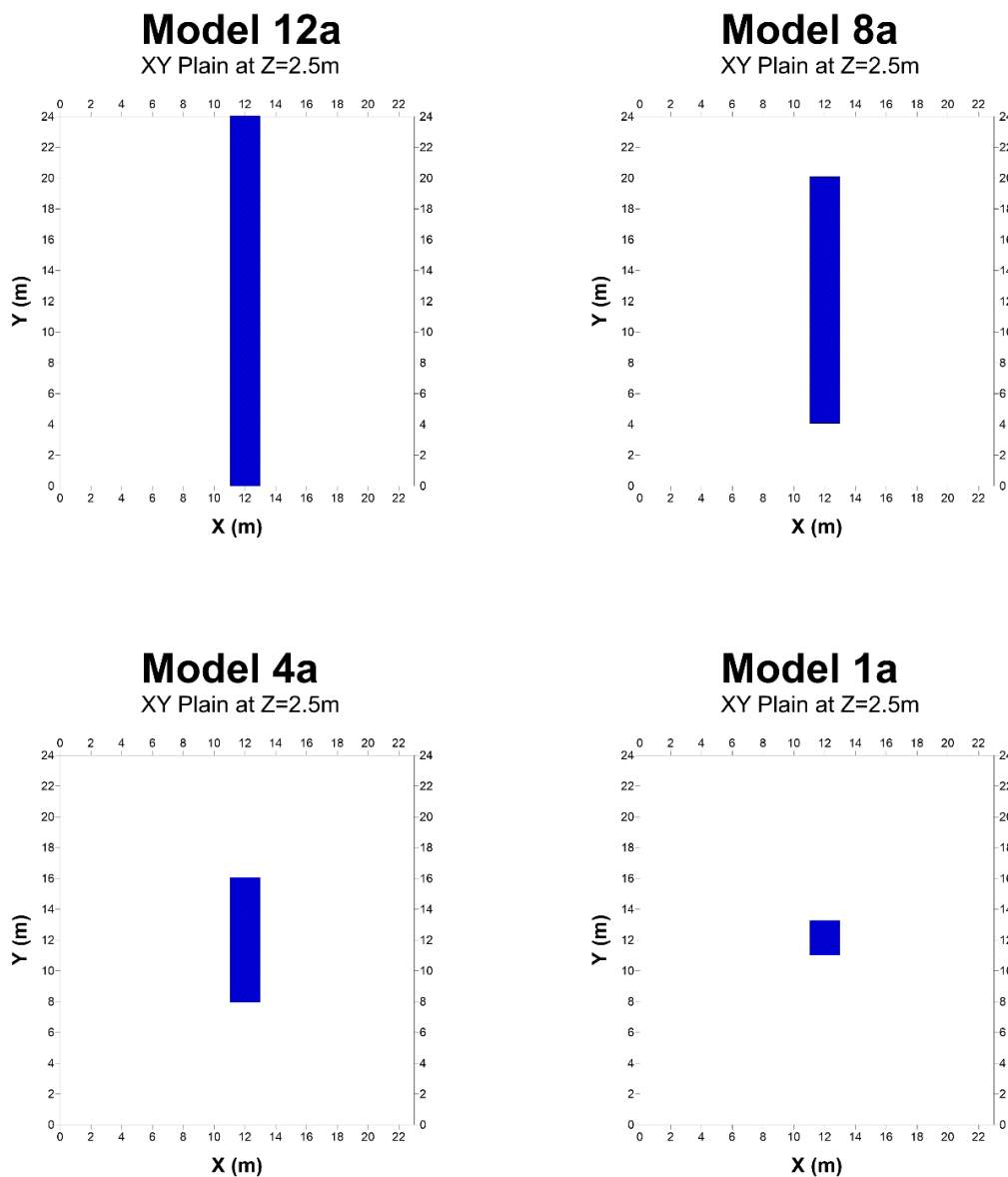
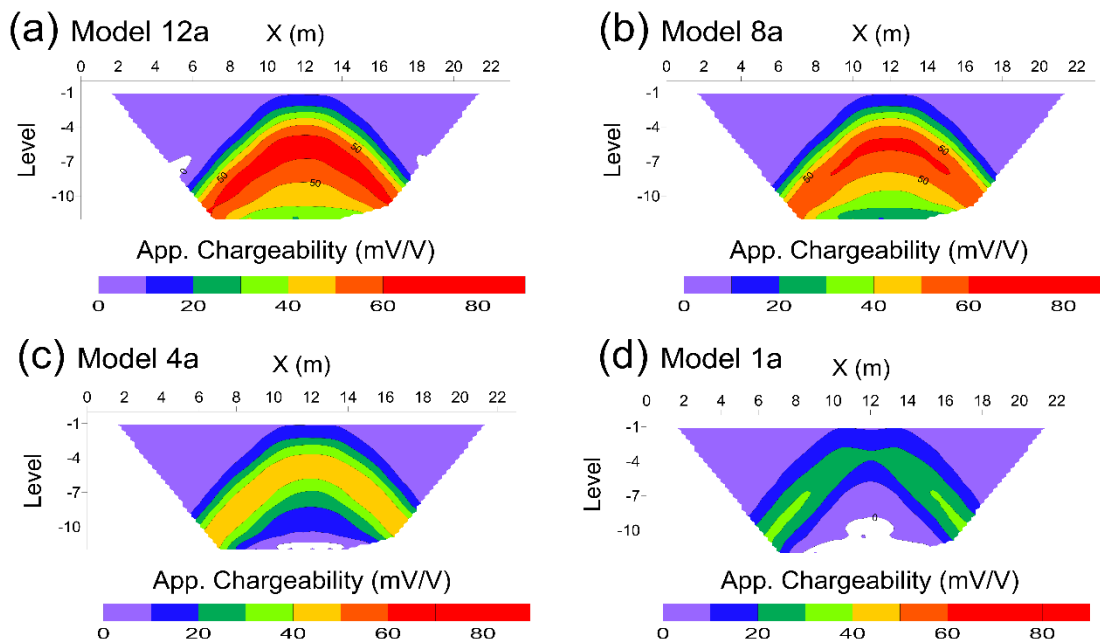


Figure 4.14. X-Y slices at 2.5m depth for Model 12a (a) to Model 1a (d) which used in study of the 3D effect.

The full 3D model response was calculated for 20 different 100msec step channels (from 100- 2000 msec). The dipole-dipole array data were simulated for every model and only the central 2D measured line was extracted from the full 3D data set to be inverted.

Channel 1



Channel 4

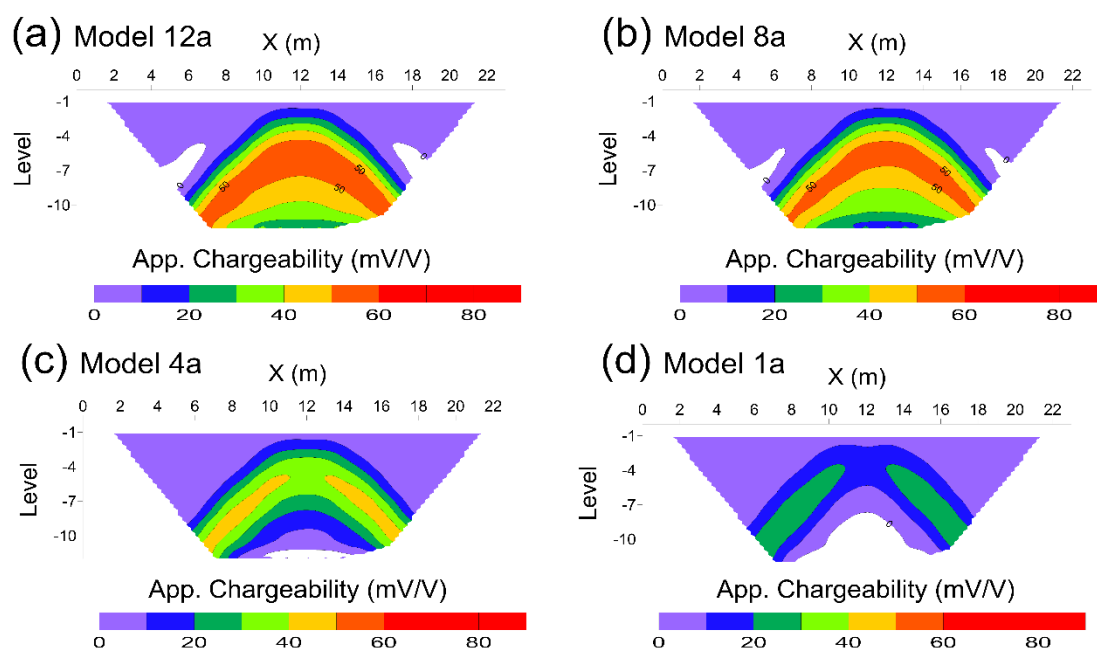


Figure 4. 15. Pseudo section of the 1st and 3th IP channels for model 12a (a) to model 1a (d).

The apparent chargeability pseudo sections for all 4 models are presented in Figure 4. 15. The apparent chargeability of the 1st channel (Figure 4. 15 top) is decreasing rapidly as the prism becomes shorter in its 3rd dimension and this holds for every channel (Figure 4. 15 bottom).

The TDIP resistivity inversion results (Figure 4. 16) show that the resistivity image is very similar for the Models 12a, 8a and 4a, while there is a noticeable difference for the case in the Mode 1a.

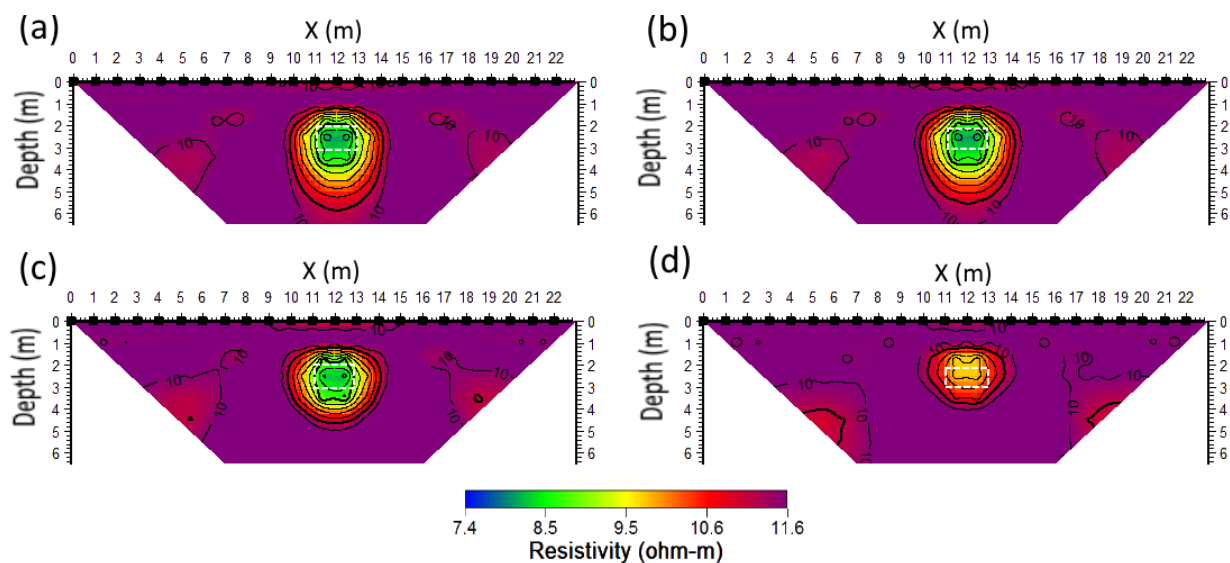


Figure 4. 16. Inverted Resistivity images for Model 12a (a) to Model 1a (d).

The inversion results of the 1st TDIP channel for every model are plotted in Figure 4. 17, and the presented images reveal the decrease in the value of chargeability (expected from the pseudo section) as the model size is reduced and departs from the 2D assumption. On the other hand the boundaries and the shape of the chargeable body can be seen in all images; however the chargeability value decreases very fast as the 3D effect is increasing especially for the Models 4a and 1a. As the prism is shorten not only the chargeability value drops but also the chargeable zones seem to be more and more concentrated at the top part of the prism.

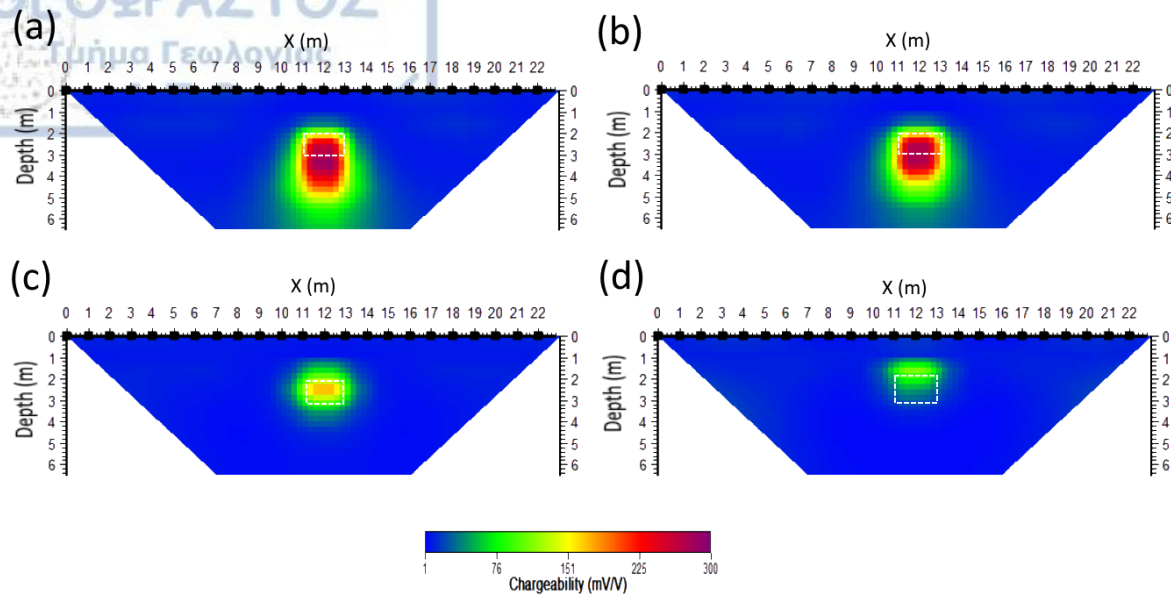


Figure 4. 17. Inversion results for the 1st IP channel for model 12a (a) to model 1a (d).

By inspecting the intrinsic chargeability curves for selected blocks of the different Models (Figure 4. 18) it can be seen that even though the chargeability values are decreasing with the decrease of the prism's strike direction, the remaining Cole-Cole parameters of the model should not be affected i.e. the general shape of the curves remains the same.

The particle swarm optimization algorithm was applied to calculate the Cole-Cole parameters for the blocks of the model which correspond to the perturbing prism for all four Models.

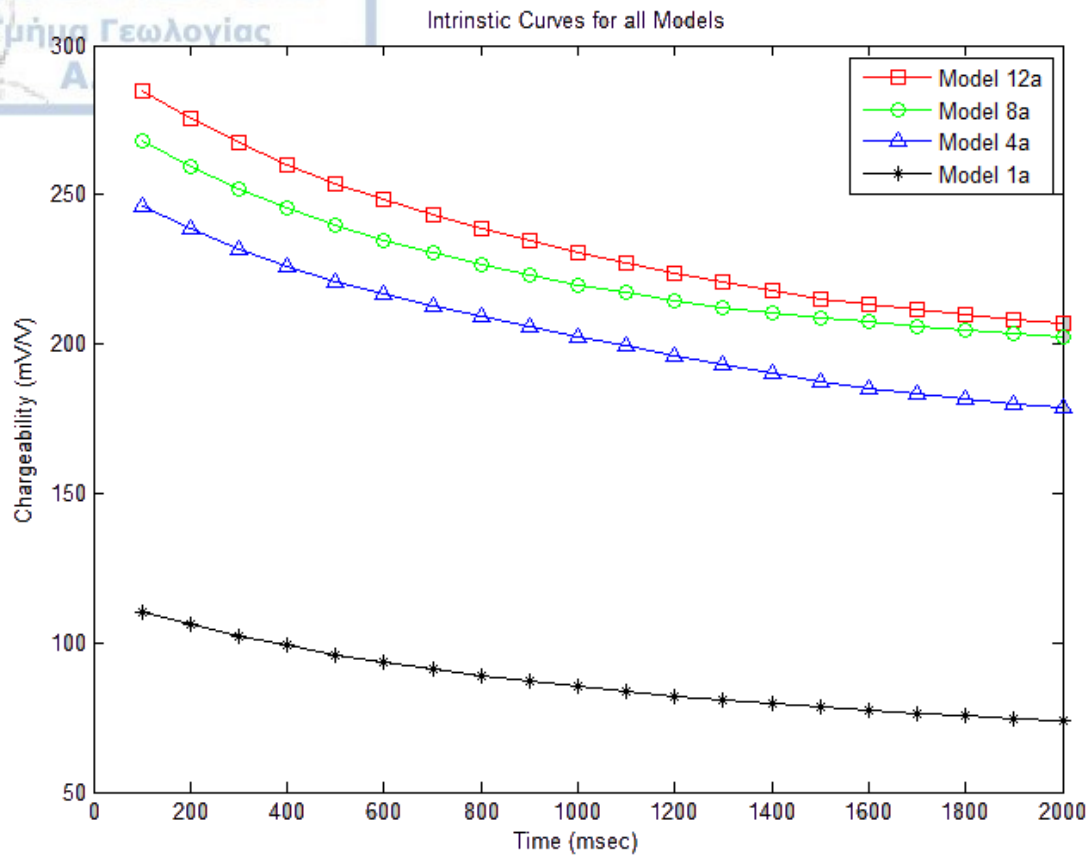


Figure 4. 18. Intrinsic chargeability curves all 4 models.

The results of the Particle Swarm Optimization for the model block that contain sufficient signal will be represented in Table 4. 4.

Particle Swarm Optimization for Model blocks					
	Original	Model 12a	Model 8a	Model 4a	Model 1a
chargeability	400	300	300	270	120
τ	10	8.9	8.9	7.6	6.0
c	0.70	0.61	0.63	0.63	0.59

Table 4. 4. Particle Swarm Optimization results for each model used in the study of the 3D effect.

The results indicate that the first two models (12a and 8a) have very similar behavior not only regarding their resistivity and chargeability image but also to the intrinsic chargeability values calculated. This can be seen at first from the behavior of the curves and then can be further verified by the optimization results.

The value of relaxation time (τ) is decreasing while the size of the Model decrease. This behavior is very similar to the decrease of chargeability indicated that might be a correlation between these two values. On the other hand the value of frequency dependence (c) has very similar values for the four different Models.

4.5 Concluding Remarks

In this section some of the conclusions that came out from the study of the synthetic models are summarized.

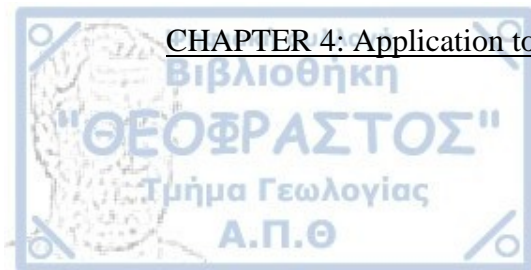
The TDIP inversion managed to retrieve the boundaries of the chargeable bodies quite successfully without being influenced significantly by artefacts appearing into the resistivity inversion. In many cases the chargeability boundaries of the body compared to the resistivity ones appear to be displaced as chargeability tends to concentrate at the upper part of the modeling body. This inversion artefact needs to be taken into account when intercepting real data. The intrinsic chargeability value, n_0 , mainly affects the level of the curve and can be computed more accurately than the other parameters. The relaxation time and the frequency dependence affect the decay's curve shape and they are more sensitive to noise.

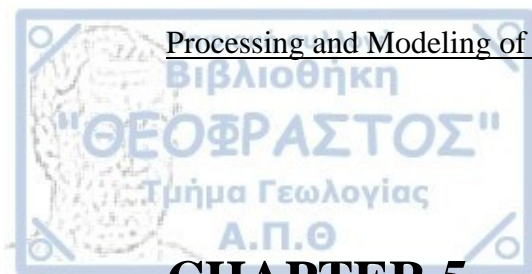
The retrieval of the Cole-Cole parameters of the model can be made accurately enough for intrinsic chargeability curves with the use of the Particle Swarm Optimization algorithm, especially for model blocks with high level of signal. On the other hand, the solution is less robust for model blocks with low signal level (e.g. the background or non-chargeable prisms) however this can be identified and can be alleviated by slightly modifying the optimization algorithm. Finally, it should be noted that the Particle Swarm Optimization results are generally stable and do not require a

valid initial solution, as in Particle Swarm Optimization case this is picked randomly and does not affect the results.

Even though the calculated intrinsic values of the Cole-Cole model cannot be directly linked with any materials they can be used to verify if a signal with the same resistivity and IP response is caused by similar or different materials.

The reduction of the length of a prism in the direction perpendicular to the array (3D effect) would lead to a reduction in the chargeability value similar to the resistivity one. From the spectral processing point of view of the models, the retrieved value for the relaxation time, τ , is also reducing with the size of the prism however the retrieved value for frequency dependence, c , is not affected.





CHAPTER 5

Application to Real Time Domain IP data

The results from the processing of the synthetic models was very useful to validate and develop a scheme for TDIP data processing. However the scheme developed in this work need to be further tested with real data.

Prior to the processing of the real data, the data need to be checked for their data quality. For that reason a tool was developed in matlab (with Graphics User Interface) that has the ability to exterminate possible bad measurements. The graphics user interface gives the ability to have full control over the filtering options.

The first two examples are from experimental data that was collected in a tank filled with water in the facilities of Aristotle University of Thessaloniki. First, a conductive and chargeable metal pipe was dived into the water in different depths, to calculate the response and then another set of two pipes with same material and different lengths was used to study the 3D effect.

Last, the measurements from a survey that took place inside the campus area, where metallic pipes from the University network are buried, will be further processed about their TDIP information.

5.1 Pre Processing

Testing of the described TDIP inversion and Cole-Cole parameters retrieval scheme with real data is very crucial in order to evaluate the effectiveness of the entire approach. As real TDIP data commonly suffer from noise it is very important to filter data prior to inversion. However, during the course of this work it was realized that the existing tools regarding the pre-processing of the TDIP data were not enough to evaluate data quality and filter TDIP data. In particular the existing pre-processing software which supports the instrumentation used in this work (Prosys software for Syscal-Pro) has only limited TDIP curve evaluation and filtering options so it was not adequate. As a result a special Matlab based program was developed within this thesis to support TDIP data preprocessing.

There are many ways to evaluate data quality so in this work a basic DC geoelectrical data quality evaluation scheme proposed by Kim et al. (2016) was adopted and extended for the TDIP case. Two filtering options based on this work were adapted and added in the new filtering tool. A further option based on the decay curve shape was also introduced in this work to filter TDIP decay curves.

Filtering can be fully automated however a graphic user interface was created to give the user the ability to choose which filtering options should be used. The main window (Figure 5. 1) gives basic options to the user, as to which files to export, which IP channels to process and which filters to apply. The advanced options window (Figure 5. 2) give the user the ability to further modify the operation of each individual filter, to the best needs based on the survey type.

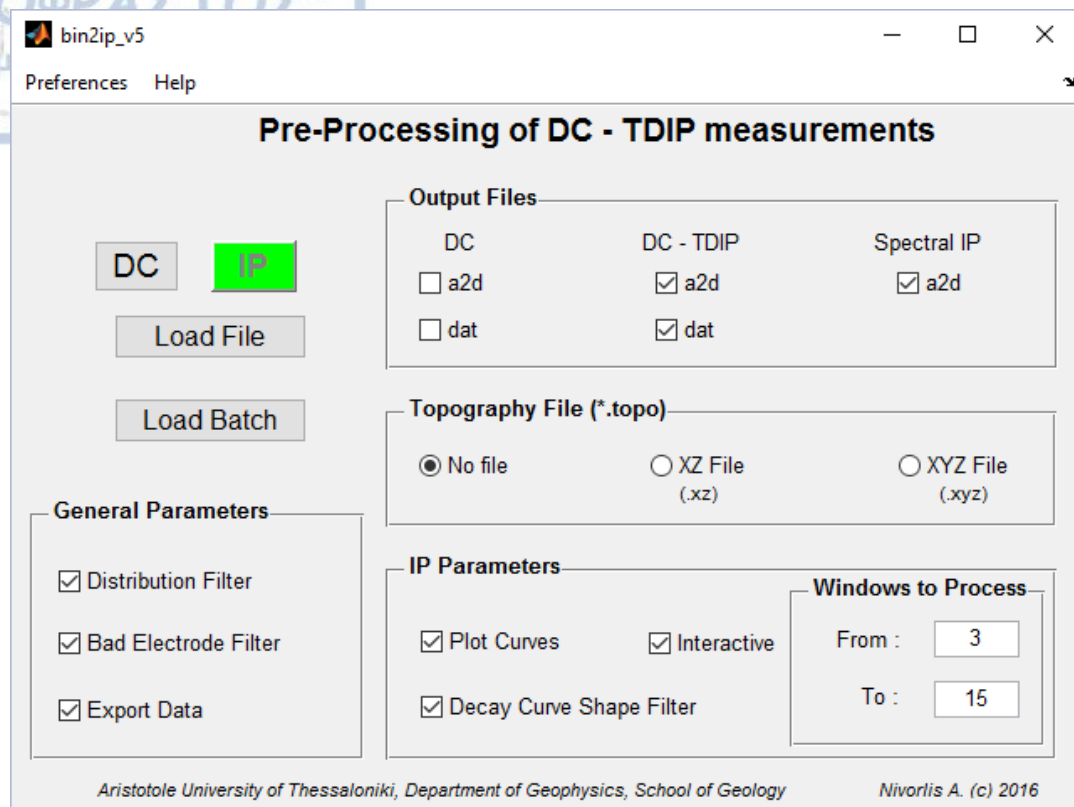


Figure 5. 1. Pre Processing tool Main window.

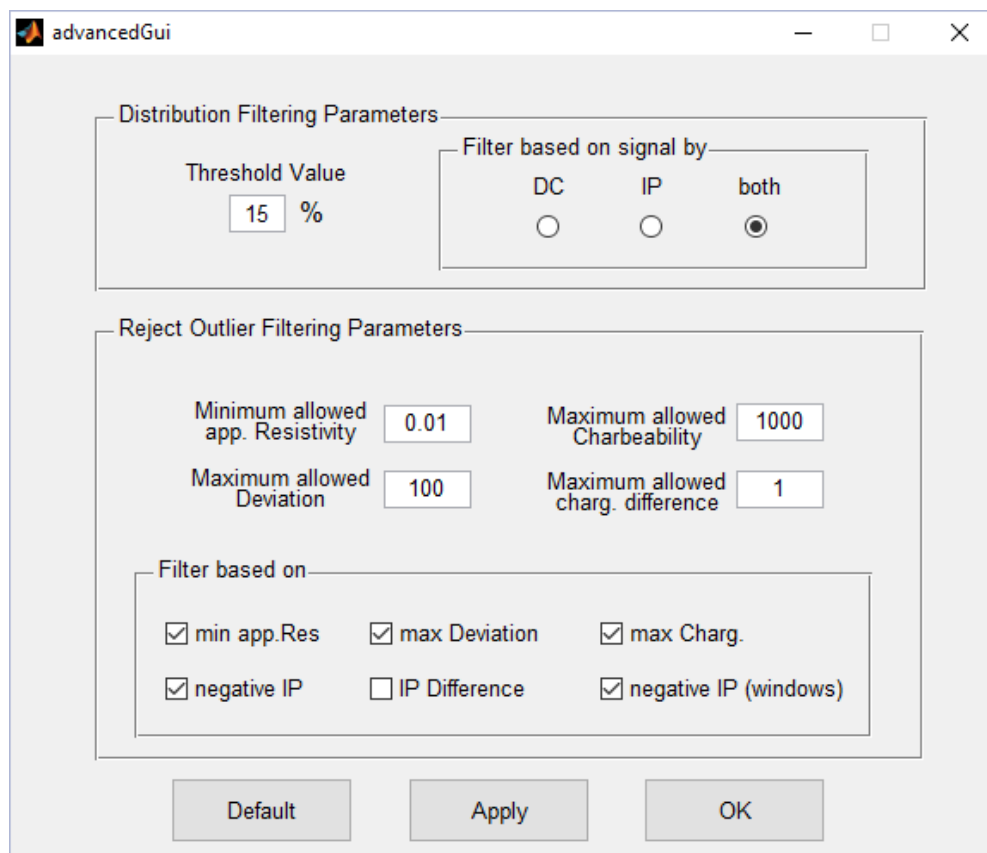


Figure 5. 2. Advanced Options.

Distribution Filtering: First, the data are filtered on the basis of their signal to noise ratio. Based on the apparent resistivity equation (eq. 2.4) measurements with high geometrical factors are more susceptible to noise due to their low signals (Figure 5. 2). At the same time apparent resistivity measurements which highly depart from the mean value of the data set can also be susceptible to noise.

The scheme automatically filters measurements which have two common characteristics: low signal (i.e. high geometrical factors) and relatively extreme apparent resistivities values. This is achieved by using some predefined threshold values which the user can modify depending on the situation.

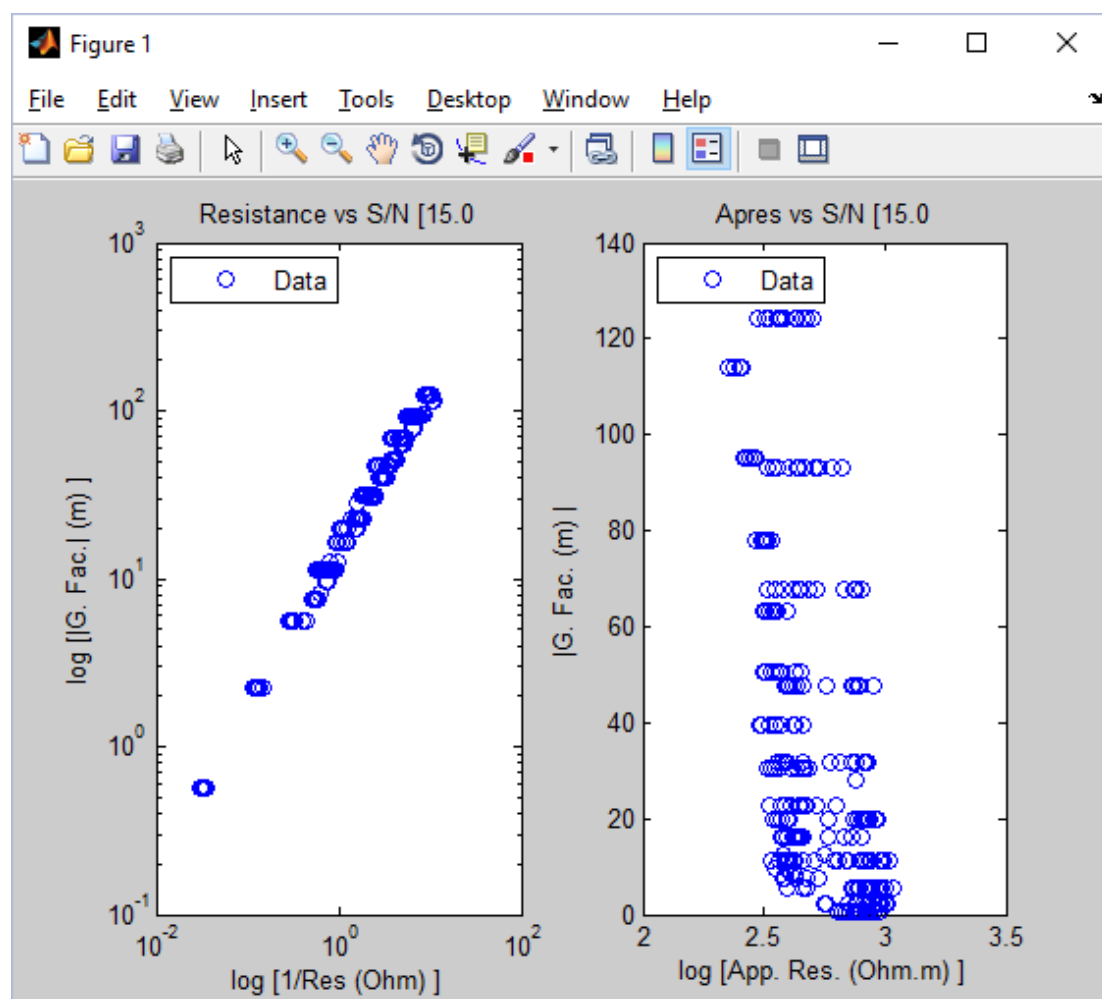


Figure 5. 3. Measurement Signal to Noise plot

Bad electrode Filtering: Next, a filtering to control the possibility of a “bad” electrodes was also included. For every electrode the mean of all the measurement errors associated with this electrode is calculated. Note that measurement errors are recorded by the instrument as the measurement is repeated several times for every data point. The graph of the mean error for each electrode (Figure 5. 4) is plotted and the user has the option to exterminate a possible bad electrode. This is very useful in cases where an electrode is disconnected during the measurement.

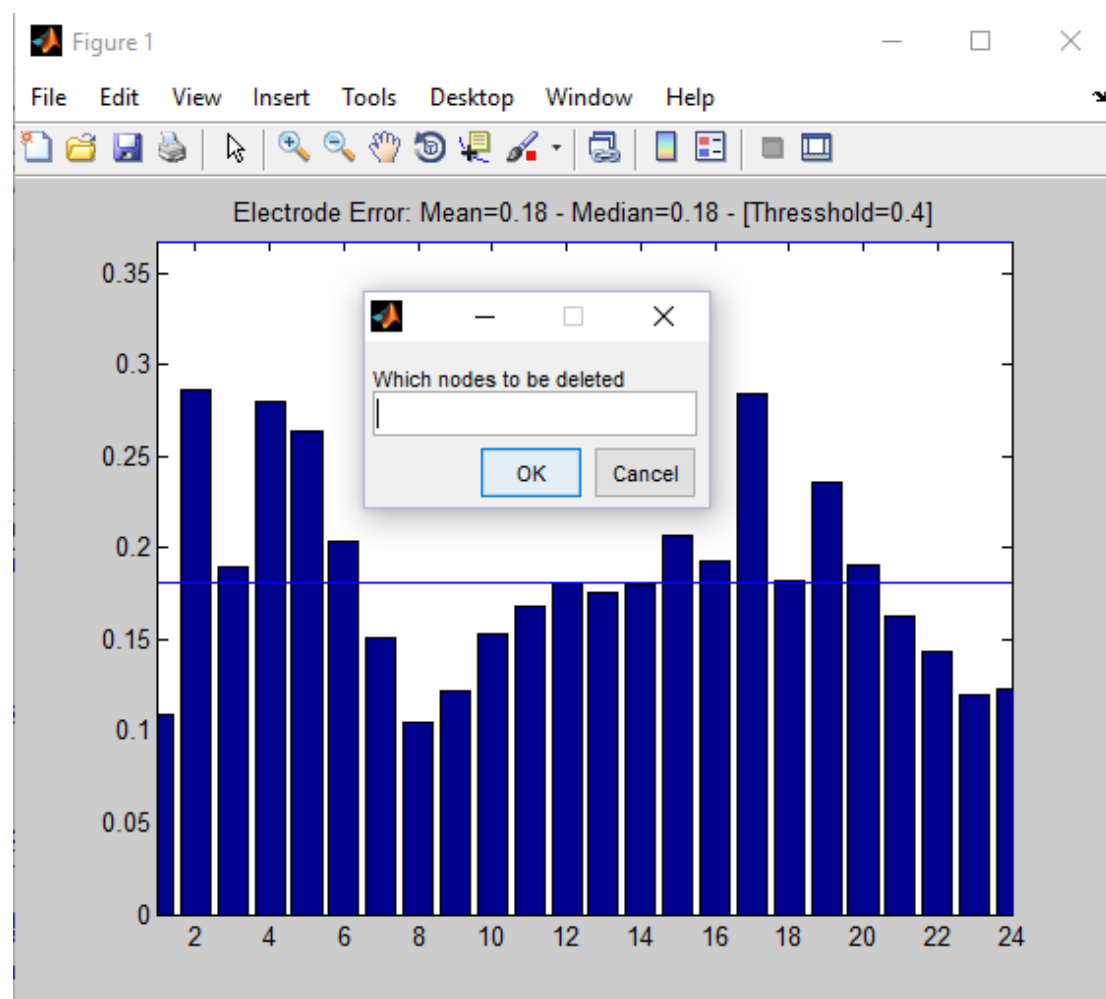


Figure 5. 4. Bad electrode filtering

Decay Curve Shape Filtering: The tool was developed in the first place to give the option to visualize the spectral information of the decay curve. As however in this work the decay curves were assumed to follow the Cole-Cole model the apparent decay

curves were expected to be decaying monotonously so the filter rejects measurements which do not fulfill that criterion.

In the case that the shape of the curve is erratic but the measurement itself has very low chargeability value, the chargeability value of that measurement is replaced by a near zero value (i.e. mean of the absolute value of the windows) in order to include more measurements into the inversion process.

Although this scheme provides an automated way of filtering the TDIP measurements a checkbox is added to each graph giving the control to the user. At any time, the user can choose to reject or accept a measurement no matters the result of the automatic filtering.

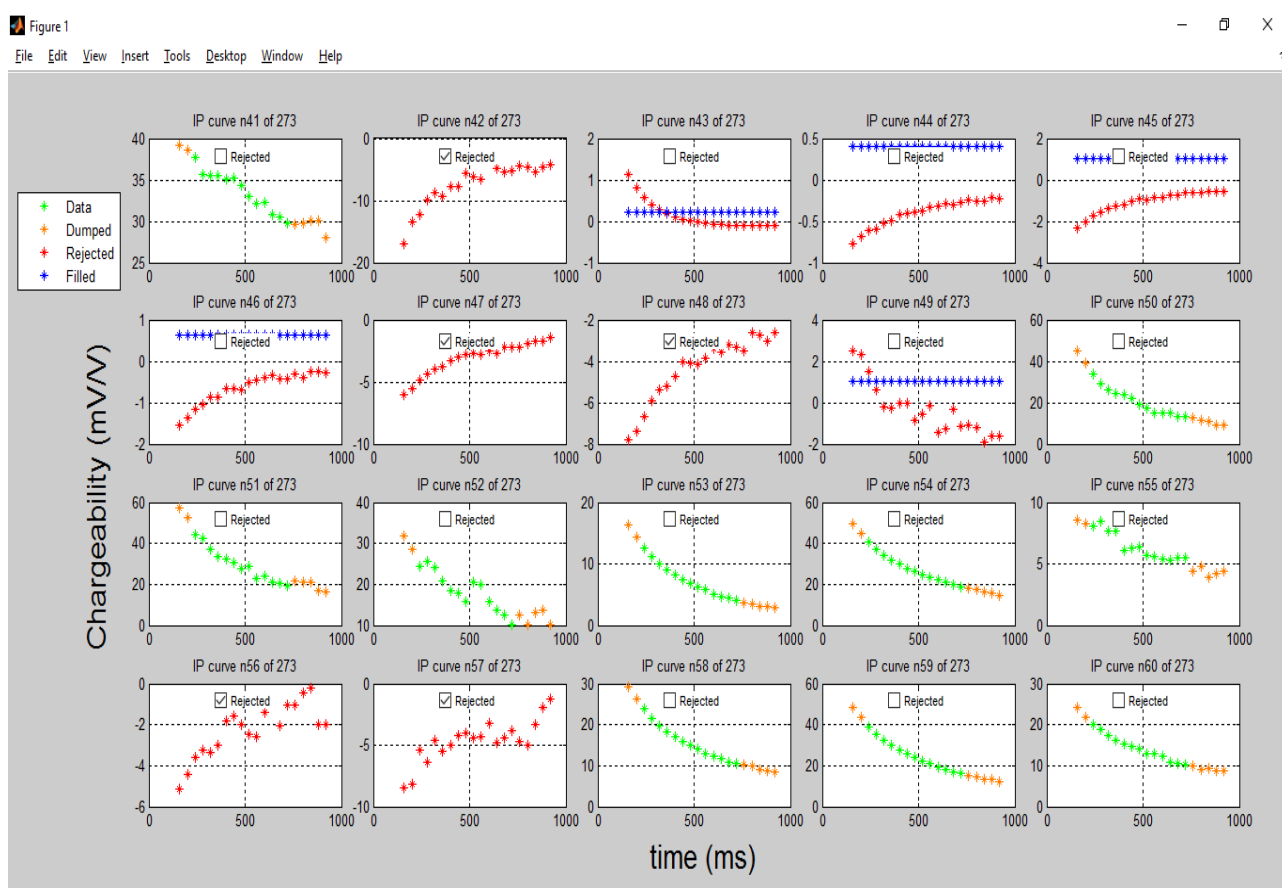


Figure 5. 5. Decay Curve Shape Filtering.

5.2 Experimental Data

5.2.1 Introduction

The experiment took place at the facilities of Aristotle University of Thessaloniki using a PVC tank (0.80m x 0.80m x 1.10m) filled with tap water of average resistivity of 22 Ohm-m while the water level was up to 40 cm from bottom.

Plastic pipes were used as the frame for the electrode array and stainless steel screws were used as electrodes. Extra wooden elements were used on top to help with the support of the array's frame as well as to hang the targets and hold them at the desired depth. The tank setup can be seen in Figure 5. 6.

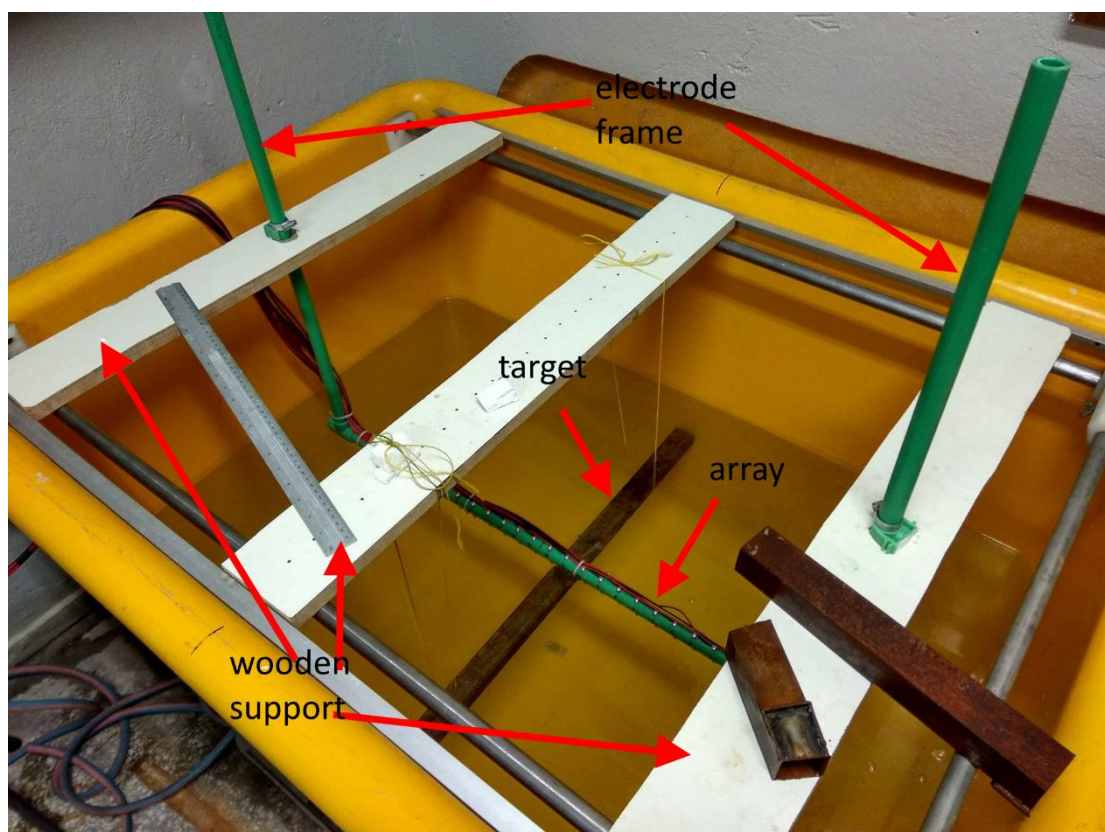


Figure 5. 6. Experimental Tank set up.

The electrode array had 24 electrodes with electrode separation $a=3\text{cm}$ i.e. the total length of the array was 69 cm. The measurements were taken using the dipole-

dipole configuration with dipole separation (a) and (2a) and maximum dipole separation equal to 7.

5.2.2 Background Measurement

To begin with a measurement with no other objects inside the tank was taken. This measurement was used to verify the equipment and the setup and to evaluate potential tank related inversion artefacts. The average contact resistance observed during the experiments was 1.5 KOhm.

The results of the background inversion can be seen in Figure 5. 7. Resistivity inversion reveals a conductive layer bellow 0.18 cm. This is an artefact as there is nothing to justify the existence of this low resistivity layer and might be due to the boundary effects or EM effects that affect the large separation measurements.

The inverted chargeability image exhibits no similar artefacts (i.e. the bottom layer) due to the nature of the inversion scheme which produces chargeability inversions referenced to the DC resistivity so artefacts tend to cancel out. A minor very low (5mV/V) chargeability anomaly at the right end of the array is considered only a minor artefact.

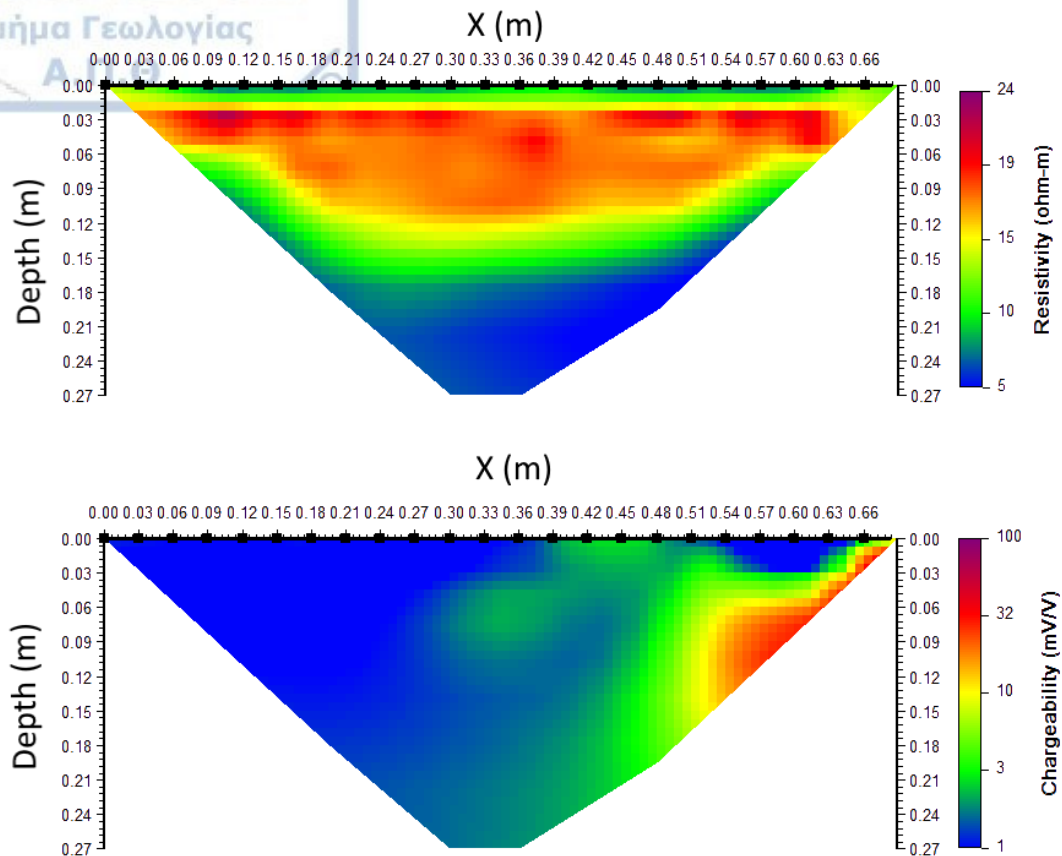


Figure 5. 7. Tank background experiment inversion results (nothing but water).

5.2.3 Experiment 1 – Metal Pipe Down lift

5.2.3.1 Experiment Geometry

On the first experiment the response of a metallic pipe positioned at different depths in the center of the array was measured. The pipe has a radius of 3 cm radius and was hanged with its center at 6, 9, 12 and 15cm below the surface of the water for experiment A, B, C and D respectively as can be seen in Figure 5. 8.

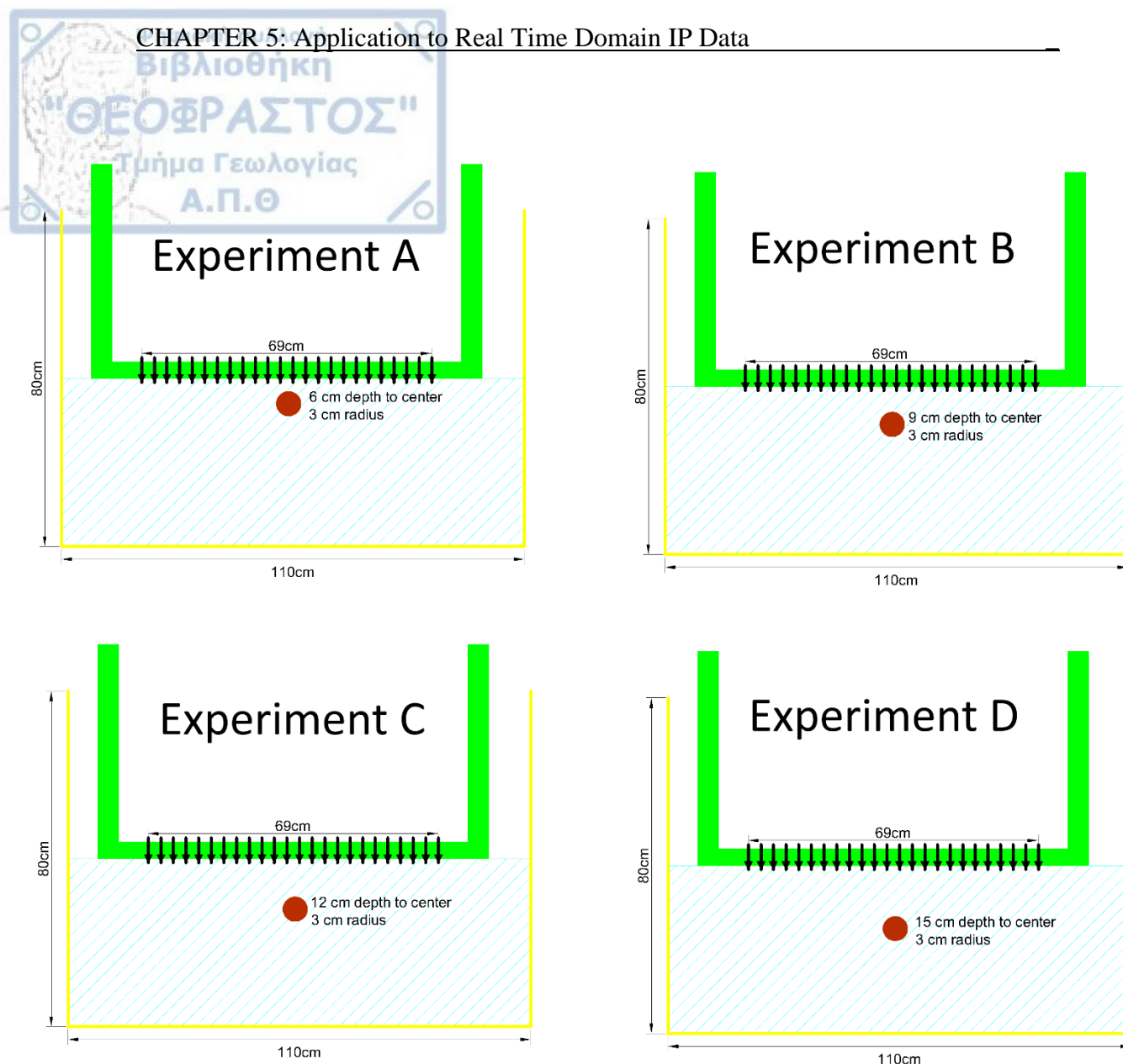


Figure 5. 8. X-Z slice of the geometry of each experiment.

5.2.3.2 Inversion Results

After the pre-processing the datasets from every experiment were inverted to calculate the distribution of the resistivity and chargeability, using the TDIP inversion algorithm. The resistivity image shows that the conductive layer at the bottom of the model, below 18 cm is still present. This artefact is still present and suggests that below 18 cm any object will probably not be visible.

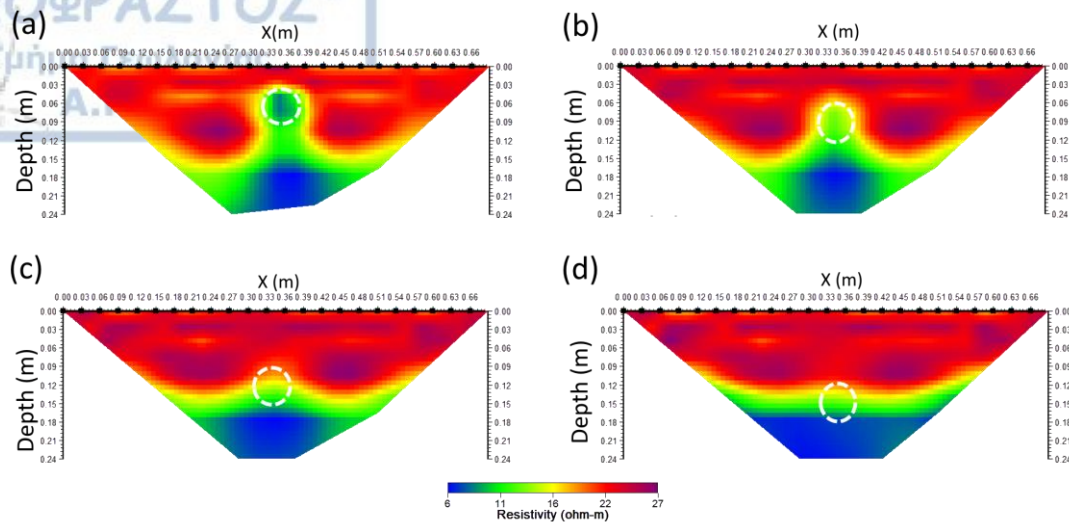


Figure 5. 9. Inverted resistivity image for the experiments.

The inverted resistivity images for all experiments can be seen in Figure 5. 9. The target is successfully shown at the inversion results of experiments A and B but in experiments C and D the target is only marginally visible mainly due to the existing low resistivity layer (artefact) which masks the conductive body which anyway is at a depth in which inversion has a low resolving ability.

The respective chargeability inverted images are quite different (see Figure 5. 10 and Figure 5. 11) in all experiments the target can be accurately located. Also, even though that the target is the same the inverted chargeability values are reduced in amplitude as the depth of the target increase which reflects the reduced resolving ability of the inversion as the target depth increases. Again the low resistivity bottom layer artefact is not shown in any of the TDIP inverted images.

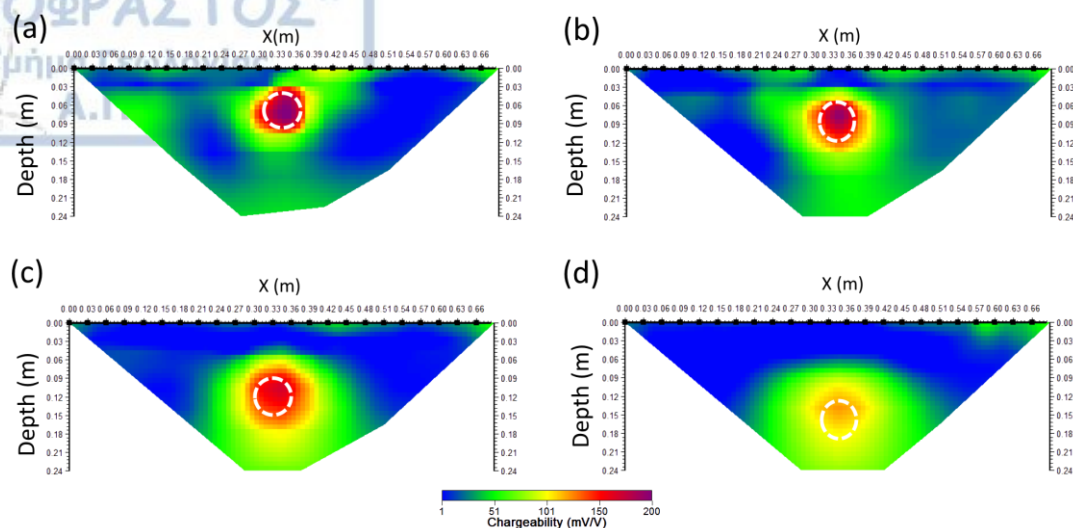


Figure 5. 10. Inverted Chargeability of 3rd Channel (400-480 ms).

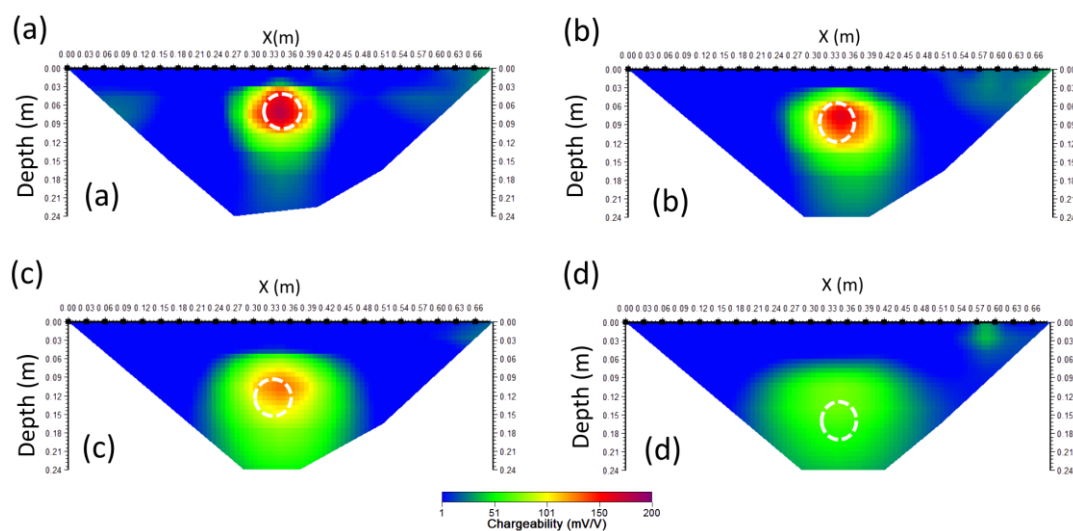


Figure 5. 11. Inverted Chargeability of 13th channel (1360-1440).

5.2.3.3 Cole-Cole Model

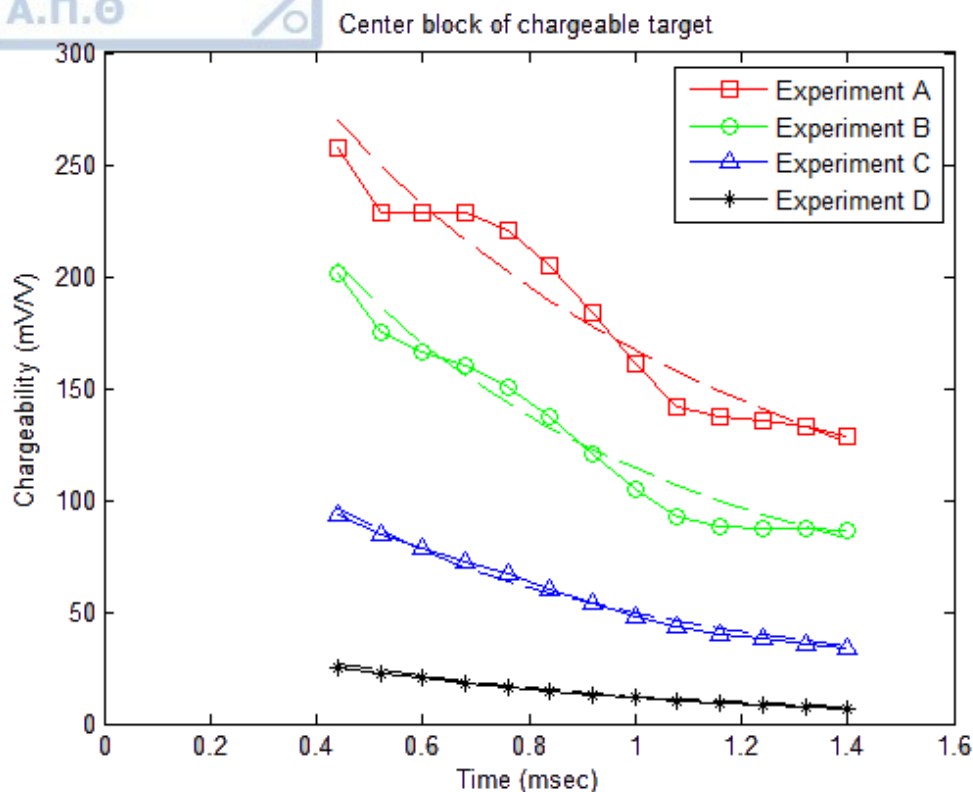


Figure 5. 12. Intrinsic chargeability curves of the central block. The Particle Swarm Optimization fit can be seen with the dashed line.

In order to evaluate the inverted results regarding the Cole-Cole parameters the TDIP decay curves of the central block were extracted and are presented in Figure 5. 12. The different chargeability levels of the curves is because of the different chargeability values which reflect the reduction in amplitude as the depth of the target increases. However the curves exhibit similar decay patterns which are also expected to be reflected on the calculated Cole-Cole values. This is pronounced for the case of the first two experiments where the target is close to the surface and the signal is generally high. On the curve of the third experiment this pattern is almost not visible probably due to the reduced level of the signal and of course on the last experiment's curve the signal has dropped very low for that pattern to be seen.

The Particle Swarm Optimization results for the center model block are rather interesting and they are summed up in the table below.

Particle Swarm Optimization for the Center block of the Chargeable body

	n_o	$T\alpha$	c
Experiment A	0.47	0.90	0.83
Experiment B	0.35	0.80	0.91
Experiment C	0.17	0.80	0.95
Experiment D	0.050	0.70	0.98

First the results indicate a strong correlation between the values of intrinsic chargeability and τ . When the chargeability values for a given body drop (because of different depths), the values of τ decrease as well. This pattern however does not appear to apply for the values of c . The calculated frequency dependence values remain rather constant indicating that the shape of the curve is not changing that much.

5.2.4 Experiment 2 – 3D effect

5.2.4.1 Geometry

On the second experiment two square metallic pipes with 4cm cross-side length were used. The top of the pipes was inserted at a depth of 5cm from the water surface. The length of the first pipe was 77 cm and the length of the second pipe was 10 cm. The pipes were used in order to simulate the 3D effect into the 2D inversion and the geometry of the experiment is depicted in Figure 5. 13.

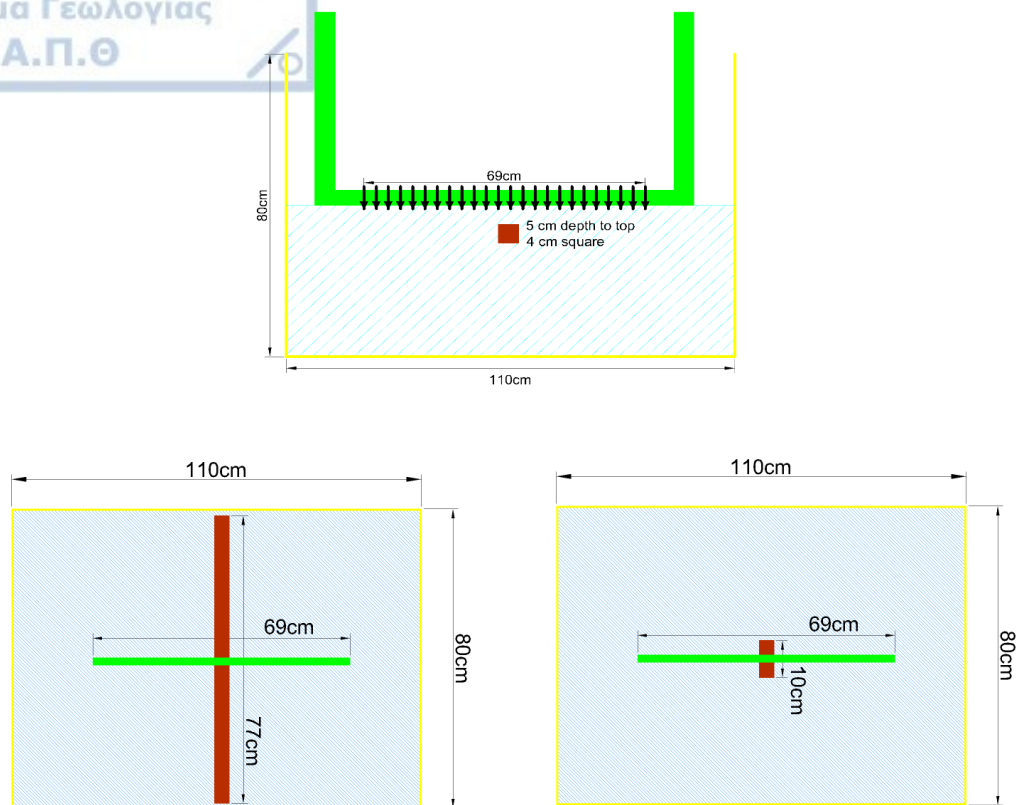
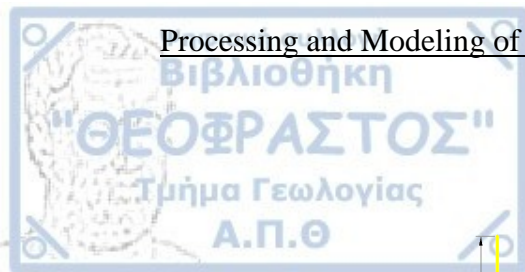


Figure 5. 13. Geometry of 2nd experiment. X-Z slice (top) and top view (bottom).

5.2.4.2 Inversion Results

The inverted resistivity images for the long and short pipes along with the respective TDIP inversion results for time channel 1 can be seen in Figure 5. 14. The resistivity inverted section for the case of the long metal pipe delineates the metal target although the image might be confusing at first, knowing that the conductive layer on bottom is an inversion artefact. The inverted resistivity image for the shorter pipe, even though the target is still visible there is a slight displacement of the target closer to the surface.

The results from the inverted chargeability image do not differ that much from the resistivity ones. The target loses amplitude as the extension of the target's Y

dimension is reduced and this reduction in the amplitude lead to a misplacement of the target, hence the target appears closer to the surface in a similar way observed in the analogous synthetic model.

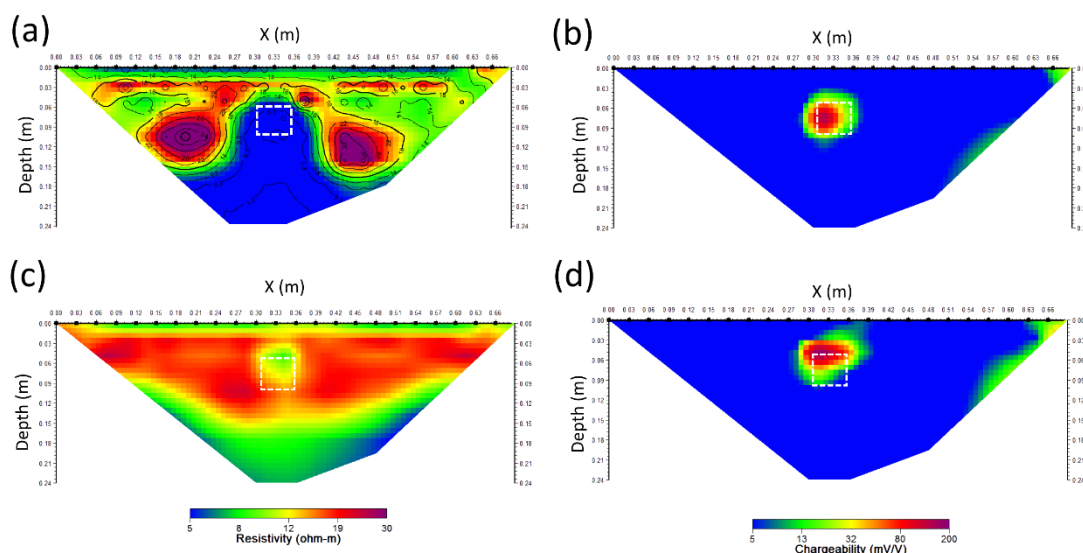


Figure 5. 14. Inversion Results for experiment 2 (3D effect) for the long metallic pipe (top) and short metallic pipe (bottom).

5.2.4.3 Cole-Cole Model

From each model, the chargeability of the center model block of the chargeable body was extracted in order to calculate the Cole-Cole parameters. Based on the synthetic model observations we expect that the resulting intrinsic chargeability curves would have very similar shapes but different amplitudes.

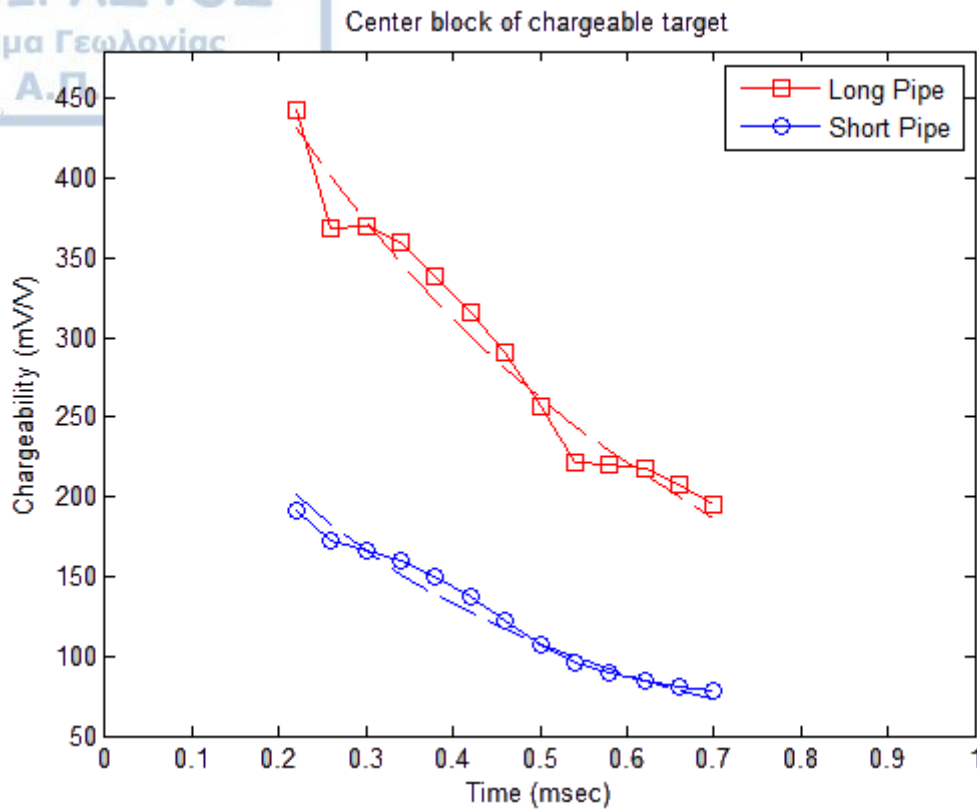


Figure 5. 15. Intrinsic chargeability curves. The Particle Swarm Optimization fit can be seen with dashed line.

Indeed as it can be seen in Figure 5. 15 the decay pattern of both curves is very similar and could be related to the behavior of the same material of the pipes. The similar shape of the curves should be reflected on the values of frequency dependence, which expected to be very close.

On the other hand, as we have seen so far, the reduction of the amplitude of the response should not only reduce the chargeability value but also the value of relaxation time, τ . The results of the Particle Swarm Optimization for the center model block can be viewed in the following table.

Results of the Particle Swarm Optimization for the Center Model Block			
	n_0	τ	c
Long Pipe	662	0.54	0.96
Short Pipe	375	0.39	0.90

The above hypothesis is verified by the results as there is a clear reduction of the amplitude of the signal which also correlates with the reduction on the τ parameter,

while the value of frequency dependence remains at the same level for both long and short pipes.

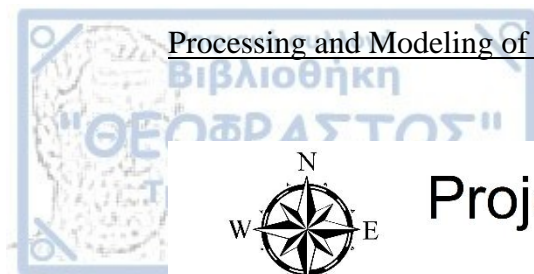
5.3 Real Data

5.3.1 Introduction

The measurements used in this work were collected in December 2015, during the field practice involved into the applied Geophysics master's program of the A.U.Th. The location chosen was inside the university campus, next to the Observatory building (Figure 5. 16), where a number of metallic utility pipes are known to be buried.

The dipole-dipole array configuration was chosen for the survey with inter-electrode separation of 1m. A total of 10 parallel ERT lines were measured having an interline spacing of 1 meter in order to create a 3D representation of the subsurface (Figure 5. 16), Each line was processed in 2D and then all lines were assembled to a single 3D data set and they were also subjected to a full 3D inversion. Note that the 3D inversion for the geoelectrical and the IP data (not in TDIP mode) were conducted using the RES3DINV software (Loke, 2004).

The inverted 2D TDIP results for the first, middle and last ERT lines were further processed with the use of the Particle Swarm Algorithm to calculate the Cole-Cole parameters of the bodies.



Project Meteo 18/12/2015

1:300

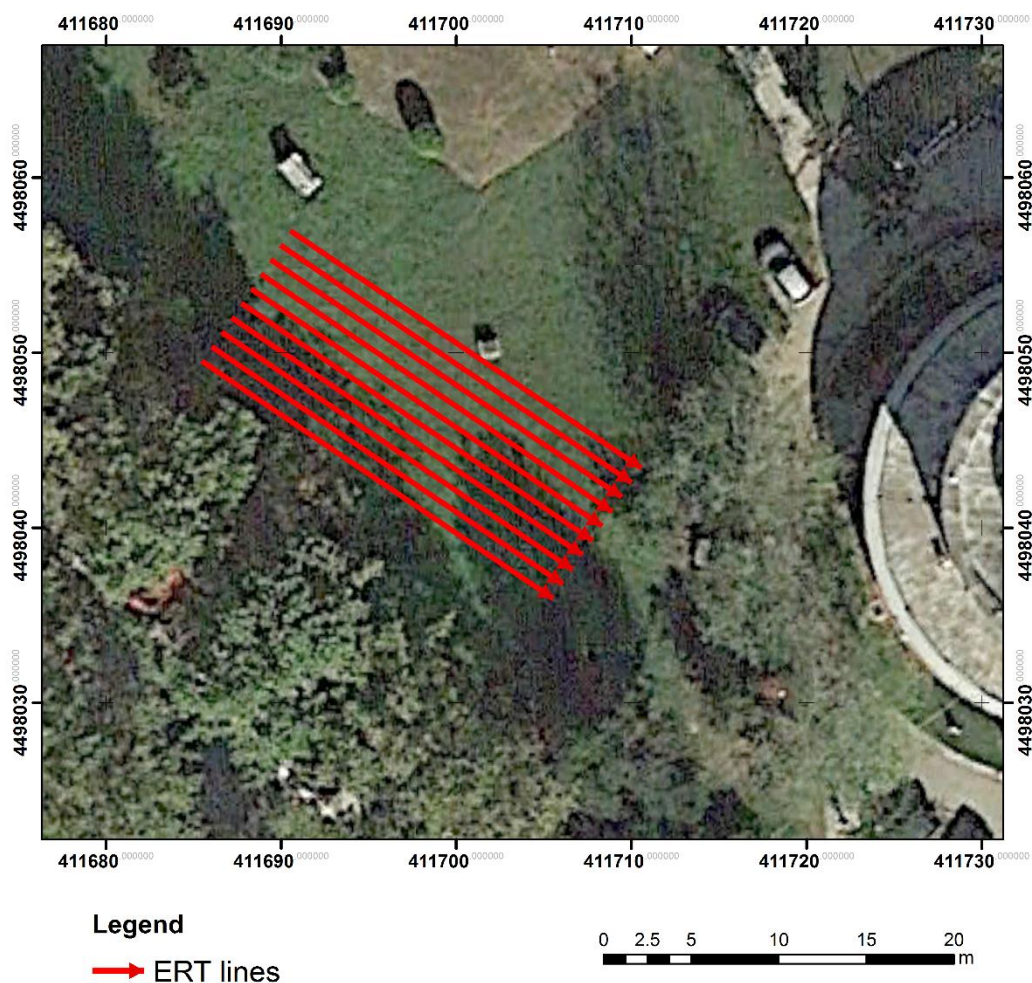


Figure 5. 16. Location of the survey. Observatory building can be seen on the right edge of the map.

5.3.2 Inversion Results

The 2D in resistivity images and the TDIP inversion results for time channel 1 can be seen in Figure 5. 17 for the 3 ERT lines. The 2D geoelectrical sections indicate the presence of two different conductive and chargeable bodies with discrete boundaries (white dashed lines), in a relatively resistive environment. These bodies are probable the metallic pipes which are buried in the top layer. As it can be seen from the results the targets appear at different X locations at the 3 inverted sections

suggesting that the targets (i.e. metal pipes) are not perpendicular to the survey lines. Both targets have a Northeast – Southwest direction (~60 degree).

The respective TD chargeability image (time channel 1) for those targets show a relative misplacement when compared to the resistivity image. The chargeability concentrates on the upper half of the bodies and this could be attributed to the fact that the targets are not perpendicular to the line and this has a 3D effect on the measurements.

The chargeability inverted images suggest the existence of a 3rd chargeable target (possible pipe) which is buried deeper and is marked with the red dashed line in Figure 5. 17. Although its boundaries are not clearly outlined it is present in all three ERT lines and appears to have quite a strong signal.

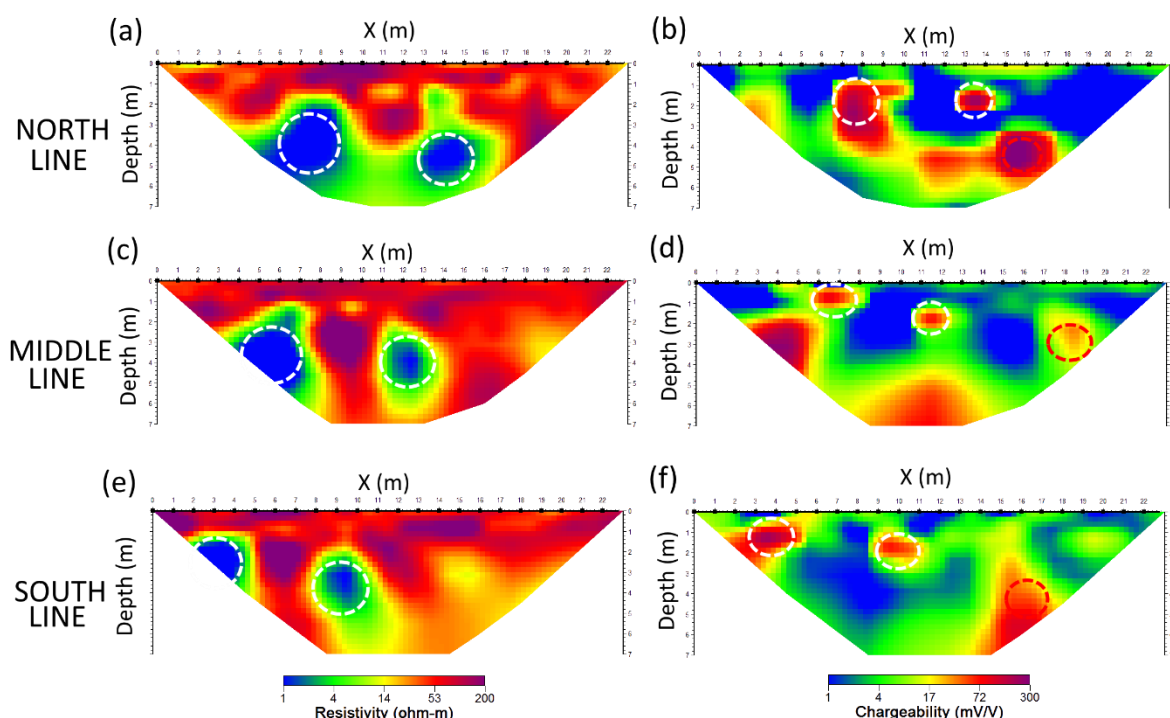


Figure 5. 17. Inversion results for north line (top), middle line (middle) and south line (bottom).

The 2D ERT lines was merged into a 3D file and inverted using a 3D inversion algorithm (Res3DInv) which support also 3D IP inversion. The results of the 3D

inversion algorithm were rendered into 3D display program (Golden Software Voxler) for better visualization and can be seen in Figure 5. 18.

The isosurfaced used in this image highlights the misplacement of the chargeability image (orange color) with the respective resistivity image (blue color) for the right pipe. The IP is concentrated on the upper part of the conductive body. Due to the fact that the signal is stronger for that pipe (shallower target) this pipe was chosen to illustrate this effect in 3D. The results are similar (not shown here) for the other pipe as well, as can be verified from the 2D inverted images as well.

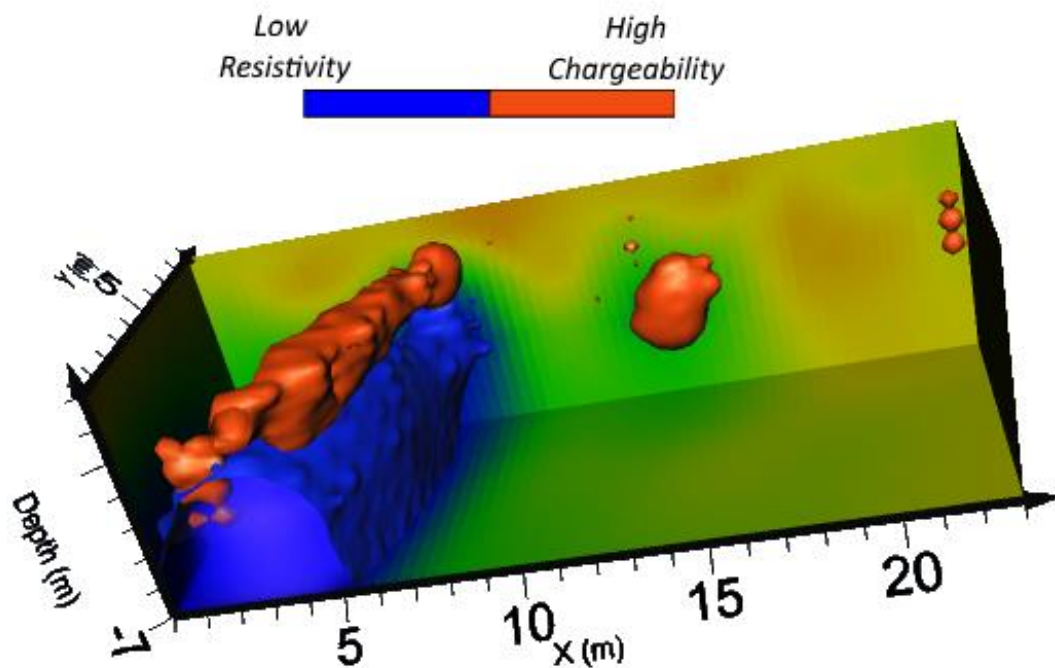


Figure 5. 18. 3D inverted model of survey.

5.3.3 Cole-Cole Model

The 2D TDIP inversion results for the three ERT lines were subjected to the Particle Swarm Optimization processing and the results for the τ and c Cole-Cole

parameters are shown in Figure 5. 19. The response of the first pipe (left white dashed line) indicate τ values around 0.40 and c values close to 0.92 and for the other pipe (right white dashed line) lower τ values around 0.25 and lower c values around 0.85 (Figure 5. 19).

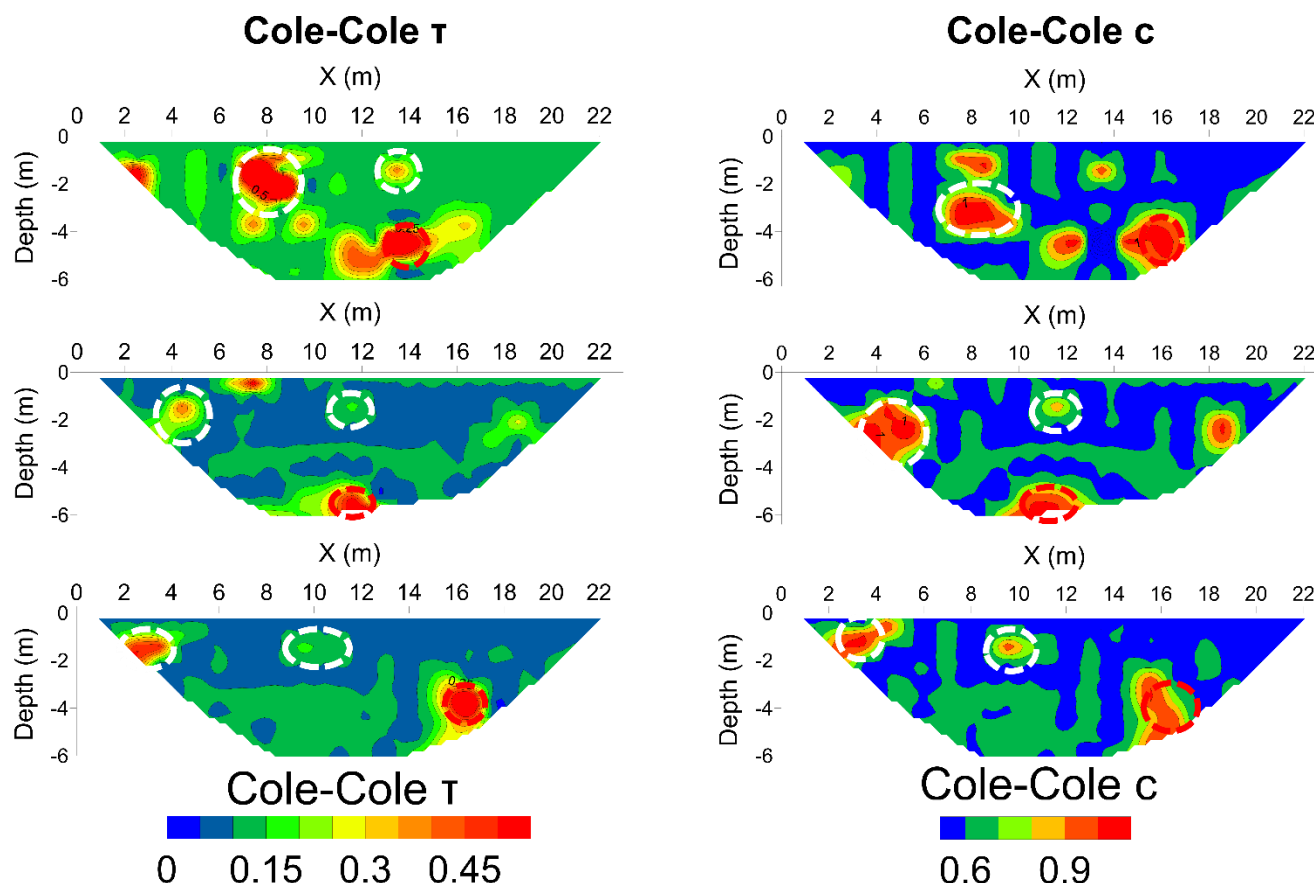


Figure 5. 19. Cole-Cole calculation results for north line (top), middle line (middle) and south line (bottom)

The results have some increased noise level however the image is still informative. The pipe boundaries can be clearly located and the calculated parameter values are pretty consistent along the different lines.

The reduced τ value for the second pipe might be due to the fact that this pipe has reduced IP signal and as we have seen before there is a correlation between the chargeability signal and the relaxation time.

On the other hand, this difference in the frequency dependence (c) parameter indicates that the shape of the curves changes and might be an indicator that those two pipes are from different materials.

5.4 Concluding Remarks

Before the inversion of the measured data collected, it is important to characterize the quality of the data in order to exterminate possible bad quality measurements. Although this process should be automated still the control of the scheme should be with the user. For that reason a Graphic User Interface was created to pre-process TDIP data.

The experimental results from the metallic pipe with different burial depths reveals the strong correlation of the depth of the target with the amplitude of the signal for both resistivity and chargeability. Furthermore, reveals a correlation on the calculated values for the intrinsic chargeability (n_o) and the relaxation time (τ) based on the fitting of a Cole-Cole model on the inverted data.

This correlation appears to hold also for the study of the 3D effects on the 2D inversion which took place over the second experiment. The reduction of the extension of the target over its Y dimension (the direction perpendicular to the array) results into a decreased resistivity and chargeability signal which also results into a decrease of the relaxation time as well. In situations where the target has very little extension across the strike (Y) direction, the inverted chargeability results could lead to false interpretation, due to the fact that there is a significant misplacement of the target's chargeability which tends to appear higher than it actually is.

On the other hand, in both tank experiments the calculated values for the frequency dependence values (c), indicates that this parameter is not affected as much

from the depth of investigation or from the 3D effect because even though the decay curves for the intrinsic chargeability values have different levels (due to the reduced signal) their shape remains very similar. That could be an indicator that the frequency dependence is affected the most by the inner structure and material of the target rather than the level of the signal.

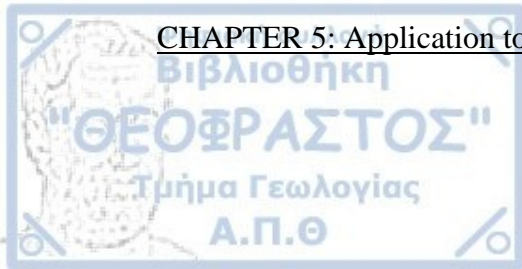
The application of this scheme in real data, verifies that there is a significant displacement of the resistivity and chargeability inversion results regarding the position of the target. As this has been observed in synthetic and experimental data, the resistivity image appears to locate the target more precisely and the chargeability image is misplaced. This misplacement is very obvious especially in situation where the target is not perpendicular to the array (3D effect).

The misplacement of the chargeability image, compared to the resistivity one has been seen in other inversion software (e.g. Res2DInv) as well. This can mean that this behavior is not caused by the specific algorithm used but is caused by an inherent inversion problem. The source of the problem is the way that these algorithms handle the inversion of IP data.

In order to correct the chargeability inversion results a cross gradient inversion has been proposed by Kim (2016, personal communication). This inversion technique can be further used in situation where a priori information about the boundaries of bodies are known to improve the chargeability image.

The Cole-Cole model when fitted to the real data is believed that it could provide useful information about the material of the different chargeable bodies in the sense that it can help to distinguish chargeable bodies with the same level of signal but

different materials rather than characterize a body itself. However this can only be the case when the signal level is strong enough to provide reliable solutions.





CHAPTER 6

Conclusions

The aim of this thesis as described in the introduction was to study the effect of various parameters in Time Domain Induced Polarization data and to develop schemes for processing this type of data. The conclusions drawn by this study will be summarized in this section.

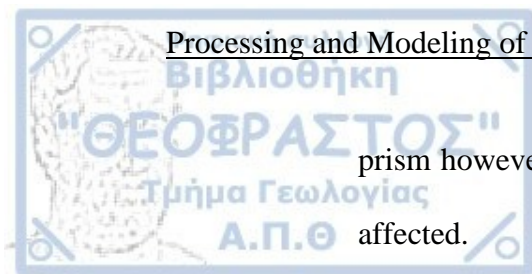
On the basis of the proposed modeling and processing scheme it can be concluded that:

- The modified version of the 3D FEM based solver can produce TDIP data, based on a complex decay model. At the moment only the Cole-Cole model is considered but the scheme can be modified to accommodate different models as well.
- Because of the increased amount of data the forward solution algorithm is slow compared to the DC/IP version however it is stable and can:
 - a) Incorporate complex body geometries in full 3D domain
 - b) Produce solution for any array configuration
 - c) As it can also calculate the Jacobian matrix in the TDIP it can be easily become part of a 3D TDIP inversion scheme in the future.
- Global Optimization Techniques (such as Particle Swarm Optimization) can be successful in retrieving the Cole-Cole parameters. The techniques tend to be robust in view of the data noise and they are

insensitive to the initial estimate of the solution however their use can be time-consuming.

Based on the results from the synthetic, experimental and real data:

- The TDIP inversion managed to retrieve the boundaries of the chargeable bodies quite successfully without being influenced significantly by artefacts appearing into the resistivity inversion. Due to the nature of the TDIP inversion the artefacts present in the DC inversion tend to cancel out.
- In many cases the chargeability boundaries of the body compared to the resistivity ones appear to be displaced as chargeability tends to concentrate at the upper part (shallower) of the modeling body.
- The retrieval of the Cole-Cole parameters of the model can be made accurately enough for intrinsic chargeability curves with the use of the Particle Swarm Optimization algorithm, especially for model blocks with high level of signal.
- On the other hand, the solution is less robust for model blocks with low signal level (e.g. the background or non-chargeable prisms) however these blocks can be identified and the problem can be alleviated by slightly modifying the optimization algorithm.
- The reduction of the length of a prism in the direction perpendicular to the array (3D effect) would lead to a reduction in the chargeability value similar to the resistivity one.
- From the spectral processing point of view of the models, the retrieved value for the relaxation time, τ , is also reducing with the size of the



prism however the retrieved value for frequency dependence, c , is not affected.

- The experimental results from the metallic pipe with different burial depths reveals the strong correlation of the depth of the target with the amplitude of the signal for both resistivity and chargeability.
- Furthermore, it reveals a correlation on the calculated values for the intrinsic chargeability (n_0) and the relaxation time (τ) based on the fitting of a Cole-Cole model on the inverted data.
- In both tank experiments the calculated values for the frequency dependence values (c), indicates that this parameter is not affected as much from the depth of investigation or from the 3D effect because even though the decay curves for the intrinsic chargeability values have different levels (due to the reduced signal) their shape remains very similar. That could be an indicator that the frequency dependence is affected the most by the inner structure and material of the target rather than the level of the signal.
- Before the inversion of the TDIP data collected, it is important to characterize the quality of the data in order to exterminate possible bad quality measurements.
- Even though the calculated intrinsic values of the Cole-Cole model cannot be directly linked with any materials the particular parameters can be used to verify if a signal with the same resistivity and IP response is caused by similar or different materials.
- The application of this scheme in real data, verifies that there is a significant displacement of the resistivity and chargeability inversion

results regarding the position of the target. This was noticed as well in the case of using other commercial inversion software (i.e. Res3DInv) therefore it appears to be an inherent inversion problem. The source of the problem is the way that these algorithms handle the inversion of IP data.

- On the basis of the inversions it seems that the resistivity inverted images tend to produce results which are more representative of the shape of the targets compared to the respective chargeability images. This suggests that there is a scope for the joined inversion of the chargeability and the resistivity results on the basis of structural similarities and this is a current line of research (Kim 2016, personal communication).

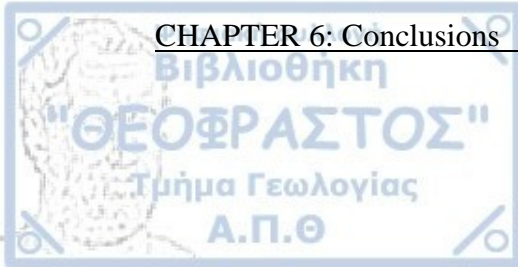
6.1 Future Work

In this work, tried to study several aspects of the TDIP modeling and inversion but it is by no means a complete investigation and so there is much left to be done.

Further modeling is required for more complex geometries in order to validate the results from this work and further test the proposed scheme. Moreover, experimental data for the study of the 3D effect in situations where the target is not located exactly beneath the array should be modelled and collected. Finally, the responses for different array configurations should be simulated as well.

The accuracy of the 3D TDIP forward solution should be extensively tested and more intrinsic chargeability decay models should be supported (e.g. Debye). A full 3D TDIP inversion scheme should be developed based on the forward solution.

Further both 2D and 3D TDIP inversion algorithms could be expanded to support time-lapse (4D) inversion. Furthermore, the filtering utilized in this work should be extended to support time lapse (4D) filtering.



References

- Barker, R.D. (1981). Depth of investigation of collinear symmetrical four-electrode arrays. *Geophysics*, 54, 1031-1037.
- Box, G.E.P., and Kanemasu, H. (1972). Topics in model building, part II: on non-linear least squares. Technical Report No. 321. Department of Statistics, University of Wisconsin, Madison.
- Constable, S. Parker. R., and Constable C. (1987). Occam's inversion: A practical algorithm for generating smooth models from electromagnetic sounding data. *Geophysics*, 52, 289-300.
- Cook, K.L., and Van Nostrand, R.G. (1954). Interpretation of Resistivity Data Over Filled Sinks. *Geophysics*, 19, 761-790.
- Dahlin, T. and Loke, M.H. (2015). Negative apparent chargeability in time-domain induced polarisation data. *Geophysics*, 123, 322-332.
- Dabas, M., Tabbagh, A. and Tabbagh, J. (1994). 3-D Inversion in Subsurface Electrical Surveying-I. Theory. *Geophys. J. Int.*, 119, 975-990.
- Edwards, L.S. (1977). A Modified Pseudosection for Resistivity and IP. *Geophysics*, 42, 1020-1036.
- Ellis, R.G., and Oldenburg D.W. (1994). Applied geophysical inversion. *Geophysics*, 42, 1020-1036.
- Furnes, P. (1992). An Integral equation for geoelectric response of thin resistive bodies. *Geophysical Prospecting*, 40, 701-720.

- Heppner, F. and U. Grenander (1990). A stochastic nonlinear model for coordinated bird flocks. In S. Krasner, Ed., The Ubiquity of Chaos. AAAS Publications, Washington, DC.
- Johnson, T.C., Versteeg, R.J., Ward, A., Day-Lewis, F.D. and Revil, A. (2010). Improved hydrogeophysical characterization and monitoring through parallel modeling and inversion of time-domain resistivity and induced-polarization data. Geophysics, 75, WA27-WA41.
- Golub, G. H. and Reinsch, C. (1970). Singular Value Decomposition and Least Square Solutions. Numer. Math 14. 403-420.
- Karaoulis, M., 2009, Inverse Algorithm Development for Time Lapse Geoelectric Data, PhD Thesis (in greek)
- Kennedy, J., Eberhart, R. (1995). Particle Swarm Optimization. Proceedings of IEEE International Conference on Neural Networks. IV. pp. 1942–1948
- Keller, G.V., and Frischknecht, F.C. (1966). Electrical methods in geophysical prospecting. Pergamon Press, New York. NY.
- Koefoed, O. (1979). Geosounding principles, 1, Resistivity Sounding Measurements. Elsevier, Amsterdam.
- Kim, J.-H., Yi, M.-J., Son, S.J., (2012). Simultaneous Inversion of Time-domain SIP data, Proceedings of Near Surface Geoscience 2012, B34, Paris, Paris, 3-5 Sep.
- Kim, J. H., Supper, R., Ottowitz, D., Jochum, B., Yi, M.J. (2016). Processing of ERT Monitoring Data and Evaluation of Their Reliabilities. Near Surface Geophysics.

LaBrecque, D.J., Miletto, M., Daily, W., Ramirez, A. and Owen, E. (1996). The effects of noise on Occam's inversion of resistivity tomography data, *Geophysics*, 61, 538-548.

Lanczos, C. (1960). Linear differential operators. D. Van Nostrad Company Ltd.

Lee, T. (1975). An integral equation and its solution for some two and three dimensional problems in resistivity and induced polarization. *Geoph. J. Roy. Astr. Soc.*, 45, 1-95.

Lines, L.R., and Treitel S. (1984). Tutorial: a review of least-squares inversion and its application to geophysical problems. *Geophysical Prospecting*, 32, 159-186.

Lesur, V., Cuer, M. and Straub, A. (1999). 2-D and 3-D Interpretation of Electrical Tomography Measurements, Part 2: The Inverse Problem. *Geophysics*, 64, 396-402.

Loke, M.H., (2004). Res3Dinv ver 2.14. Geotomo Software. www.geoelectrical.com.

Levenberg, K. (1944). A Method for the Solution of Certain Non-Linear Problems in Least Squares. *The Quarterly of Applied Mathematics*, 2. 164-168.

Marquadt, D.W. (1980). An algorithm for least-square estimation of nonlinear parameters. *J. Soc. Indust. Appl. Math.*, 11, 431-441.

Oldenburg, D.W., (1997). Computation of Cole-Cole parameters from IP data, *Geophysics*, 62, 436-448.

Pain, C.C., Herwanger, J.V., Worthington, M.H. and de Oliveira, C.R.E. (2002). Effective Multidimensional Resistivity Inversion using Finite Element Techniques. *Geophys. J. Int.*, 151, 710- 728.

Park, S.K., and Van, G.P. (1991). Inversion of pole-pole data for 3-D resistivity structure beneath arrays of electrodes. *Geophysics*, 56, 951-960.

Pelton, W., Ward, S., Halloff, P., Sill, W., and Nelson P. (1978). Mineral discrimination and removal of inductive coupling with multifrequency induced polarization. *Geophysics*, 43, 588-609.

Press, W.H., Teukolsky, S.A., Vetterling, W.T., Flannery, B.P. (1992). *Numerical Recipes in C: The art of Scientific Computing*. Second Edition, Cambridge University Press.

Pridmore, D., Hohmann, G., Ward, S., and Sill, W. (1981). An investigation of finite-element modelling for electrical and electromagnetic data in three dimensions. *Geophysics*, 46, 1009-1024.

Reynolds, C. W. (1987). Flocks, herds and schools: a distributed behavioral model. *Computer Graphics*, 2 1 (4):25-34.

Roy, A., and Apparao, A. (1970). Depth of investigation in direct current methods. *Geophysics*, 36, 943-959.

Sasaki, Y. (1982). Automatic inversion of induced polarization data over 2-D structures. *Memoirs of the Faculty of Engineering, Kyushu University*, 42, 59-74.

Sasaki, Y. (1994). 3-D Inversion using the Finite Element Method. *Geophysics*, 59, 1839-1848.

Seigel, H.O., (1959). Mathematical formulation and type curves for induced polarization. *Geophysics* 24, 547–565.

Summer, J. (1976). *Principles of induced polarization for Geophysical Exploration*

Telford, W., Geldart, L., Sheriff, R., and Keys, D. (1991). Applied geophysics. Cambridge University Press.

Tikhonov, A.N. (1963). Solution of incorrectly formulated problems and the regularization method. Soviet Mathematics. 4. 1035-1038.

Tsourlos P., (1995). Modelling interpretation and inversion of multielectrode resistivity survey data: D. Phil. Thesis, University of York.

Tsourlos, P. and Ogilvy, R. (1999). An algorithm for the 3-D Inversion of Tomographic Resistivity and Induced Polarization data: Preliminary Results. Journal of the Balkan Geophysical Society, 2, 2, 30-45.

Ward, S. (1989) Resistivity and induced polarization methods: in Investigations in Geophysics no 5, Geotechnical and Environmental Geophysics vol I, ed. S.Ward SEG, Tulsa, 147-189.

Wilson, E.O. (1975). Sociobiology: The new synthesis. Belknap Press, Cambridge, MA.

Yi. M.J., Kim, J.H., Song, Y., Cho, S.J., Chung, S.H. and Suh, J.H. (2001). Three-Dimensional Imaging of Subsurface Structures using Resistivity Data. Geophysical Prospecting, 49, 483-497.

Yuval and Oldenburg, D.W. (1997). Computation of Cole-Cole parameters from IP data. Geophysics, 62, 436-448.

Zienkiewicz, O.C., and Taylor, R.L. (1989). The finite element method. 4th ed., Vol. 1, Basic formulation and linear problems. McGraw-Hill.

Appendix I

```
function [par RMS] = CalculateColeColeParameters(data,time,filename)
```

```
% {
```

```
*****Nivorlis Aristeides (c) 2016*****
```

This function solves the inverses problem of time domain IP decay curve.

data is a vector contain chargeability of each time.

time is a vector contain the time of each measurement.

filename is optional parameter. if given the results will be saved in an image file.

This code fits a curve (Pelton 1978 equation) in the data using PSO algorithm.

It returns a vector par [no tau c] and the RMS error of fit (not percent).

A simple version of PSO code taken from yarpiz.

Modified by Nivorlis Aristeidis to solve this optimization problem.

```
*****M.Sc. Thesis A.U.TH.*****
```

```
% }
```

```
% {
```

```
*****Problem Definition*****
```

```
% }
```

```
measuredData = data;
```

```
costFunction = @(x,time) PeltonCurvesForward(x,time); % Cost Function
```

```
nVar = 3; % Number of Unknown (Decision) Variables
```

```
nData = length(measuredData); % Number of Data Points
```

```
varSize = [1 nVar]; % Matrix Size of Decision Variables
```



```
varMin = [0 0 0]; % Lower Bound
varMax = [1 100 1]; % Upper Bound
```

```
% Parameters of PSO
```

```
MaxIt = 20; % Maximum Number of Iterations [20] opt
```

```
nPop = 100; % Population Size (Swarm Size) [100] opt
```

```
w = 1; % Inertia Coefficient
```

```
wdamp = 0.5; % Damping Ratio of Inertia Coefficient
```

```
c1 = 2; % Personal Acceleration Coefficient
```

```
c2 = 2; % Social Acceleration Coefficient
```

```
% The Flag for Showing Iteration Information
```

```
ShowIterInfo = false;
```

```
maxVelocity = [0.2 20 0.2];
```

```
minVelocity = -maxVelocity;
```

```
% {
```

```
*****Initialization*****
```

```
% }
```

```
% The Particle Template
```

```
empty_particle.Position = [];
```

```
empty_particle.Residual = [];
```

```
empty_particle.Velocity = [];
```

```
empty_particle.Cost = [];
```

```
empty_particle.Best.Position = [];
```

```
empty_particle.Best.Residual = [];
```

```
empty_particle.Best.RMS = [];
```

% Create Population Array

```
particle = repmat(empty_particle, nPop, 1);
```

% Initialize Global Best

```
globalBest.Residual = inf;
```

```
globalBest.RMS = inf;
```

% Initialize Population Members

```
for i=1:nPop
```

% Generate Random Solution

```
%particle(i).Position = zeros(varSize);
```

```
particle(i).Position(1) = unifrnd(varMin(1), varMax(1));
```

```
particle(i).Position(2) = unifrnd(varMin(2), varMax(2));
```

```
particle(i).Position(3) = unifrnd(varMin(3), varMax(3));
```

% Initialize Velocity

```
particle(i).Velocity = zeros(varSize);
```

% Evaluation

```
particle(i).Cost = costFunction(particle(i).Position,time);
```

```
particle(i).Residual = norm((measuredData - particle(i).Cost),2);
```

% Update the Personal Best

```
particle(i).Best.Position = particle(i).Position;
```

```
particle(i).Best.Residual = particle(i).Residual;
```

```
particle(i).Best.RMS = sqrt(sum((((measuredData-particle(i).Cost) ./ particle(i).Cost) .^ 2)) / (nData-nVar));
```

% Update Global Best

```
if particle(i).Best.Residual < globalBest.Residual
```

```
    globalBest = particle(i).Best;
```

```
end
```

```
end
```

% Array to Hold Best Cost Value on Each Iteration

bestResidual = zeros(MaxIt, 1);

bestRMS = zeros(MaxIt, 1);

% {

*****Main Loop of PSO*****

% }

% waitbar 0

wb = waitbar(0,'Processing...');

cnt=0;

total = MaxIt * nPop;

for it=1:MaxIt

for i=1:nPop

% Update Velocity

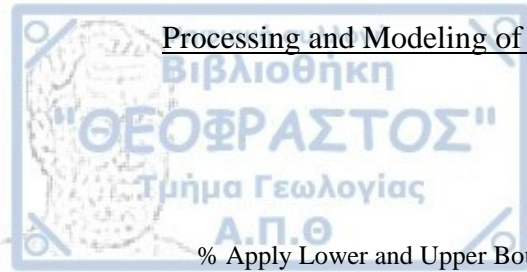
particle(i).Velocity = w*particle(i).Velocity ...
+ c1*rand(varSize).*(particle(i).Best.Position - particle(i).Position) ...
+ c2*rand(varSize).*(globalBest.Position - particle(i).Position);

% Apply Velocity Limits

particle(i).Velocity(1) = max(particle(i).Velocity(1), minVelocity(1));
particle(i).Velocity(1) = min(particle(i).Velocity(1), maxVelocity(1));
particle(i).Velocity(2) = max(particle(i).Velocity(2), minVelocity(2));
particle(i).Velocity(2) = min(particle(i).Velocity(2), maxVelocity(2));
particle(i).Velocity(3) = max(particle(i).Velocity(3), minVelocity(3));
particle(i).Velocity(3) = min(particle(i).Velocity(3), maxVelocity(3));

% Update Position

particle(i).Position = particle(i).Position + particle(i).Velocity;



% Apply Lower and Upper Bound Limits

particle(i).Position(1) = max(particle(i).Position(1), varMin(1));

particle(i).Position(1) = min(particle(i).Position(1), varMax(1));

particle(i).Position(2) = max(particle(i).Position(2), varMin(2));

particle(i).Position(2) = min(particle(i).Position(2), varMax(2));

particle(i).Position(3) = max(particle(i).Position(3), varMin(3));

particle(i).Position(3) = min(particle(i).Position(3), varMax(3));

% Evaluation

particle(i).Cost = costFunction(particle(i).Position,time);

particle(i).Residual = norm((measuredData - particle(i).Cost),2);

% Update Personal Best

if particle(i).Residual < particle(i).Best.Residual

particle(i).Best.Position = particle(i).Position;

particle(i).Best.Residual = particle(i).Residual;

particle(i).Best.RMS = sqrt(sum((((particle(i).Cost-measuredData) ./ measuredData) .^ 2)) / (nData-nVar));

% Update Global Best

if particle(i).Best.Residual < globalBest.Residual

globalBest = particle(i).Best;

end

end

% Update waitbar

cnt = cnt + 1;

waitbar(cnt/total,wb);

end

% Store the Best Cost Value

bestResidual(it) = globalBest.Residual;

bestRMS(it) = globalBest.RMS;

% Display Iteration Information

if ShowIterInfo

disp(sprintf('Iteration %d: Best Residual = %.5f [%.2f%%]',it,bestResidual(it),bestRMS(it)*100));

disp(sprintf('Best Solution
is:\nn=%.2f\ntau=%.1f\nc=%.2f',globalBest.Position(1),globalBest.Position(2),globalBest.Position(3)));

end

% Damping Inertia Coefficient

w = w * wdamp;

%%if bestResidual(it) < 0.01

%%break

%%end

end

waitbar(1,wb,'Done!!');

pause(0.1);

close(wb);

par = globalBest.Position;

RMS = globalBest.RMS;

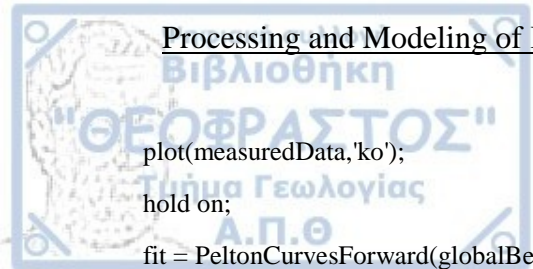
% {

*****Results*****

% }

fig = figure;

subplot(1,2,1);



```
plot(measuredData,'ko');
hold on;
fit = PeltonCurvesForward(globalBest.Position,time);
plot(fit,'r--');
title('Model Fit');
xlabel('Time');
ylabel('Chargeability (mV/V)');
% plot(BestCosts, 'LineWidth', 2);
subplot(1,2,2);
semilogy(bestRMS, 'LineWidth', 2);
title('Model Error');
xlabel('Iteration');
ylabel('Best Residual');
grid on;
if exist('filename','var')
    print(filename,'-dpng')
end
close(fig);
```